GAS PRODUCTION FROM HYDRATE-BEARING SEDIMENTS

A thesis
Presented to
The Academic Faculty

by

Jaewon Jang

In Partial Fulfillment
of the Requirements for the Degree
Doctor of Philosophy in the
School of Civil and Environmental Engineering

Georgia Institute of Technology
August 2011

GAS PRODUCTION FROM HYDRATE-BEARING SEDIMENTS

Approved by:

Dr. J. Carlos Santamarina, Advisor
School of Civil and Environmental Engineering
Georgia Institute of Technology

Dr. Susan E. Burns
School of Civil and Environmental Engineering
Georgia Institute of Technology

Dr. Haiying Huang
School of Civil and Environmental Engineering
Georgia Institute of Technology

Dr. Costas Tsouris
School of Civil and Environmental Engineering
Georgia Institute of Technology

Dr. Guillermo Goldsztein
School of Mathematics
Georgia Institute of Technology

Dr. Carolyn Ruppel
United States Geological Survey

Date Approved: July 5th 2011

ACKNOWLEDGEMENTS

I would like to express my sincere gratitude to my advisor, Dr. J. Carlos Santamarina for giving me such as excellent time in my life. It was really fortunate to work with him at Georgia Tech. I was always surprised by his endless curiosity, excellent guidance, and generous support, which really motivated and helped me to pursue my Ph.D. Thanks to Carlos, I was able to interact with many prominent professors in the world and excellent researchers in national laboratories, USGS, and DOE/NETL.

Insightful comments and recommendations from my committee members, Dr. Susan E. Burns, Dr. Haiying Huang, Dr. Costas Tsouris, Dr. Guillermo Goldsztein, and Dr. Carolyn Ruppel, enhanced my work. Especially, I would like to thank an Oak Ridge National Laboratory team, Dr. Costas Tsouris, Dr. Tommy J. Phelps, Dr. Claudia Rawn, Dr. Jiwon Moon, and Jonathan Alford for their dedicated help during my experiments. It was really great experience to work at the Oak Ridge National Laboratory.

Frequent discussions and interactions with Particulate Media Research Laboratory members enriched my research as well as my personal life: Taesup Yun, Hyunki Kim, Hosung Shin, Jooyong Lee, Douglas Cortes, Jongwon Jung, Changho Lee, Taehyuk Kwon, Nicolas Espinoza, Sheng Dai, Minsu Cha, Cesar Pasten, Seunghee Kim, Lucio G. Cruz, Eunseok Bang, Alessio Savioli, Songhun Chong, Junbong Jang, and Marco Terzariol.

Without the support from my parents and parents-in-law, I could not finish this work. My daughter Chloe also gave me a big support. Finally, my love Hyeyoung, thank you very much for your unconditional love and sincere support.

TABLE OF CONTENTS

LIST OF TABLES

LIST OF FIGURES

SUMMARY

Gas hydrates are crystalline compounds made of gas and water molecules. Methane hydrates are found in marine sediments and permafrost regions; extensive amounts of methane are trapped in the form of hydrates. The unique behavior of hydrate-bearing sediments requires the development of special research tools, including new numerical algorithms (tube- and pore-network models) and experimental devices (high pressure chambers and micromodels). Hydraulic conductivity decreases with increasing variance in pore size distribution; while spatial correlation in pore size reduces this trend, both variability and spatial correlation promote flow focusing. Invading gas forms a percolating path while nucleating gas forms isolated gas bubbles; as a result, relative gas conductivity is lower for gas nucleation than for gas invasion processes, and constitutive models must be properly adapted for reservoir simulations. Physical properties such as gas solubility, salinity, pore size, and mixed gas conditions affect hydrate formation and dissociation; implications include oscillatory transient hydrate formation, dissolution within the hydrate stability field, initial hydrate lens formation, and phase boundary changes in real field situations. High initial hydrate saturation and high depressurization favor gas recovery efficiency during gas production from hydrate-bearing sediments. Even a small fraction of fines in otherwise clean sand sediments can cause fines migration and concentration, vuggy structure formation, and gas-driven fracture formation during gas production by depressurization.

CHAPTER 1

INTRODUCTION

1.1 Motivation

Hydrate is a crystalline compound made of gas and water molecules found in marine sediments and permafrost regions. Methane hydrate could be a future alternative energy resource. The amount of methane contained in gas hydrate is estimated to be ~3×10^{15} m^3 [Boswell and Collett, 2011; NETL/DOE, 2011]. The largest fraction of gas hydrate resources resides in fine-grained sediments at relatively low saturations and may be difficult to recover; therefore, the technically-recoverable methane is assessed as ~3×10^{13} m^3 [Boswell and Collett, 2006; Boswell and Collett, 2011; NETL/DOE, 2011].

Global warming may trigger hydrate dissociation and cause the release of methane into the atmosphere. As methane is a very effective greenhouse gas, a positive feedback loop may follow and accelerate climate change [Reagan and Moridis, 2007; Reagan and Moridis, 2008].

The study of hydrate has implications on various geological and engineering processes. The upward migration of CO_2 can form CO_2 hydrate within the stability zone, i.e., a robust seal for CO_2 geological storage [Tohidi et al., 2010]. Liquid CO_2 can be used to replace methane in natural gas hydrates and to sequester CO_2 inside the sediment in the form of CO_2 hydrate [Jung et al., 2010]. Hydrate formation can hinder fluid flow inside flowline during hydrocarbon recovery [Sloan et al., 2009]. Finally, clathrate hydrate can be used for hydrogen storage [Koh et al., 2009].

1.2 Thesis organization

This research investigates fluid flow under single and mixed fluid conditions; pore-scale physical properties relevant to hydrate formation and dissociation, and their effect on

gas recovery efficiency, and emergent phenomena during gas production. Contents are organized as follows.

Chapter 2 investigates the effect of statistical and spatial pore size distribution on the global hydraulic conductivity using tube-network models. Results show prevalent flow localization.

Chapter 3 reports experimental results on gas invasion and gas nucleation. Then, the tube-network model is used to mimic the experiments. The effects of two different gas generation methods on the soil water characteristic curve and relative permeability are studied and explained.

Chapter 4 focuses on pore-scale observations and analytical studies relevant to hydrate formation and dissociation processes. Solubility, phase boundary changes (as a function of pore size, salinity, and gas mixture), and thermal properties of hydrate bearing sediments are studied and their implications on hydrate formation and dissociation for gas production are investigated.

Chapter 5 documents a numerical study on recoverable gas from hydrate bearing sediments. Fluid volume expansion after hydrate dissociation is calculated as a function of pressure and temperature conditions. Results show the effects of fluid volume expansion, initial hydrate saturation, mean pore size, and pore size distribution on gas recovery efficiency.

Chapter 6 investigates several emergent phenomena during hydrate dissociation, such as secondary ice formation, fines migration, vuggy structure formation, and gas-driven fracture formation using a new effective stress cell housed within the Seafloor Process Simulator. This is collaborative work with J.W. Jung and the research team at Oak Ridge National Laboratory.

Salient conclusions are summarized in Chapter 7.

CHAPTER 2

HYDRAULIC CONDUCTIVITY IN SPATIALLY VARYING MEDIA – A PORE-SCALE INVESTIGATION

2.1 Introduction

The hydraulic conductivity k depends on the size of pores, their spatial distribution and connectivity. These pore-scale characteristics are defined by grain size distribution and formation history. In turn, hydraulic conductivity controls fluid invasion, flow rate and pore fluid pressure distribution. Consequently, hydraulic conductivity affects storativity, effective stress and mechanical stability, plays a critical role in geotechnical design, determines contaminant migration and the selection of remediation strategies, defines the limits for resource recovery (oil production and residual oil saturation, gas extraction from hydrate bearing sediments, methane recovery from coal bed methane, non-isothermal fluid flow in geothermal applications), and is a central parameter in the design of waste disposal strategies, from nuclear waste to CO_2 sequestration.

In this study, we investigate the effect of pore-scale spatial variability on macroscale hydraulic conductivity using network models, following the pioneering work by Fatt (1956a, 1956b, 1956c). The main advantage of network models resides in their ability to capture pore-scale characteristics within a physically sound upscaling algorithm to render macroscale properties relevant to the porous medium. Networks can be generated either by assuming an idealized regular geometry, by adopting physically representative networks that capture the porous structure [Bryant et al., 1993] or by mapping the pore structures measured by high resolution tomographic technics onto a network structure [Dong and Blunt, 2009, see also Al-Raoush and Wilson, 2005; Narsilio et al., 2009]. Network model results are consistent with experimentally obtained values of permeability [Al-Kharusi and Blunt, 2007; Al-Kharusi and Blunt, 2008]. The approach has been used to

upscale a wide range of pore-scale phenomena such as viscous drag, capillarity, phase change (e.g., ice or hydrate), and mineral dissolution. Consequently, network models have been used to study multiphase flow [Valvatne, 2004; Al-Kharusi and Blunt, 2008], wettability effects in multiphase flow [Suicmez et al., 2008], fine migration and clogging [Kampel et al., 2008], mineral dissolution [Hoefner and Fogler, 1988; Fredd and Fogler, 1998], pressure-induced pore closure [David, 1993], CO_2 sequestration [Kang et al., 2005], liquid or gas diffusion through porous media [Laudone et al., 2008; Mu et al., 2008], drying and unsaturation [Prat, 2002; Surasani et al., 2008], the effect of flow localization on diffusion [Bruderer and Bernabé, 2001], and resource recovery such as methane production from hydrate bearing sediments [Tsimpanogiannis and Lichtner, 2003; Tsimpanogiannis and Lichtner, 2006]. Furthermore, pore-scale network models have been coupled to continuum models to conduct field-scale simulations of complex processes such as clogging, reactive flow, and non-Darcian flow near well-bores [Balhoff et al., 2007].

The first part of the manuscript summarizes previous studies. Then, we provide a detailed description of the numerical model, report statistical results in terms of equivalent hydraulic conductivity, and compare trends against known and analytically derived lower and upper bounds.

2.2 Variability in hydraulic conductivity – Previous studies

Hydraulic conductivity can vary by more than ten orders of magnitude, from very low values in montmorillonitic shale to high values in gravels and boulders. Hydraulic conductivity varies widely even for a given material. The coefficient of variation, defined as the ratio between the standard deviation and the mean, can range from 100% to 800% for both natural sediments [Albrecht et al., 1985; Cassel, 1983; Duffera et al., 2007; Libardi et al., 1980; Warrick and Nielsen, 1980] and remolded sediments [Benson, 1993; Benson and Daniel, 1994]. Data are typically log-normal distributed so that $x=\log(k/[k])$ is

Gaussian, where [k] captures the dimensions of k [Freeze, 1975; Hoeksema and Kitanidis, 1985].

The correlation length L is the distance where the spatial autocorrelation decays by 1/e≅0.368. The correlation length for hydraulic conductivity ranges from less than a meter to hundreds of meters. It is typically longer in the horizontal plane than in the vertical direction, in agreement with layering and weathering patterns [Bjerg et al., 1992; Ditmars et al., 1988; DeGroot, 1996; Lacasse and Nadim, 1996].

The equivalent hydraulic conductivity k_{eq} of spatially varying media reflects the distribution of individual values k_i, their spatial correlation and flow conditions. Available close-form solutions are summarized in Table 2.1. In particular, the equivalent hydraulic conductivity k_{eq} is (1) the harmonic mean of individual k_i values in one-dimensional systems, (2) the geometric mean in two-dimensional media, and (3) higher than the geometric mean when seepage in 3D systems can take place through multiple alternative flow paths. The equivalent hydraulic conductivity in these three cases can be computed in terms of the geometric mean k_g and the variance σ^2 in $\log(k/[k])$, as captured in the following expressions [Gutjahr et al., 1978; Dagan, 1979 - refer to Table 2.1]:

$$k_{eq} = k_h = k_g \left[1 - \left(\sigma^2_{\log k}/2\right)\right] \quad \text{(1D system)} \tag{2.1}$$

$$k_{eq} = k_g \quad \text{(2D system)} \tag{2.2}$$

$$k_{eq} = k_g \left[1 + \left(\sigma^2_{\log k}/6\right)\right] \quad \text{(3D system)} \tag{2.3}$$

More complex systems have been studied using equivalent continuum numerical methods. Those results show that (1) flow rate decreases as the coefficient of variation COV(k) increases, and (2) the mean hydraulic conductivity in correlated fields is higher than in uncorrelated fields with the same coefficient of variation COV(k) [Griffiths and Fenton, 1993; Griffiths et al., 1994; Griffiths and Fenton, 1997].

Table 2.1. Equivalent hydraulic conductivity – Mixture models and Bounds

Equivalent k_{eq}	**Assumptions / Comments**	**Reference**
$k_a = \sum_{i=1}^{N} t_i \cdot k_i \Big/ \sum_{i=1}^{N} t_i$ 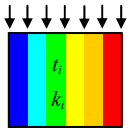	Arithmetic mean - Parallel Parallel stratified media Upper bound	Wiener (1912)
$k_h = \sum_{i=1}^{N} t_i \Big/ \sum_{i=1}^{N} \frac{t_i}{k_i}$ 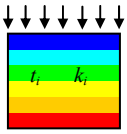	Harmonic mean - Series Perpendicular stratified media (1D flow) Lower bound	
$k_g = \left(\prod_{1}^{N} k_i \right)^{1/N}$ 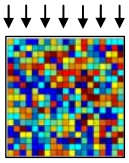	Geometric mean Lognormal k_i distribution / isotropic media 2D flow	Warren and Price (1961)
$k_{eq} = k_a^{\alpha} k_h^{1-\alpha} \quad \left(\alpha = \frac{D-1}{D} \right)$	Statistically homogeneous and isotropic Weighted average of Wiener bounds	Landau and Lifshitz (1960)
$k_a - \frac{f_1 f_0 (k_1 - k_0)^2}{k_0 (D - f_0) + k_1 f_0} \le k_{eq} \le k_a - \frac{f_1 f_0 (k_1 - k_0)^2}{k_1 (D - f_1)^2 + k_0 f_1}$	Based on a model constructed of composite spheres. Isotropic binary medium. Uniform flow	Hashin and Shtrikman (1962)
if $f_0 \ge 0.5 \Rightarrow k_{eq} \ge k_{ac}$ *if* $f_0 \le 0.5 \Rightarrow k_{eq} \le k_{ac}$ *if* $f_0 = 0.5 \Rightarrow k_{eq} = \sqrt{k_1 \cdot k_0}$ where $k_{ac} = \frac{1}{2}\left[(f_1 - f_0)(k_1 - k_0) + \sqrt{(f_1 - f_0)^2 (k_1 - k_0)^2 + 4 k_1 k_0} \right]$	Isotropic 2D random two phase mosaic medium. Uniform flow.	Matheron (1967)
if $f_0 \ge 0.5 \Rightarrow k_{eq} \le k_m$ $k_m = \frac{f_1 k_0 k_1 + f_0 k_a \sqrt{k_0 (2k_a - k_0)}}{f_1 m^* + f_0 \sqrt{k_0 (2k_a - k_0)}}$ *if* $f_0 \le 0.5 \Rightarrow k_{eq} \ge k_m$ $k_m = k_0 k_1 \frac{f_0 k_a + f_1 \sqrt{k_0 (2m^* - k_0)}}{f_1 k_0 k_1 + f_1 m^* \sqrt{k_0 (2m^* - k_0)}}$		

Note: k_{eq} = equivalent hydraulic conductivity; f_0 and f_1 are the fractions of the medium with hydraulic conductivity k_0 and k_1, where $k_1 > k_0$, D=space dimension (i.e., 1, 2 or 3); $m^* = f_1 \cdot k_0 + f_0 \cdot k_1$

2.3 Network models

Network models consist of tubes connected at nodes, and can be used to simulate fluid flow through pervious materials. Volume can be added at nodes to reproduce various conditions [Blunt, 2001; Reeves and Celia, 1996; Acharya et al., 2004]. The flow rate through a tube q [m^3/s] is a function of fluid viscosity η [$N \cdot s/m^2$], tube radius R [m], tube length ΔL [m], and pressure difference between end nodes ΔP [N/m^2]:

$$q = \frac{\pi R^4}{8 \eta \Delta L} \Delta P = \alpha \cdot \Delta P \qquad \text{tube equation} - \textit{Poiseuille} \qquad (2.4)$$

where $\alpha = \pi R^4/(8\eta \Delta L)$ under isothermal condition, constant viscosity, and constant tube radius. Mass conservation requires that the total flow rate into a node equals the total flow rate out of the node:

$$\sum q_i = 0 \qquad \text{node equation} \qquad (2.5)$$

Equations 2.4 and 2.5 can be combined to determine the pressure at a central node P_c as a function of the pressure at neighboring nodes P_i.

$$P_c = \frac{\sum \alpha_i P_i}{\sum \alpha_i} \qquad (2.6)$$

If all α-values are equal, Equation 2.6 predicts $P_c = (P_a+P_b+P_r+P_l)/4$. It is worth noting that this equation is identical to the first order central finite difference formulation of Laplace's field equation.

Equation 2.6 is written at all internal nodes to obtain a system of linear equations which can be captured in matrix form:

$$\underline{\underline{A}}\,\underline{P} = \underline{B} \qquad (2.7)$$

where the matrix $\underline{\underline{A}}$ is computed with tube conductivities α, $\underline{P}$ is the vector of unknown pressures at internal nodes, and the vector $\underline{B}$ captures known boundary pressures. The vector $\underline{P}$ can be recovered as $\underline{P} = \underline{\underline{A}}^{-1}\underline{B}$. Once fluid pressures P_i are known at all nodes, the global flow rate Q through the network is obtained by adding the flow rate q (Equation 2.4)

in all tubes that cross a plane normal to the flow direction. The equivalent network hydraulic conductivity in the direction of the prescribed external pressure gradient is calculated from the computed flow rate Q and the imposed pressure gradient between inlet and outlet boundaries. Insightful information is gained by analyzing prevailing flow patterns within the networks as will be shown later in this manuscript.

Network generation. Networks are realized with pre-specified statistical characteristics. We control the coefficient of variation in tube size, spatial correlation, and isotropy to generate networks with different tube size distribution (mono-sized, bimodal, or log-normal distributed) spatially uncorrelated or correlated and isotropic or anisotropic. Every realization is identified according to these three qualifiers.

Pore size R is log-normally distributed in sediments. Mercury intrusion porosimetry data for a wide range of soils and effective stress conditions show that the standard deviation in $\sigma(\ln(R/[\mu m]))$ is about 0.4±0.2 [Phadnis and Santamarina, 2011]. Examples of statistical distributions used in this study are shown in Figure 2.1. Throughout the manuscript, the log-normal distribution of pore cross sectional area is used in terms of R^2, i.e., $\log(R^2/[R]^2)$ where [R] indicates unit of R. Tube R^2 values are generated as $R^2=10^a$ where a is a set of Gaussian distributed random numbers with given standard deviation. Values R^2 are scaled to satisfy the selected mean value. While we assume log-normal distribution for network generation, we analyze results and global trends in terms of the mean and standard deviation of R^2, that is $\mu(R^2)$ and $\sigma(R^2)$ for each realization.

The computer code is written in MATLAB. The run time for each realization in a 2.4GHz processor is ~40 min. The reported study was conducted using a stack of dual-core computers.

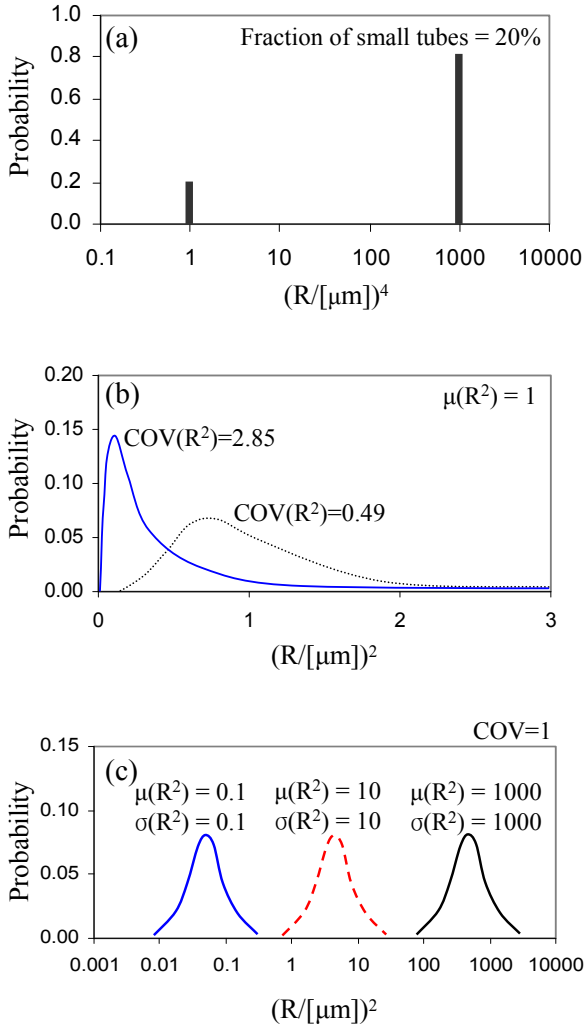

Figure 2.1. Schematic of typical distribution of R^2 in spatially varying fields. (a) Bimodal distribution of tubes (used in Figure 2.2 and 2.3) when fraction of small tubes is 20%. The relative size of large to small tube radii is $(R_L/R_S)^4=10^3$. (b) Two distributions of tube size R^2 with the same $\mu(R^2)$ but different standard deviation used in Figure 2.4, 2.6, and 2.7. As the coefficient of variation increases, the distribution of R^2 is skewed to the right. (c) Distributions of R^2 used in Figure 2.5. Note that $\sigma(R^2)$ of two sets of tube size distribution with different $\mu(R^2)$ are adjusted to have same $COV(R^2)$.

2.4 Studied cases – Numerical results

Network models are used herein to extend previous studies on the effect of spatial variability and anisotropy on hydraulic conductivity. Numerical results are presented next. Simulation details are listed in the corresponding figure captions.

2.4.1 Bimodal distribution – Effect of coordination number and bounds

Consider a bimodal distribution made of large and small tubes of relative size R_L/R_S=5.62 so that their conductivity ratio is $k_L/k_S=10^3$ for constant tube length (refer to Equation 2.4). Twenty spatially randomly arranged networks are generated for each fixed fraction of small tubes. Two-dimensional networks with coordination number *cn*=4, 6, and 8 and three-dimensional networks with coordination number *cn*=6 are used to investigate the effect of coordination number on flow conditions. Computed hydraulic conductivities are averaged for the 20 realizations and plotted in Figure 2.2 where the mean value is normalized by the hydraulic conductivity of the network model made of large tubes only, k_{mix}/k_L.

Results in Figure 2.2 show that network conductivity range in three orders of magnitude from k_{mix}/k_L=0.001 to 1.0 in agreement with the size ratio $(R_L/R_S)^4=10^3$. Hydraulic conductivity values increase as the coordination number increases. There is a pronounced decrease in flow rate where large tubes cease to form a percolating path. Percolation thresholds (readily identified in linear-linear plots - see also Hoshen and Kopelman, 1976) decrease as coordination numbers increase; results are consistent with reported percolation thresholds for various networks: 2D-honeycomb (fraction of small tubes=0.65), 2D-square (0.5), 2D-triangular (0.35), and 3D-simple cubic arrangement (0.25) [Sahimi, 1994; Stauffer and Aharony, 1992].

Analytical solutions for equivalent hydraulic conductivity, and lower and upper bounds summarized in Table 2.1 are compared to numerical results in Figure 2.3. The normalized mean hydraulic conductivity for 20 realizations using 2D networks with *cn*=4 follows the Matheron's mixture model. All simulation results are between Wiener's and Hashin and Shtrikman's upper and lower bounds (Table 2.1). Hashin and Shtrikman bounds incorporate the dimensionality of the system resulting in 3D bounds that are shifted toward high k_{eq} values compared to 2D bounds. Overall, numerical and analytical results

point to higher value of hydraulic conductivity with a larger number of alternative flow paths.

2.4.2 Coefficient of variation in random networks

We explore next the effect of variance in R^2 by creating 2D and 3D networks with the same nominal mean $\mu(R^2)$. Network statistics, mean $\mu(R^2)$, standard deviation $\sigma(R^2)$, and coefficient of variation $COV(R^2)$ are evaluated for each realization. Note that R^2-distributions are skewed toward higher values as the coefficient of variation increases (Figure 2.1b) even though they all have the same $\mu(R^2)$.

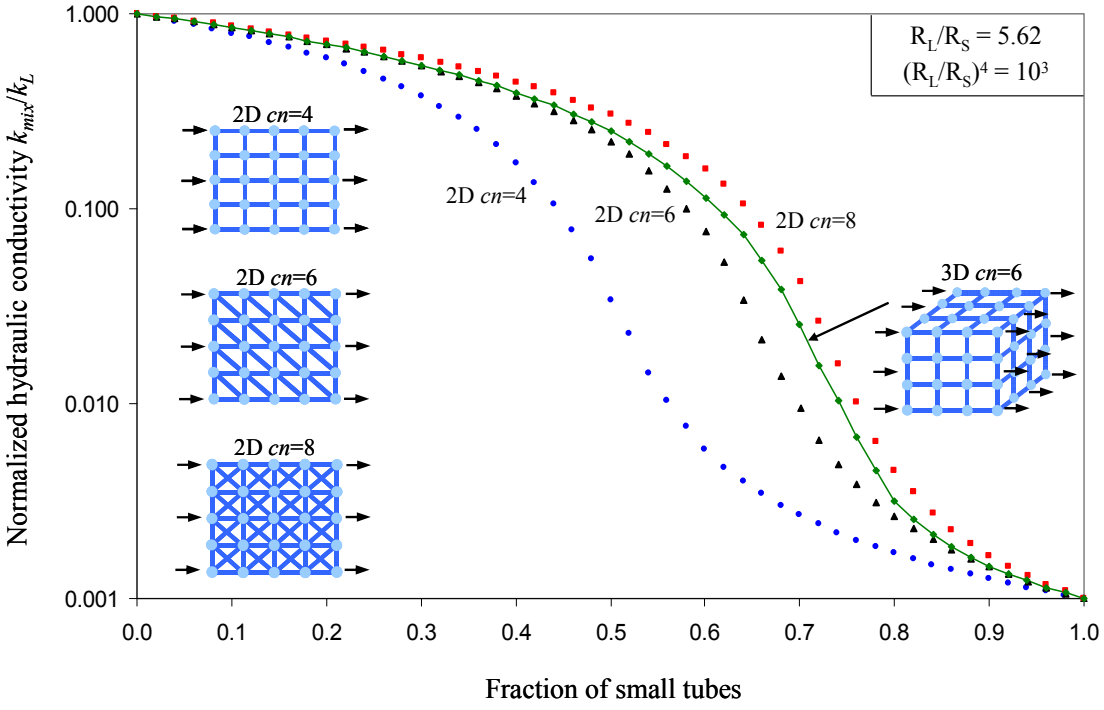

Figure 2.2. Effect of coordination number *cn* on equivalent hydraulic conductivity in bimodal distribution k_{mix} normalized by the hydraulic conductivity in the field composed of only large tubes k_L. Each point is the average value of 20 realizations. Bimodal distribution of tubes. The relative size of large L to small S tube radii is $(R_L/R_S)^4 = 10^3$. Two-dimensional network model: 50x50 nodes, 4900 tubes, and *cn*=4 (circle) / *cn*=6 (triangle) / *cn*=8 (square). Three-dimensional network model: 15x15x15 nodes, 9450 tubes, and *cn*=6 (diamond).

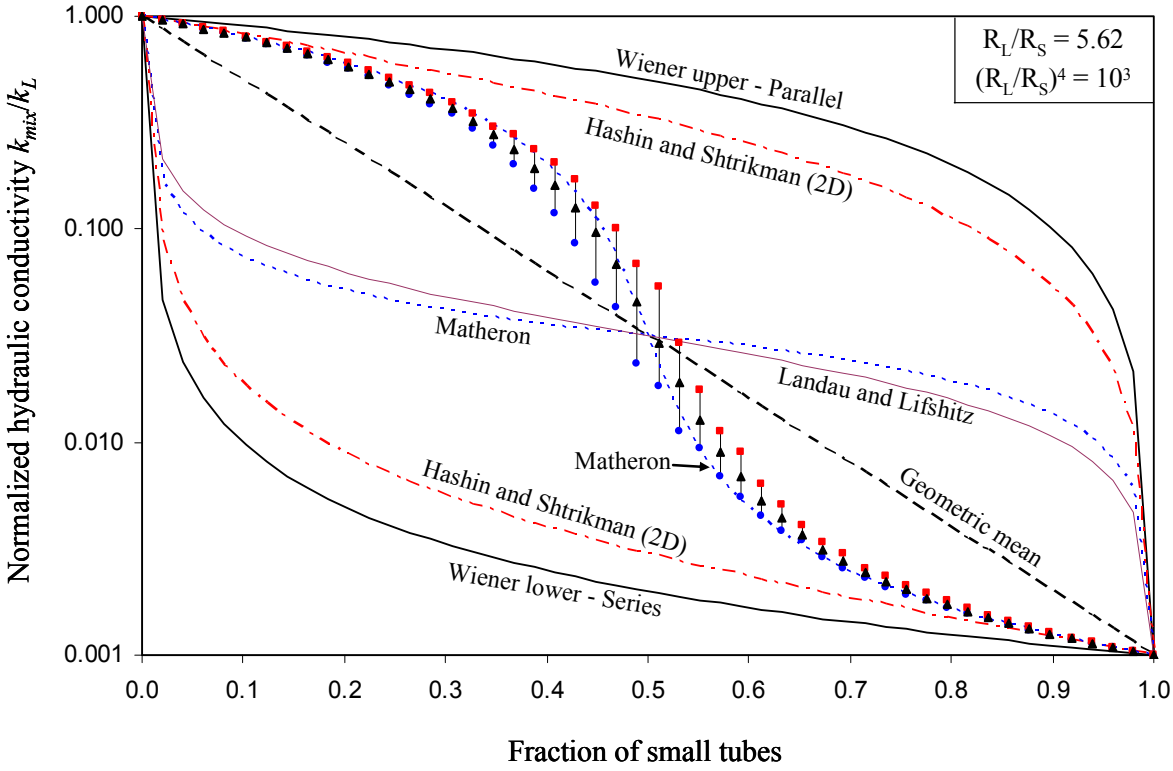

Figure 2.3. Computed equivalent hydraulic conductivity in bimodal distribution k_{mix} normalized by the hydraulic conductivity in the field composed of only large tubes k_L, models and bounds as a function of the fraction of small tubes. Points represent the maximum (square), average (triangle), and minimum (circle) values of 20 realizations at each fraction of small tubes. Bounds and models are described in Table 2.1. Two-dimensional network model: 50x50 nodes, 4900 tubes, bimodal distribution of tubes, relative size of large L to small S tube radii $(R_L/R_S)^4 = 10^3$, and coordination number cn=4.

The conductivity of a given realization k_{dist} is normalized by the conductivity k_{mono} of the network made of all equal size tubes, i.e., $R^2=\mu(R^2)$ and $COV(R^2)=0$. The normalized hydraulic conductivity k_{dist}/k_{mono} decreases as the coefficient of variation of R^2 increases (Figure 2.4) (see similar results in Bernabé and Bruderer, 1998). The normalized arithmetic, geometric, and harmonic means computed for each network are shown as shaded areas on Figure 2.4. The range in normalized hydraulic conductivities for 2D cn=4 networks coincides with the shaded band of geometric means computed for all networks. Computed hydraulic conductivity values for 3D cn=6 and 2D cn=6 networks are the same

as the range obtained using Equation 2.3 and confirm the applicability of the close-form solutions.

These trends result from the increased probability of large tubes becoming surrounded by smaller tubes, i.e., there is an increased probability of finding a small tube along every potential flow path with increasing coefficient of variation COV(R^2). This effect is more pronounced when the coordination number decreases because there are fewer alternative flow paths; in other words, network models with high coordination number are less sensitive to variation in pore size COV(R^2) because a higher number of alternative flow paths develop in high connectivity condition. Flow patterns are analyzed in detail later in this manuscript.

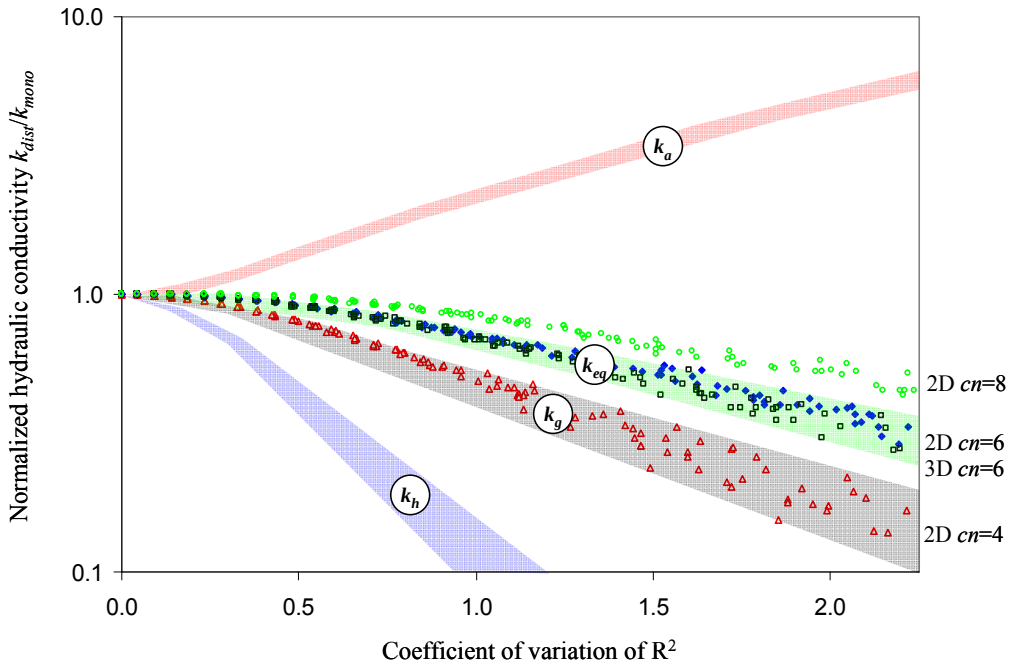

Figure 2.4. Equivalent hydraulic conductivity in uncorrelated tube network k_{dist} normalized by the hydraulic conductivity for the mono-sized tube network k_{mono} as a function of the coefficient of variation of R^2. Each point is a single realization. All realizations have the same $\mu(R^2)$. Two-dimensional network model: 50x50 nodes, 4900 tubes, and *cn*=4 (empty triangle), *cn*=6 (empty square), *cn*=8 (empty circle). Three-dimensional network model: 15x15x15 nodes, 9450 tubes, and *cn* =6 (solid diamond). Shaded areas show arithmetic k_a, geometric k_g, harmonic k_h mean of 2D and 3D system, and analytical solution k_{eq} of 3D system (Equation 2.3).

2.4.3 Anisotropic, uncorrelated networks

When tubes parallel to the predominant fluid flow direction are mono-sized R_P ("parallel tubes"), the flow rate is proportional to R_P^4, and the distribution of tube size transverse to flow direction R_T ("transverse tubes") does not affect the global flow rate because there is no local gradient or fluid flow transverse to the main flow direction. This is not the case when tubes parallel to the flow direction are of different size, i.e., not mono-sized.

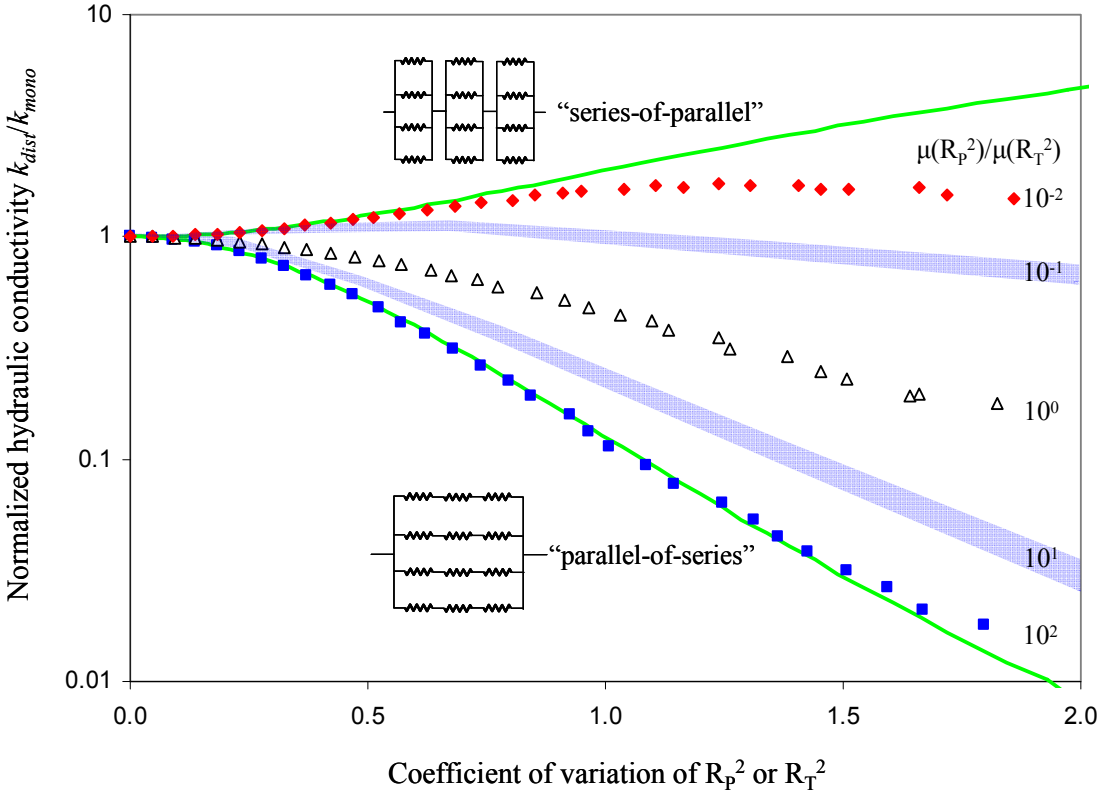

Figure 2.5. Anisotropic conductivity: Equivalent hydraulic conductivity in uncorrelated and distributed tube network k_{dist} normalized by the hydraulic conductivity for the mono-sized tube network k_{mono} as a function of coefficient of variation of R^2. Normalized hydraulic conductivities are obtained at different values of the ratio between the mean tube size parallel and transverse to the flow direction $(R_P/R_T)^2$. Each point is the average value of 20 realizations (using same set of tube sizes, but different spatial distribution). For clarity, results for intermediate sequences are shown as shaded area. Normalized hydraulic conductivities in series of parallel and parallel of series circuits are also obtained. Two-dimensional network model: 50x50 nodes, 4900 tubes, *cn*=4, and log-normal distribution of R^2.

Let's consider log-normal distributions for the size R_P^2 and R_T^2 of both parallel and transverse tubes. We select different mean values $\mu(R_P^2) \neq \mu(R_T^2)$ and adjust standard deviations $\sigma(R_P^2)$ and $\sigma(R_T^2)$ so that both parallel and transverse tubes have the same coefficient of variation $COV(R^2)$.

Results in Figure 2.5 show that the normalized hydraulic conductivity decreases as the coefficient of variation $COV(R^2)$ increases when $\mu(R_P^2)/\mu(R_T^2)>1$. However, the hydraulic conductivity may actually increase when transverse tubes are of high conductivity as shown by the $\mu(R_P^2)/\mu(R_T^2)= 10^{-2}$ case: fluid flows along transverse tubes until it finds parallel tubes of high conductivity, mostly with $R_P^2>\mu(R_P^2)$.

Two extreme networks of "series-of-parallel" and "parallel-of-series" tubes provide upper and lower bounds to the numerical results (shown as lines in Figure 2.5). When the ratio of $(R_P/R_T)^2$ is larger than 10^{-1}, the network responds as a parallel combination of tubes in series. When the ratio of $(R_P/R_T)^2$ is smaller than 10^{-1}, pressure is homogenized along the relatively large transverse tubes, as captured in the series-of-parallel bound.

2.4.4 Spatial correlation in pore size – Isotropic networks

Spatial correlation in pore size upscales to the macroscale hydraulic conductivity in unexpected ways. The methodology followed in this study starts with a set of tubes with fixed $\mu(R^2)$ and $COV(R^2)$. Then, we use the same set of tubes to generate 100 randomly redistributed spatially uncorrelated networks and other three sets of 100 isotropically correlated networks with correlation lengths L/D=5/39, 15/39, and 30/39 (where L is correlation length and D is the network size transverse to the overall flow direction) and for different $COV(R^2)$. We use the method by Taskinen et al. (2008) to create correlated fields.

Hydraulic conductivities are numerically computed for all networks k_{cor}. For comparison, the hydraulic conductivity k_{mono} is evaluated for a network of equal size tubes, i.e., $COV(R^2)=0$. The normalized mean hydraulic conductivity k_{cor}/k_{mono} computed using

the 100 realizations for each COV(R^2) is plotted versus COV(R^2) in Figure 2.6a. The normalized mean conductivity decreases with COV(R^2) in all cases in agreement with Figure 2.4, but it is higher in correlated than in uncorrelated networks. Note that the variance from the mean trend also increases with COV(R^2) and it is exacerbated by spatial correlation L/D (Figure 2.6b).

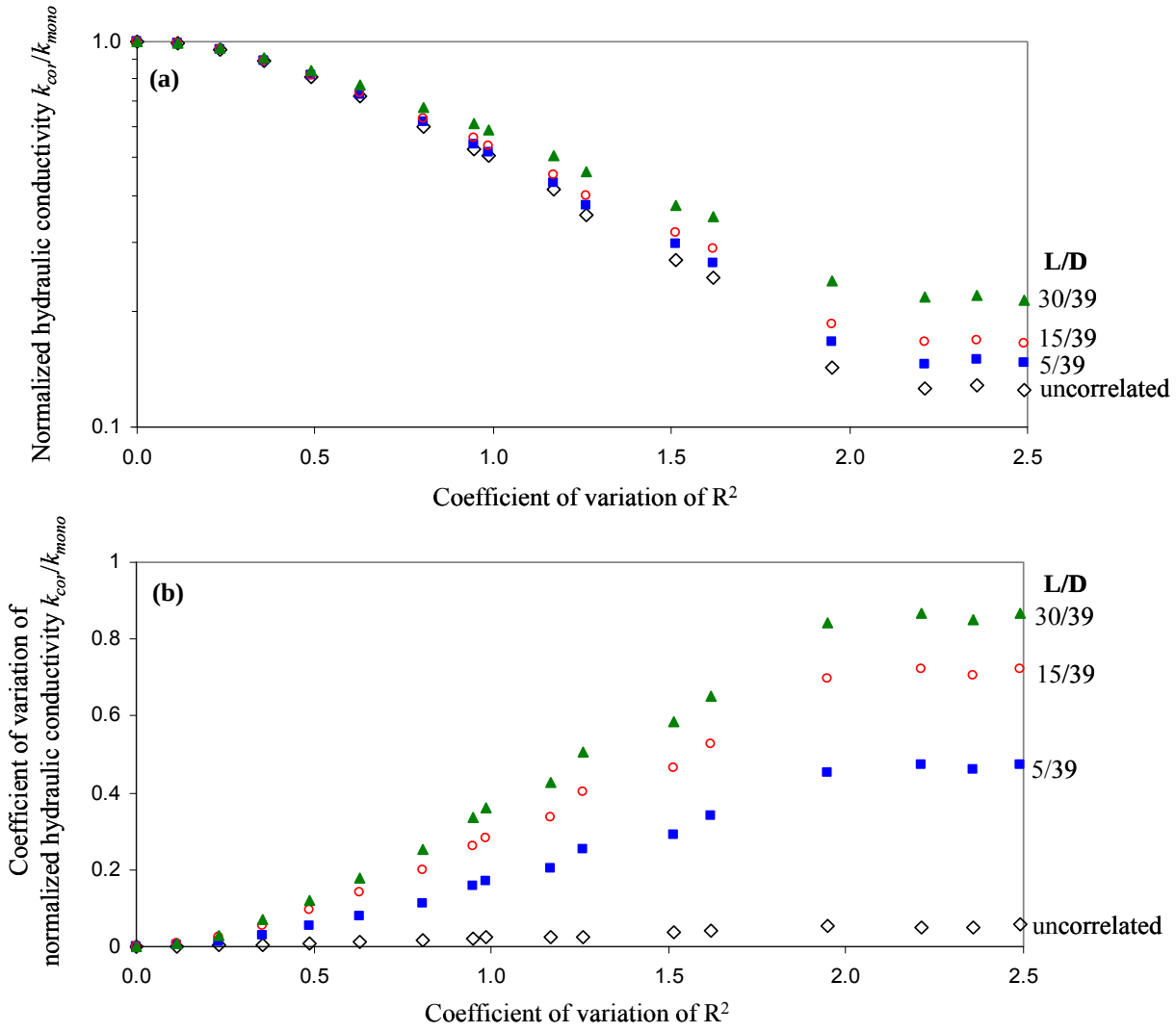

Figure 2.6. Correlated field. (a) Equivalent hydraulic conductivity in isotropic uncorrelated and correlated tube network k_{cor} normalized by the hydraulic conductivity for the mono-sized tube network k_{mono} as a function of the coefficient of variation of R^2. (b) Coefficient of variation of the equivalent hydraulic conductivities as a function of the coefficient of variation of R^2. The correlation length L is reported relative to the specimen size. Each point stands for the average of 100 realizations. Two-dimensional network model: 40x40 nodes, 3120 tubes, *cn*=4, and log-normal distribution of R^2.

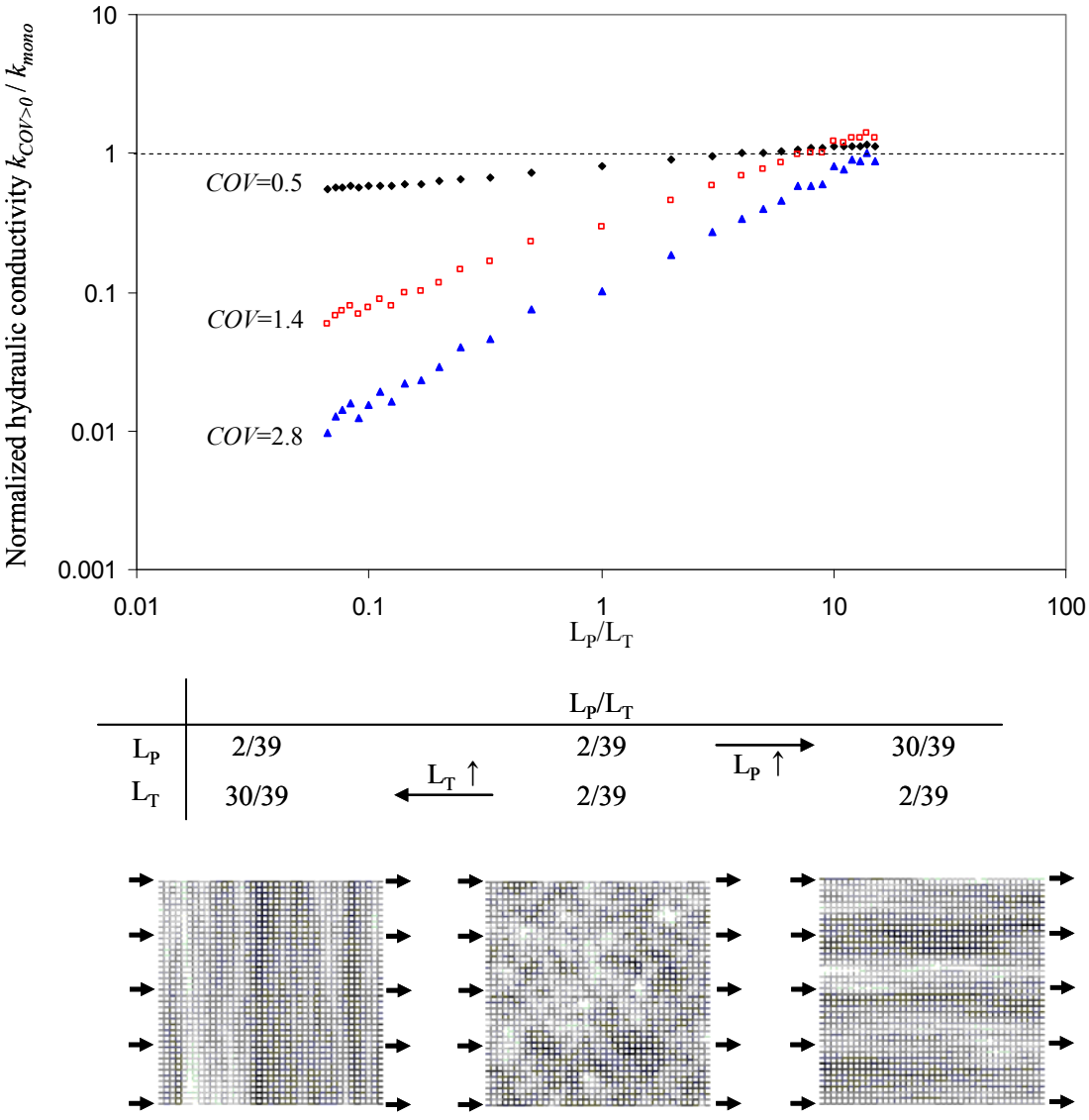

Figure 2.7. Effect of anisotropic correlation on equivalent hydraulic conductivity in an anisotropically correlated tube network $k_{COV>0}$ normalized by the hydraulic conductivity for the mono-sized tube network k_{mono}. Three sets of tubes different $COV(R^2)$ are generated and used to form correlated fields of different anisotropic correlation length. L_P and L_T are the correlation lengths parallel and transverse to flow direction. D is the length of medium perpendicular to the flow direction. In the range between L_P/L_T=0.01 to 1, L_P=2D/39 fixed and L_T changes from 2D/39 to 30D/39. In the range between L_P/L_T=1 to 100, L_T=2D/39 fixed and L_P changes from 2D/39 to 30D/39. Each point is an average of 20 realizations. Two-dimensional network model: 40x40 nodes, 3120 tubes, *cn*=4, and log-normal distribution of R^2.

2.4.5 Spatial correlation in pore size – Anisotropic networks

In order to gain further insight into the previous results, we study the effect of anisotropy in correlation length following a similar approach, but in this case we distinguish the correlation length parallel to the overall flow direction L_P from the correlation length transverse to the overall flow direction L_T. The isotropic case is created with $L_P/D=L_T/D=2/39$ so that $L_P/L_T=1.0$. High correlation parallel to the flow direction is simulated by increasing L_P/D, while high correlation transverse to the flow direction is imposed by increasing L_T/D. The study is repeated for three sets of R^2 with $COV(R^2)=0.5$, 1.4, and 2.8.

Average hydraulic conductivity values (based on 20 realizations) are normalized by the hydraulic conductivity k_{mono} of the network made of equal size tubes. Results in Figure 2.7 show that the normalized hydraulic conductivity $k_{COV>0}/k_{mono}$ increases as spatial correlation parallel to the flow direction L_P/L_T increases and it may even exceed the conductivity of the mono-sized tube network in highly anisotropic networks with very high L_P/L_T values. Otherwise, variation in tube size $COV(R^2)$ has a similar effect reported previously: an increase in $COV(R^2)$ causes a decrease in hydraulic conductivity (see Figure 2.4 and 2.6). Overall, results in Figure 2.7 point to pore-scale flow conditions similar to those identified in Figure 2.5.

2.5 Discussion

Numerical results show the evolution of percolation in bimodal system (Figure 2.2 and 2.3), and the decrease in hydraulic conductivity with increasing variance in pore size while the mean value of pore size remains constant. This is observed for all types of network topology (Figure 2.4), and in both spatially correlated and uncorrelated networks (Figure 2.6). The only exception to this trend is found in highly anisotropic porous media in the direction that favors fluid flow (Figure 2.5 and 2.7).

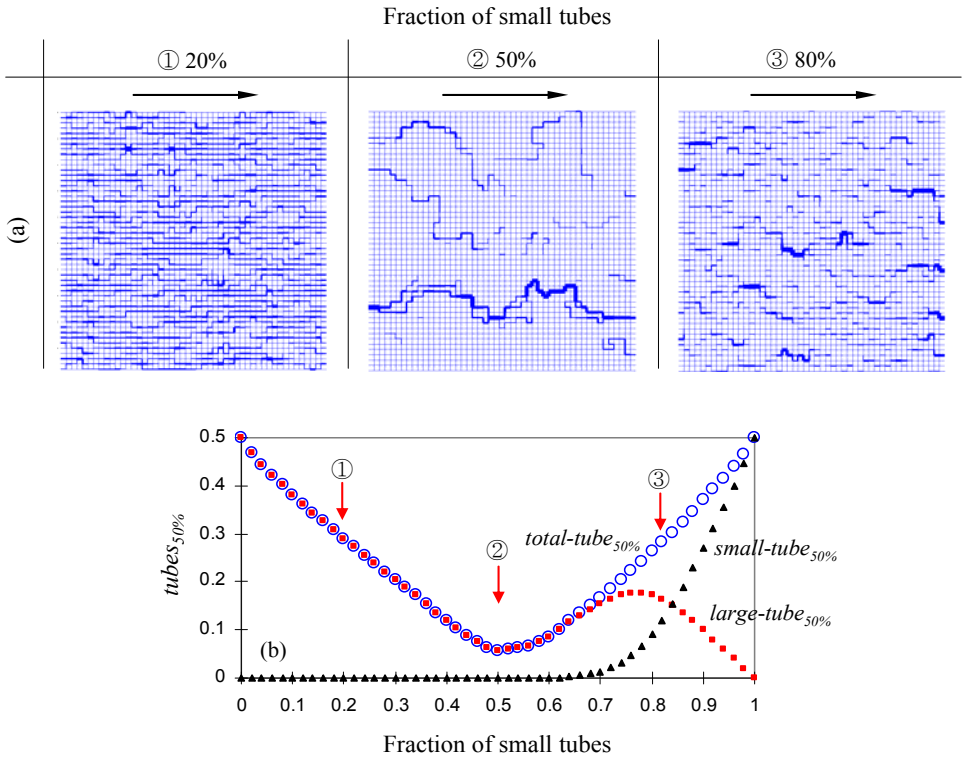

Figure 2.8. Analysis of flow pattern in network model of bimodal distribution of R^2 (2D *cn*=4 - Percolation occurs when the fraction of small tubes is 0.5. Refer to Figure 2.2 and 2.3 for simulation details). (a) Flow intensity in each tube of the network of different fraction of small tubes. The change of flow pattern in each fraction of small tubes is well detected. The arrow indicates the predominant fluid flow direction. (b) Fraction of tubes $tube_{50\%}$ responsible for 50% of total conductivity. The fraction $total\text{-}tube_{50\%}$ is the summation of $small\text{-}tube_{50\%}$ and $large\text{-}tube_{50\%}$.

To facilitate the visualization of flow patterns, we compute tube flow rates (Equation 2.4), and represent tubes with lines of thickness proportional to flow rate (additional plotting details are noted in figure captions). Figure 2.8a shows flow patterns in bimodal distribution networks made of different fractions of small tubes. Flow localizes along dominant flow channels when the fraction of small tubes is 50% which is near the percolation threshold for this network (2D *cn*=4). Few flow paths are responsible for the global conductivity in networks where the fraction of either small or large tubes is ~50% (Figure 2.8a ②); conversely, multiple flow paths contribute to the global conductivity in networks made of a majority of either small or large tubes (Figure 2.8a ① and ③).

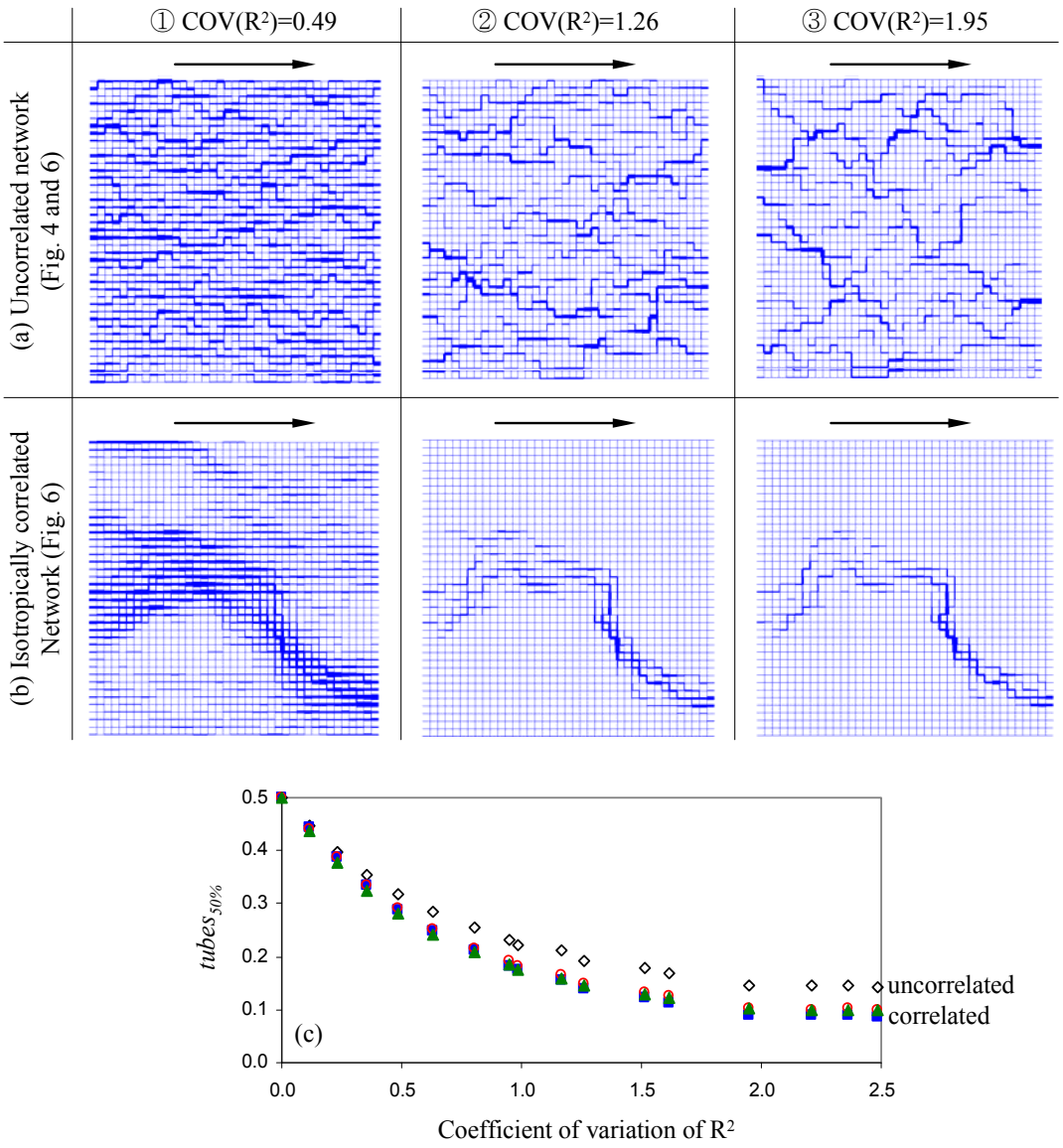

Figure 2.9. Analysis of flow pattern in network model of log-normal distribution of R^2 (refer to Figure 2.4 and 2.6 for simulation details). (a) Flow intensity in each tube in spatially uncorrelated network. (b) Flow intensity in each tube in spatially correlated networks. Thickness of line represents the intensity of flow rate. (c) Fraction of tubes $tube_{50\%}$ responsible for 50% of total conductivity.

The fraction of parallel tubes which conducts 50% of the total flow, $tubes_{50\%}$, quantifies this observation (Figure 2.8b). The values is $tubes_{50\%}$=50% when all tubes are of the same size, either large or small, which means flow is homogeneous. Fluid preferentially flows along the large tubes so that large tubes are responsible for 50% of the

total flow until the fraction of small tubes exceeds ~65%. The participation of small tubes starts to increase above the large-tube percolation threshold (0.5 - Point ② in Figure 2.8b). In general, flow always seeks the larger tubes.

Distributed tube diameters exhibit a similar response. Most parallel tubes contribute to total flow when the coefficient of variation of R^2 is low (Figure 2.9a ①). Flow becomes gradually localized as COV(R^2) increases and fewer channels contribute to global flow (*tubes*$_{50\%}$ in Figure 2.9c). Consequently, hydraulic conductivity decreases as shown earlier (Figures 2.4 and 2.6). The main effect of spatial correlation is to channel flow along interconnected regions of high conductivity (compare Figures 2.9a and 2.9b, see also Bruderer-Weng et al., 2004 for the effect of different correlation lengths on flow channeling).

Flow patterns in anisotropic networks are shown in Figure 2.10 and 2.11 for 18 realizations with different degrees of anisotropy $\mu(R_P^2)/\mu(R_T^2)$, spatial correlation L_P/L_T, and tube size variability COV(R^2). The number of parallel tubes responsible for 50% of the total flow is included in Figure 2.12 for all cases. Significant flow takes place along transverse tubes when transverse tubes are much more conductive than parallel tubes $\mu(R_P^2) \ll \mu(R_T^2)$ (Figure 2.10a), or when there is high transverse correlation $L_P/L_T \ll 1$ (Figure 2.11a - upper bound was labeled "series-of-parallel" configuration in Figure 2.5). On the other hand, there is virtually no flow along transverse paths when parallel tubes are much larger than the transverse tubes $\mu(R_P^2) \gg \mu(R_T^2)$ (Figure 2.10c) or when there is high longitudinal correlation $L_P/L_T \gg 1$ (Figure 2.11c); in these cases, flow localizes along linear flow paths and global conductivity is limited by the smallest tubes along their longitudinal paths (third row in Figures 2.10 and 2.11 - referred to the "parallel-of-series" bound in Figure 2.5). Therefore, the number of parallel tubes responsible for most of the flow decreases with increasing COV(R^2) in this case as well.

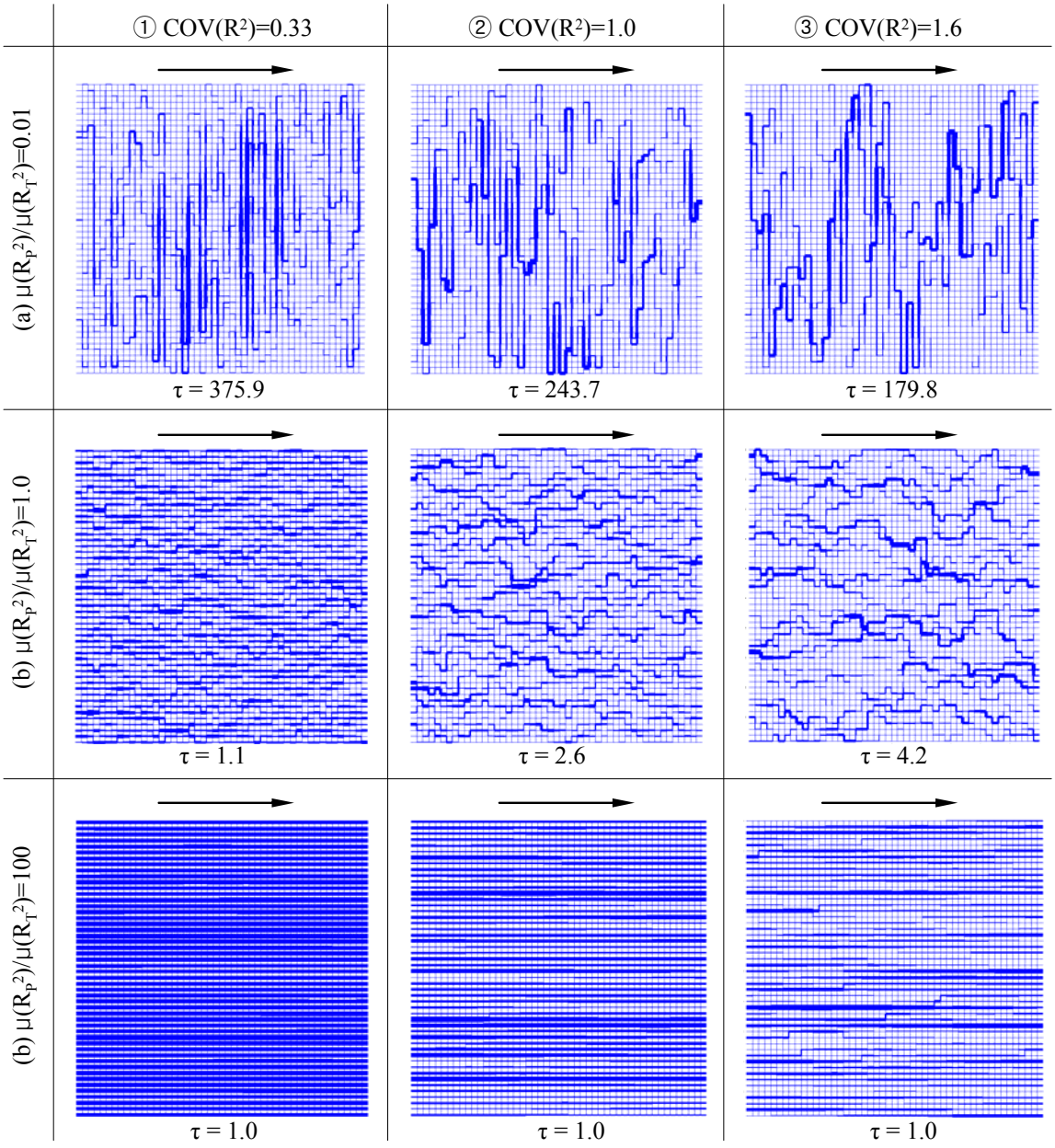

Figure 2.10. Analysis of flow patterns in anisotropic networks made of tubes with the same mean size $\mu(R^2)$ but different variance in size as captured in $COV(R^2)$ (refer to Figure 2.5 for simulation details). Anisotropy ratios: (a) $\mu(R_P^2)/\mu(R_T^2)=0.01$, (b) $(R_P^2)/\mu(R_T^2)=1.0$, (c) $\mu(R_P^2)/\mu(R_T^2)=100$. The arrow indicates the global flow direction. The line thickness used to represent the tubes is proportional to the flow intensity in each tube. Tortuosity values τ are shown for each case.

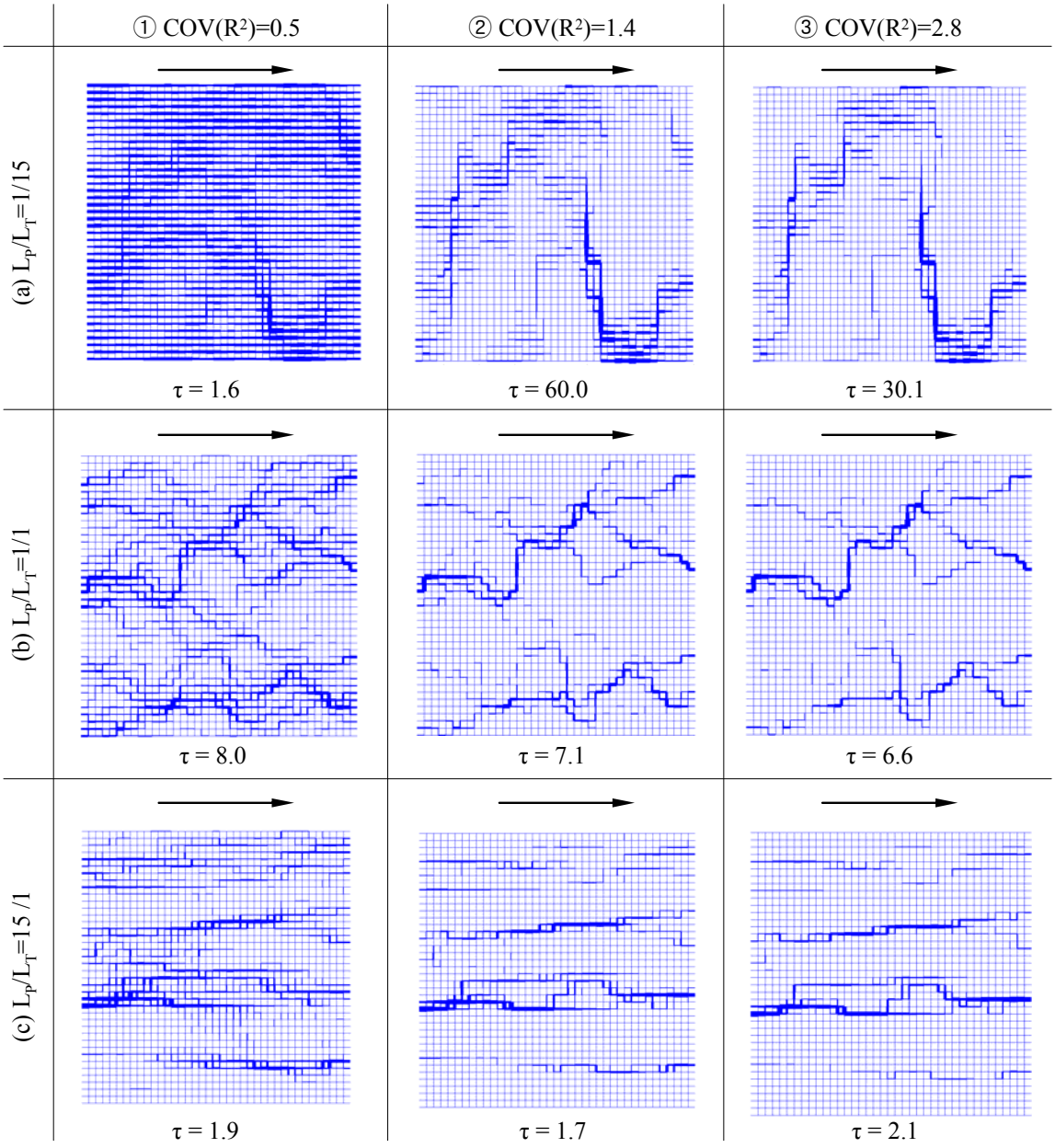

Figure 2.11. Analysis of flow pattern in anisotropically correlated networks made of three sets of tube areas with different COV(R^2) (refer to Figure 2.7 for simulation details). Anisotropy ratios: (a) L_P/L_T=1/15, (b) L_P/L_T=1/1, and (c) L_P/L_T=15/1. The arrow indicates the global flow direction. The line thickness used to represent the tubes is proportional to the flow intensity in each tube. Tortuosity values τ are shown for each case.

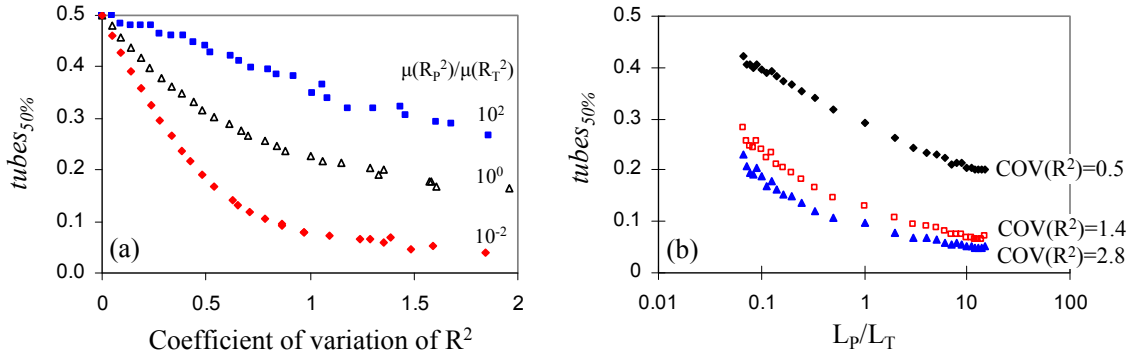

Figure 2.12. Fraction of tubes *tubes*$_{50\%}$ carrying 50% of the total flux as a function of (a) coefficient of variation of R^2 in anisotropically uncorrelated field and (b) the ratio of parallel to transverse correlation length L_P/L_T.

Let's define the network tortuosity factor as the ratio $\tau=(N_{CP}/N_{hom})^2$ between the total number of tubes in the backbone of the critical path N_{CP} and the number of tubes in a straight streamline parallel to the global flow direction N_{hom} [details in David, 1993]. A critical path analysis in terms of tube flow rate is used to compute the tortuosity factors for fluid flow (see Bernabé and Bruderer, 1998). Figure 2.10 and 2.11 show flow patterns and associated tortuosity values. In agreement with visual patterns, there is a pronounced decrease in tortuosity when $\mu(R_P^2)>>\mu(R_T^2)$ in anisotropic uncorrelated fields (Figure 2.10) or when $L_P/L_T>>1$ in anisotropic correlated fields with high $COV(R^2)$ (Figure 2.11).

Spatial correlation reduces the probability of small tubes being next to large ones, and leads to more focused channeling of fluid flow through the porous network. This can be observed by visual inspection of cases shown in Figure 2.11 in comparison to the corresponding ones in Figure 2.10.

Tube length variability. Simple geometrical analyses show that the distance between adjacent pore centers is 2R for simple cubic packing and face-centered cubic packing, and $\sqrt{1.5}\,R$ for tetrahedral packing, where R is the grain radius [see also Lindquist et al., 2000]. However, the constant tube length assumption made in this study is only an idealization for

real sediments [Bryant et al., 1993]. For example, the distance between adjacent pore centers in Fontainebleau and Berea sandstones ranges from 20 to 600μm with most tube lengths between 130 and 200μm [Lindquist et al., 2000; Dong and Blunt, 2009].

While pore-to-pore distance varies in real sediments, we note that the hydraulic conductivity of tubes is much more dependent on the radius than on the tube length (see Equation 2.4). Therefore, the imposed variability in tube radius causes variability in tube conductivity q that could equally capture tube length variability. Clearly, variations in tube length would imply a non-regular network topology.

2.6 Conclusions

Grain size and formation history dependent pore size distribution and spatial variability determine the hydraulic conductivity, immiscible fluid invasion and mixed fluid flow, resource recovery, storativity, and the performance of remediation strategies. Numerical simulations with porous networks permit the study of pore-size distribution, spatial correlation and anisotropy on hydraulic conductivity and flow patterns in pervious media.

In most cases, the hydraulic conductivity decreases as the variance in pore size increases because flow becomes gradually localized along fewer flow paths. As few as 10% of pores may be responsible for 50% of the total flow in media with high pore-size variability. The equivalent conductivity remains within Hashin and Shtrickman bounds.

Spatial correlation reduces the probability of small pores being next to large ones. There is more focused channeling of fluid flow along interconnected regions of high conductivity and the hydraulic conductivity is higher than in an uncorrelated medium with the same pore size distribution.

The equivalent hydraulic conductivity in anisotropic correlated media increases as the correlation length parallel to the flow direction increases relative to the transverse correlation. The hydraulic conductivity in anisotropic uncorrelated pore networks is

bounded by the two extreme “parallel-of-series” and “series-of-parallel” tube configurations. Flow analysis shows a pronounced decrease in tortuosity when pore size and spatial correlation in the flow direction are higher than in the transverse direction.

While Poiseuille flow defines the governing role of pore size on hydraulic conductivity, the numerical results presented in this manuscript show the combined effects of pore size distribution and variance, spatial correlation, and anisotropy (either in mean pore size or in correlation length). In particular, results show that the proper analysis of hydraulic conductivity requires adequate interpretation of preferential flow paths or localization along interconnected high conductivity paths, often prompted by variance and spatial correlation. The development of flow localization will impact a wide range of flow related conditions including the performance of seal layers and storativity, invasion and mixed fluid flow, contaminant migration and remediation, efficiency in resource recovery, the formation of dissolution pipes in reactive transport, and the evolution of fine migration and clogging.

CHAPTER 3

EVOLUTION OF SATURATION AND RELATIVE PERMEABILITY DURING GAS INVASION AND NUCLEATION

3.1 Introduction

Gas and water permeabilities control gas recovery efficiency and determine the economic development of hydrate bearing sediments [Johnson et al., 2011; Minagawa et al., 2004; Minagawa et al., 2007; Gupta, 2007; Kleinberg et al., 2003]. While it would appear that gas and water permeabilities during hydrate dissociation should depend on initial hydrate distributions, there is no laboratory data or numerical simulation result to guide the selection of adequate parameters for reservoir simulations.

The study of unsaturated soil behavior has led to the development of expressions for degree of saturation S and permeability k_r as a function of capillary pressure P_c [Corey, 1954; Brooks and Corey, 1964; Stone, 1970, van Genuchten, 1980]. These P_c-S expressions can be used to investigate similar conditions in resource recovery such as oil production and the injection of liquid CO_2 into water-saturated sediments.

The air-vapor phase is continuous in unsaturated soils, where the gas-vapor phase invades the medium from a boundary, i.e., "external gas drive process". However, gas comes out of solution and bubbles grow within the sediment in methane production from hydrate bearing sediments, i.e., "internal gas drive process" (Note: this situation also takes place in seepage conditions downstream of earth dams). These two cases are referred to as "internal gas drive process" for the case of nucleation and gas liberation during depressurization, and "external gas drive process" or gas injection, for the case of forced invasion [Yortsos and Parlar 1989, Poulsen et al. 2001, Nyre et al., 2008].

The manuscript first introduces and summarizes previous studies. Then, we use a micromodel to gather unprecedented experimental data, and tube-network models for

numerical simulations that explore differences between gas invasion and gas nucleation on the evolution of the soil water saturation and relative permeabilities.

3.2 Previous studies

The development of governing equations for unsaturated soils has centered on changes in saturation as a function of capillary pressure (known as "soil water characteristic curve"), the evolution in relative water and gas permeabilities with saturation, and ensuing mechanical implications (i.e., effective stress, stiffness and strength). The first two are reviewed next.

3.2.1 Soil water characteristic curve

The soil water characteristic curve SWCC captures the causal link between water saturation and capillary pressure [see also Wilkinson and Willemsen, 1983; Lenormand and Zarcone, 1985]. The soil water characteristic curve is also referred to as the soil water retention curve, soil water release curve, capillary pressure curve, or the suction water content relationship [Leong and Rahardjo, 1997; Fredlund, 2002; ASTM D6836-02]. The wetting and drying processes result in different soil water characteristic curves. The ASTM standard method deals only with the drying cycle due to experimental difficulties in obtaining SWCC measurements during wetting [Hillel, 1980]. The relation between capillary pressure and water saturation is usually obtained by applying a vacuum or air pressure to a soil sample or drying the soil sample under controlled relative humidity.

Pore throat size distribution, spatial correlation, soil fabric, contact angle, and interfacial tension affect the shape of the characteristic curve [Francisca and Arduino, 2007; Mitchell and Soga, 2005]. The air entry value is the pressure when decisive de-saturation begins. The air entry pressure increases as pore size decreases and it is much higher for fine-grained sediments than it is for coarse-grained sediments.

Table 3.1. Water saturation in hydrate bearing sediments as a function of capillary pressure P_c=P_g-P_w

Equation		Factors used in hydrate bearing sediment study					References
		Relative saturation $\overline{S}$	S_{mxw}	S_{rw}	P_0	m or λ	
van Genuchten (1980)	$P_c = P_0\left[\overline{S}^{-\frac{1}{m}} - 1\right]^{1-m}$	$\overline{S} = \frac{S_w - S_{rw}}{S_{mxw} - S_{rw}}$	1	0.14	/	0.46	Gamwo and Liu (2010)
			/	/	0.1MPa	0.45	Moridis and Reagan (2007[a]) Moridis and Reagan (2007[b])
			/	0.19	2kPa	0.45	Moridis and Sloan (2007)
			/	/	0.1MPa	0.45	Moridis et al. (2009)
			/	/	5kPa	0.77	Moridis et al. (2010) Reagan et al. (2010)
			/	0.19	2kPa	0.45	Reagan and Moridis (2008)
			1	/	2kPa	0.45	Rutqvist and Moridis (2007)
		$\overline{S} = \frac{S_w - S_{rw}}{1 - S_{rg} - S_{rw}}$	S_{rg}=0.5	0.3 0.2	1kPa	0.45	Hong and Pooladi-Darvish (2003) Uddin et al. (2008)
Corey (1954)	$P_c = P_0\overline{S}^{\lambda}$	$\overline{S} = \frac{S_w - S_{rw}}{1 - S_{rw}}$	/	/	/	- 0.5	Corey (1954)
			/	/	/	- 0.65	Liang et al. (2010)
		$\overline{S} = \frac{S_w - S_{rw}}{1 - S_{rg} - S_{rw}}$	S_{rg}=0.1	0.1	5kPa	- 0.25	Konno et al. (2010)

Note: (1) S_{mxw}: maximum water content, S_{rw}: residual water content, P_0: air entry value, m: van Genuchten equation's fitting parameter, and λ: pore size distribution index. (2) Factors depend on soil type: the finer the soil is, the higher P_0 is. (3) /: not reported.

There are several analytical expressions to capture the soil water characteristic curve in terms of the capillary pressure P_c as a function of relative water saturation $\overline{S}$ = (S_w-S_r)/(1-S_r) where S_w is the water saturation and $\underline{S_r}$ is the residual water saturation [Corey, 1954; Brooks and Corey 1954; van Genuchten, 1980; Fredlund and Xing 1994]. Two popular equations are from Brooks-Corey (1954) and van Genuchten (1980):

$$P_c = P_0\left(\frac{S_w - S_r}{1 - S_r}\right)^{\lambda} \qquad \text{Books-Corey (1964)} \qquad (3.1)$$

$$P_c = P_0\left[\left(\frac{S_w - S_r}{1 - S_r}\right)^{-\frac{1}{m}} - 1\right]^{1-m} \qquad \text{van Genuchten (1980)} \qquad (3.2)$$

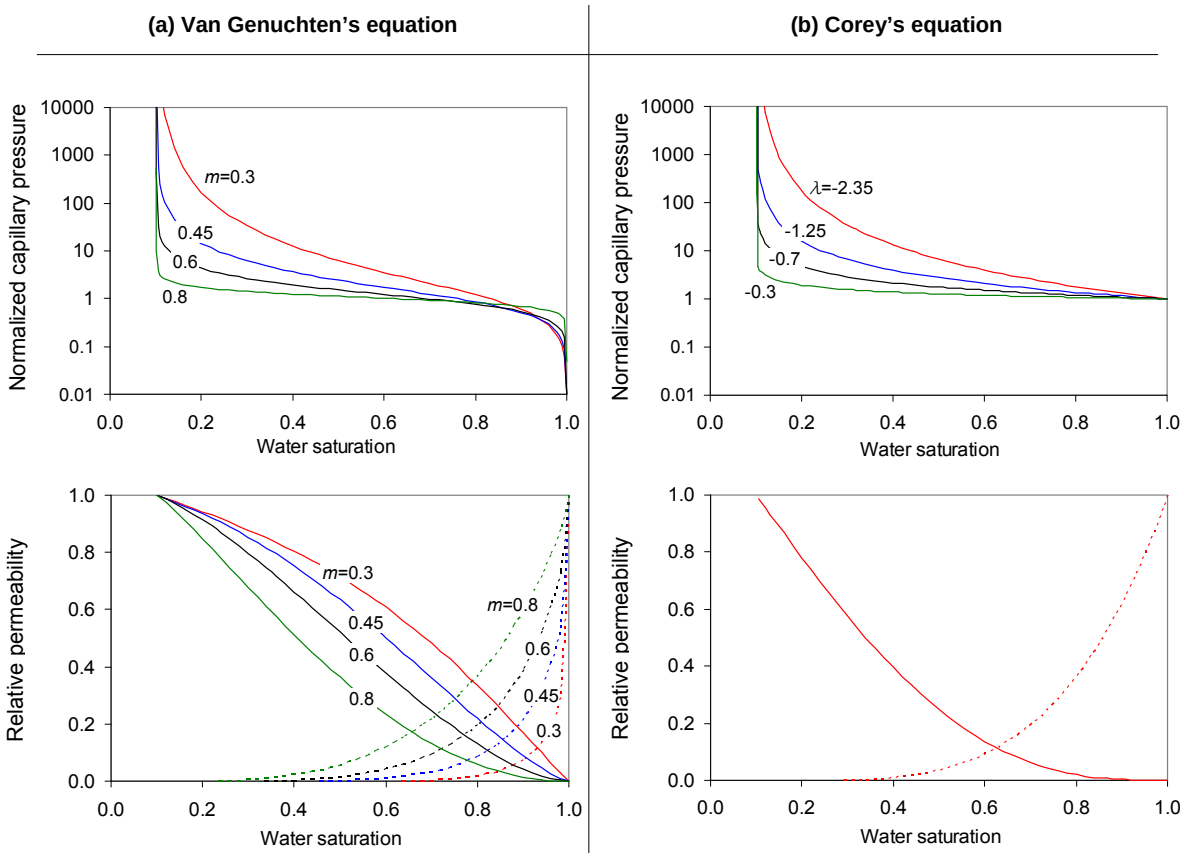

Figure 3.1. Predicted characteristic curves (P_c-*vs*-S_w) and relative permeability trends (k_r-*vs*-S_w). (a) van Genuchten's model. (b) Corey's model. Selected m and λ values shown for each trend. See equations in Table 3.1 & 3.2.

Compiled m-values for European soils (5521 samples) range from m=0.068 for very fine soils, to m=0.342 for coarse soils [Wösten et al., 1999]. Parameters used in hydrate bearing reservoir simulations are compiled in Table 3.1. The effect of different parameters on the soil water characteristic curve is explained in Figure 3.1.

3.2.2 Relative permeability

The relative gas or water permeability k is the value of the property normalized by the corresponding phase conductivity at 100% saturation (or either the non-wetting phase conductivity at irreducible wetting phase saturation, or the wetting phase conductivity at irreducible non-wetting phase saturation [Jaiswal, 2004]). In this study, water conductivity

Table 3.2. Relative permeability equations – Parameters used in published simulations

Equation		Factors used in published hydrate bearing sediment studies				References
		$\overline{S}$	S_{rw}	S_{rg}	m	
van Genuchten (1980)	$k_{rw} = \overline{S}^{0.5}\left[1-\left(1-\overline{S}^{1/m}\right)^{m}\right]^{2}$ $k_{rg} = \sqrt{1-\overline{S}}\left(1-\overline{S}^{1/m}\right)^{2m}$	$\frac{S_w - S_{rw}}{1-S_{rw}}$	0.3	0.05	0.45	Hong and Pooladi-Davish (2003)
			0.2	0.05	0.45	Uddin et al. (2008)
			0.1	-	0.45	Moridis (1998)
					0.386	Hong and Pooladi-Darvish (2005)
Corey (1954)	$k_{rw} = \overline{S}^{4}$ $k_{rg} = \left(1-\overline{S}\right)^{2}\left(1-\overline{S}^{2}\right)$	$\overline{S} = \frac{S_w - S_{rw}}{1-S_{rw}-S_{rg}}$				Nazridoust and Ahmadi (2007)
	$k_{rw} = S_{l,g}^{'\ 4}$ $k_{rg} = S_g^{'\ 2}\left(1-\left(1-S_g^{'}\right)^{2}\right)$	$S_{l,g}^{'} = \frac{S_{l,g}}{1-S_h}$				Tonnet and Herri (2009)
(modified) Stone (1970)	$k_{rw} = \left(\frac{S_w - S_{rw}}{1-S_{rw}}\right)^{n_w}$ $k_{rg} = \left(\frac{S_g - S_{rg}}{1-S_{rg}}\right)^{n_g}$ or $k_{rg} = \left(\frac{S_g - S_{rg}}{1-S_{rw}}\right)^{n_g}$	n_w	n_g	S_{rw}	S_{rg}	
		3.0	3.0	0.15	0.05	Gamwo and Liu (2010)
		4.0	4.0	0.20	0.02	Reagan and Moridis (2008)
		3.0	3.0	0.25	0.02	Moridis and Kowalsky (2005) Moridis et al. (2007)
		3.6	3.6	0.25	0.02	Moridis and Reagan (2007[a])
		3.6	3.6	0.25	0.02	Moridis and Reagan (2007[b])
		4.0	4.0	0.20	0.02	Moridis and Sloan (2007)
		4.0 3.6	4.0 3.6	0.20 0.25	0.02 0.02	Rutqvist and Moridis (2007)
		4.0	4.0	0.20	0.02	Reagan and Moridis (2008) Rutqvist and Moridis (2009)
		3.6	3.6	0.25	0.02	Moridis et al. (2009)
		4.5	3.2	0.24	0	Anderson et al. (2011) Kurihara et al. (2010)
		4.5 -	- 3.2	0.25 0	- 0	Kurihara et al. (2010)
	$k_{rw} = \left(\frac{S_w - S_{rw}}{1-S_{rg}-S_{rw}}\right)^{n_w}$ $k_{rg} = \left(\frac{S_g - S_{rg}}{1-S_{rg}-S_{rw}}\right)^{n_g}$	-	3.0 or 4.0	0.12	-	Gupta (2007)
		3.0	2.0	0.10	0.10	Konno et al. (2010)
		0.2	0.4	-	-	Liang et al. (2010)

at 100% water saturation and gas conductivity at irreducible water saturation are used as reference values.

Models for relative permeability as a function of saturation are intimately related to the soil water characteristic curve models [Brooks and Corey, 1964; Stone, 1970; van

Genuchten, 1980]. The relative permeability equations and fitting parameters used in hydrate bearing reservoir simulations are summarized in Table 3.2. Model predictions and the effect of different parameters on relative permeability are shown in Figure 3.1.

3.2.3 Gas invasion vs. gas nucleation (External vs. Internal gas drive)

The relative gas permeability models proposed for gas invasion may not apply to gas nucleation [Naylor et al., 2000; Grattoni et al., 1998; Egermann and Vizika, 2001]. During external gas drive, gas gradually invades the largest interconnected pores advancing from one boundary into the medium. However, internal gas nucleation takes place at independent pores and results in separate and disconnected bubbles [Poulsen et al., 2001; Egermann and Vizika, 2001] before coalescing to form a continuous gas path. Furthermore, in the case of hydrate dissociation, the dissociated gas distribution must correlate with the initial hydrate distribution.

Network model simulations and experimental studies of gas nucleation from a depressurized heavy oil sample show that gas conductivity by external gas drive exhibits relative gas permeabilities much higher than when gas nucleates in the medium or internal gas drive [Stewart et al., 1954; Naylor et al., 2000; Poulsen et al., 2001; Yortsos and Parlar, 1989; Nyre et al., 2008]. In addition, it is observed that pore connectivity, depressurization rate, and pore size distribution affect the critical gas saturation when a gas cluster percolates, generated gas bubble density, and relative gas permeabilities [Poulsen et al., 2001; Nyre et al., 2008]. The critical gas saturation can be as low as 1% for external gas drive or as high as 10% for internal gas drive [Kamath and Boyer, 1995].

3.3 Experimental study

Experiments with a two-dimensional micromodel in high pressure chamber to validate the evolution of different gas distribution during gas invasion and gas nucleation.

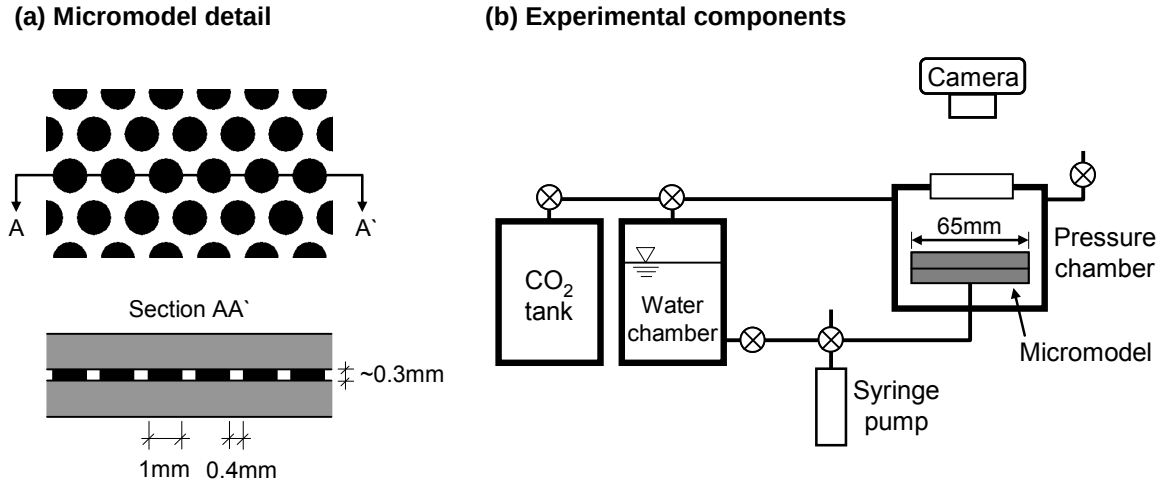

Figure 3.2. Experimental configuration. (a) Micromodel geometry. (b) Pressure chamber and peripheral components.

The introduction about the micromodel, experimental procedure for both gas invasion and gas nucleation processes, and experimental results follow.

3.3.1 Experimental device – Micromodel

A micromodel is constructed using by photo-fabrication and glass etching processes to form a well defined two-dimensional pore structure on the bottom glass plate (Figure 3.2a). A smooth glass plate is bonded on top. The periphery of the micromodel is not sealed to allow for radial flow. The diameter and thickness of pores are d=0.4mm and t=0.3mm. Glass plates are naturally water-wet. The micromodel is housed inside a high-pressure chamber. A detailed experimental configuration is shown in Figure 3.2b. During experimentation, water and air are injected through the port at the center of the bottom glass plate using a syringe pump. A transparent sapphire window at the top of the high-pressure chamber allows the use of time-lapse photography to monitor the evolution of unsaturation.

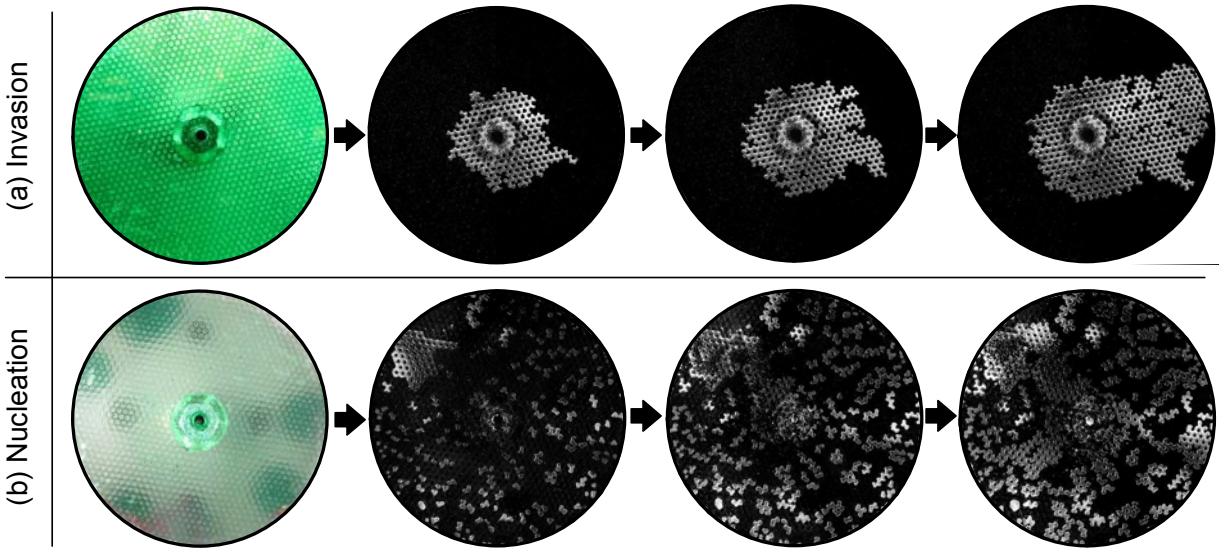

Figure 3.3. Evolution of gas saturation – differential images. (a) Gas invasion into water-saturated micromodel - Inlet port connected at the center of the bottom plate. (b) Gas nucleation during depressurization of CO_2-saturated water.

3.3.2 Experimental procedure and results

For the gas invasion test, the micromodel is saturated with water dyed as green. Then, air is introduced through the central port connected to the bottom glass plate. Air invades the micromodel and gradually forms a preferential air flow path until it percolates to the periphery. At the same time, water is displaced and drains freely until air percolation takes place (Figure 3.3a).

For the gas nucleation test, water saturated with CO_2 at high pressure (P=2.4MPa) is injected into the micromodel using a syringe pump. Once the micromodel is saturated with CO_2-dissolved water, the pressure inside the chamber is increased to dissolve any remaining CO_2 gas. Finally, the chamber pressure is decreased and the evolution of unsaturation is recorded using time-lapse photography. As the pressure decreases, the initially dissolved carbon dioxide evolves to form isolated gas bubbles that displace the water within the micromodel. Further depressurization provokes coalescence. Eventually, gas bubbles percolate (Figure 3.3b).

3.4 Numerical study

Tube-network model and simulation algorithms are developed to complement the experimental study. The network model can simulate gas invasion and nucleation process. The soil water characteristic curves and relative permeability for both cases are obtained and compared.

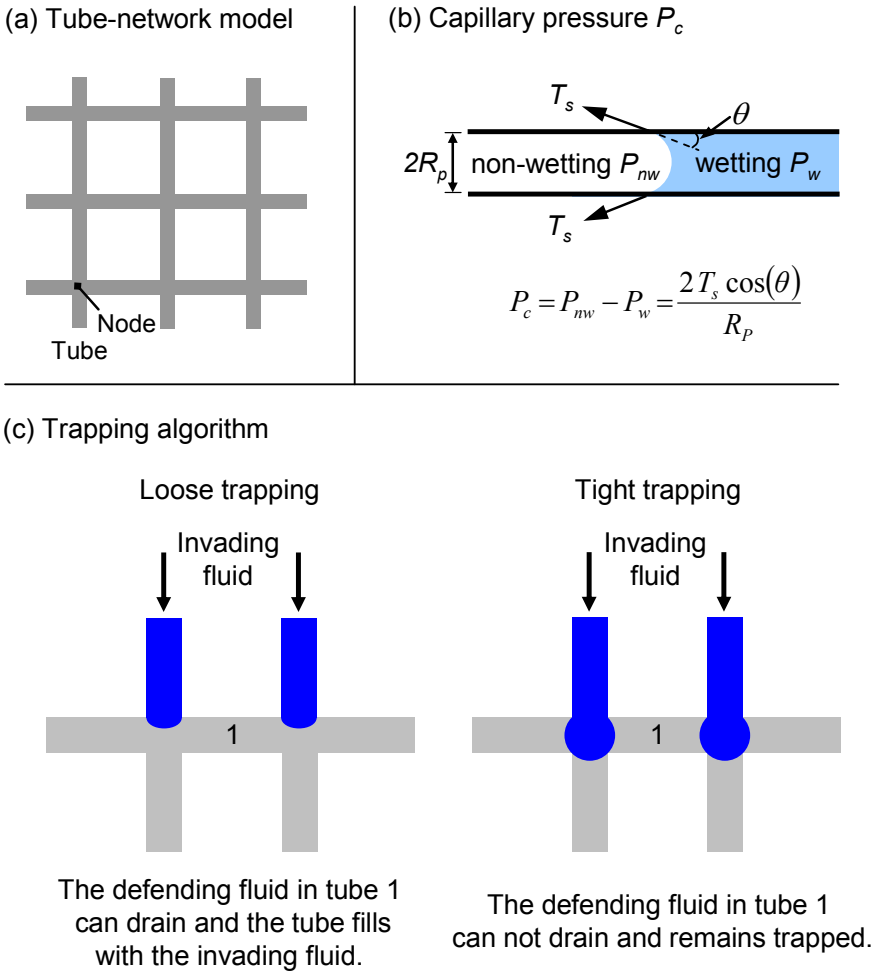

Figure 3.4. Tube network model: Simulation algorithm. (a) Regular tube geometry. (b) Displacement mechanism: the invading phase displaces the defending phase by piston-type displacement. (c) Trapping algorithm: the defending phase in tube #1 is displaced in the "loose trapping" algorithm, but it remains trapped in the tube when the "tight trapping" algorithm is used.

3.4.1 Tube-network model

The tube-network model (Figure 3.4a) consists of tubes connected at nodes. The model can be used to simulate fluid flow through pervious materials [Fatt 1956; see also blunt 2001 for a comprehensive review of network models]. Mixed fluids give rise to capillary pressure P_c which is the pressure difference between the wetting P_w and non-wetting P_g fluids; in a tube of radius R_p, the capillary pressure is captured by the Laplace equation $P_c=P_g-P_w=2T_s\cos(\theta)/R_p$ where T_s is a surface tension and θ is a contact angle (Figure 3.4b).

In order to simulate real sediments, the tube radius R is log-normally distributed. The standard deviation in logarithmic scale of tube radius $\sigma[\ln(R/[\mu\text{m}])]$ is about 0.4±0.2 as observed in natural sediments [Phadnis and Santamarina, 2011]. The same set of tubes and network is used to explore both gas invasion and nucleation.

3.4.2 Simulation procedure

We assume slow invasion and nucleation so that capillary forces control the evolution of unsaturation, that is, both viscous and gravitational forces are disregarded. Gas invasion is enforced at nodes along one boundary plane, while gas nucleation is initiated by injecting gas at randomly selected internal nodes to mimic gas generation from hydrate dissociation in sediments. In both cases, the non-wetting phase is injected until the wetting fluid no longer drains. The algorithms, tube size distributions, and spatial arrangement of the network are identical in both invasion and nucleation simulations. Results are described in terms of the defending fluid retention and relative permeability. Relative permeability at a given saturation is calculated using the Hagen-Poiseuille equation, solving for the pressure at every node, and computing tube-flow across any section [Jang et al., 2011]. The same procedure is used for either fluid once it percolates.

Trapping algorithm. When gas invades a water-saturated micromodel, water may remain trapped in a tube between two air invaded nodes. Two different trapping algorithms are used to capture water displacement/trapping mechanism (Figure 3.4c). The loose trapping algorithm assumes that the invading fluid does not occupy nodes, therefore the water in tube #1 can drain during the invasion process (Figure 3.4c left). However, the tight trapping algorithm assumes that the invading fluid occupies the nodes so that water in an air-bounded tube cannot be drained when gas has invaded both ends (tube #1 in Figure 3.4c right). Displacement/trapping in real systems falls in between these two extreme cases. Therefore, both algorithms are considered in this study.

3.4.3 Simulation results

Effect of trapping algorithm. A three-dimensional tube-network model (13×13×13) is used to study the effect of the trapping algorithm during gas invasion (network details listed in the figure caption). It can be observed that: (1) the residual gas saturation is higher when the tight trapping algorithm is used rather than the loose trapping algorithm (Figure 3.5a); (2) the gas conductivity during gas invasion obtained by the loose trapping algorithm is higher than that obtained by the tight trapping algorithm (Figure 3.5b); (3) gas percolation thresholds ($S_g \approx 0.15$) and water permeabilities during gas invasion are similar for both algorithms (Figure 3.5c). We anticipate that the numerical simulation results are very dependent on the chosen trapping algorithm, and the combination of these trapping algorithms happens in real sediment.

The lower-bound characteristic curve *lb* is determined by sorting the tubes and gradually invading the network from the largest tubes to the smallest ones. Conversely, the upper-bound *ub* is obtained by invading the smallest tubes first and traversing through the

sediment as gradually larger tubes are invaded (green line in Figures 3.5a, 3.6a, and 3.7a). Real cases fall in between these two extremes.

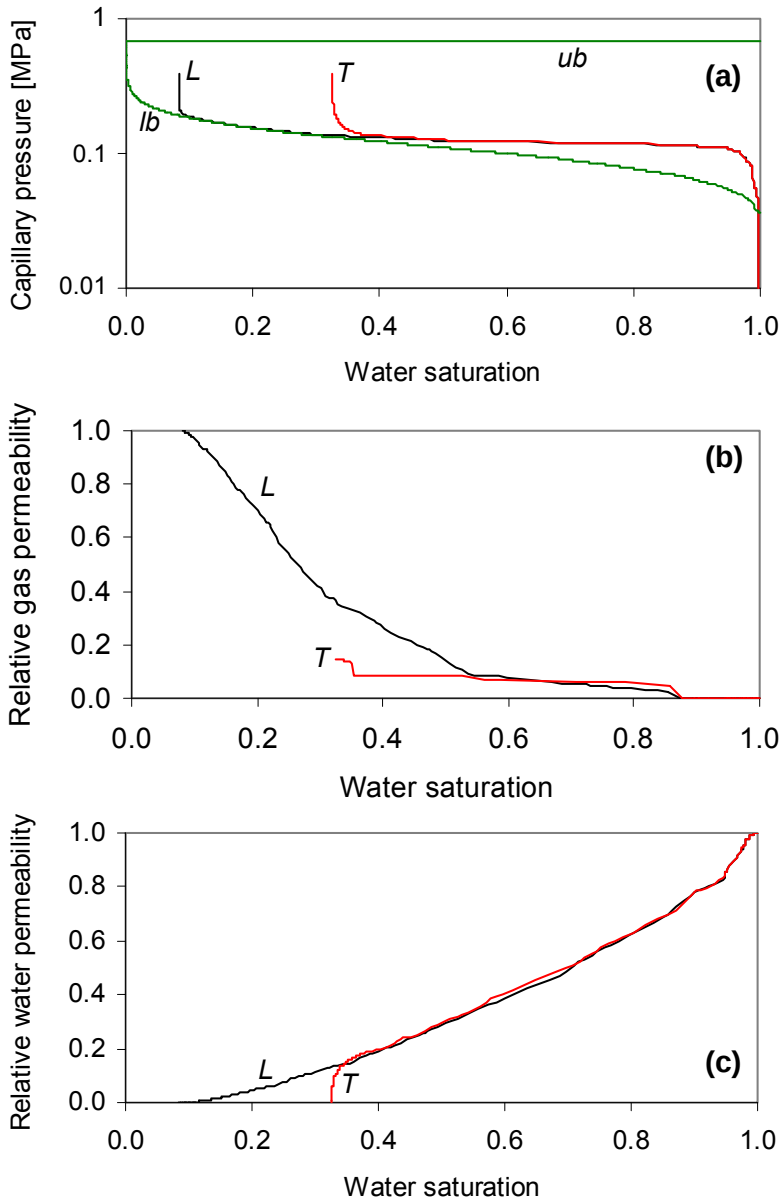

Figure 3.5. Gas invasion: Effect of loose and tight trapping algorithms on the characteristic curve and relative permeability trends. (a) Characteristic curve. (b) Relative gas permeability. (c) Relative water permeability. Results are obtained using a three-dimensional tube-network model: 13×13×13 nodes, 5460 tubes, coordination number cn=6, log-normal distribution of tube radius R, the mean tube size $\mu(R)$=1μm, and the standard deviation in tube radius in logarithmic scale σ(ln(R/[μm]))=0.4. Parameters for Young's equation $P_c=2T_s\cos/R$: T_s=72mN/m, θ=0°.

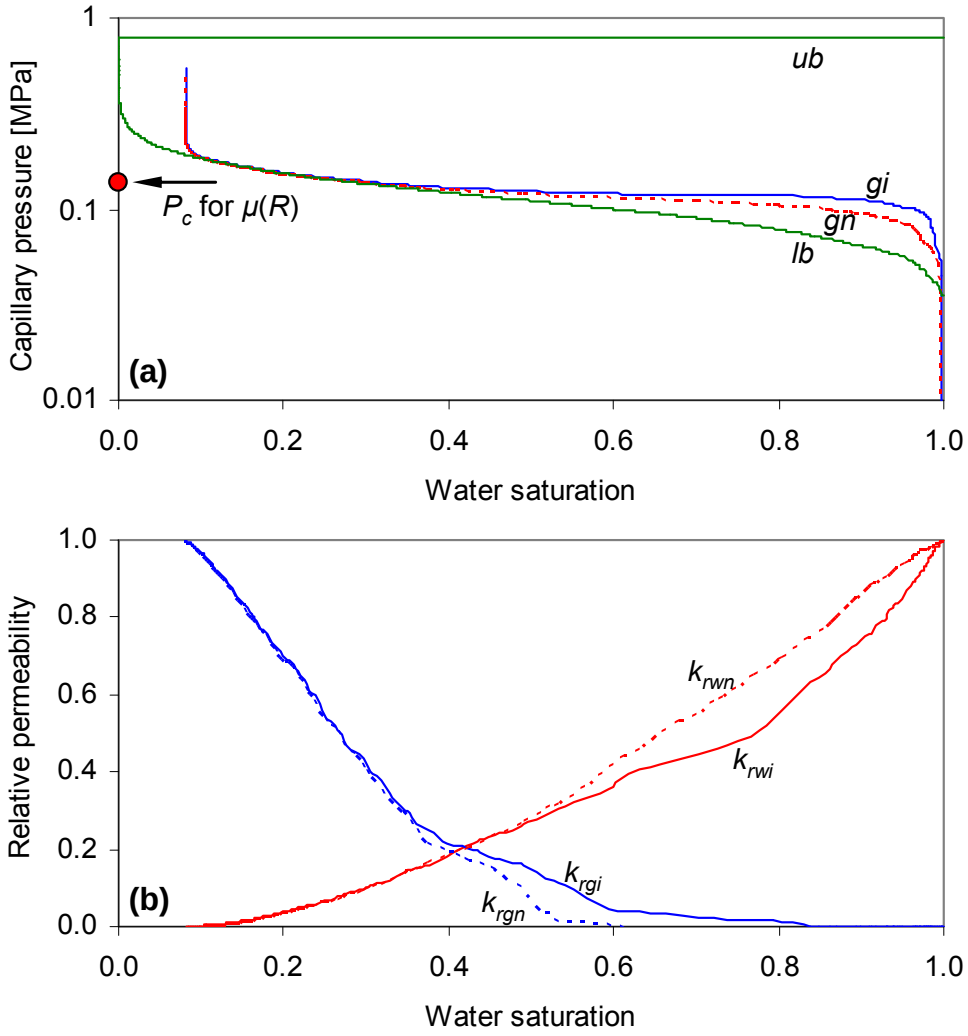

Figure 3.6. Characteristic curves and relative permeabilities during gas invasion "gi" and internal gas nucleation "gn" obtained using the loose trapping algorithm. (a) Characteristic curves. (b) Relative permeabilities. Results are obtained using a three-dimensional tube-network model: 13×13×13 nodes, 5460 tubes, coordination number cn=6, log-normal distribution of tube radius R, the mean tube size $\mu(R)$=1μm, and the standard deviation in tube radius in logarithmic scale σ(ln(R/[μm]))=0.4. Parameters for Young's equation $P_c=2T_s\cos/R$: T_s=72mN/m, θ=0°. For gas invasion, gas is injected through a total of 13^2 nodes on one boundary side of tube-network whose node size is 13×13×13. For gas nucleation, gas is injected through a total of 13^2 nodes distributed inside the tube-network. The lower bound characteristic curve "lb" is computed by sorting tubes and gradually invading from the largest pore to the smallest one.

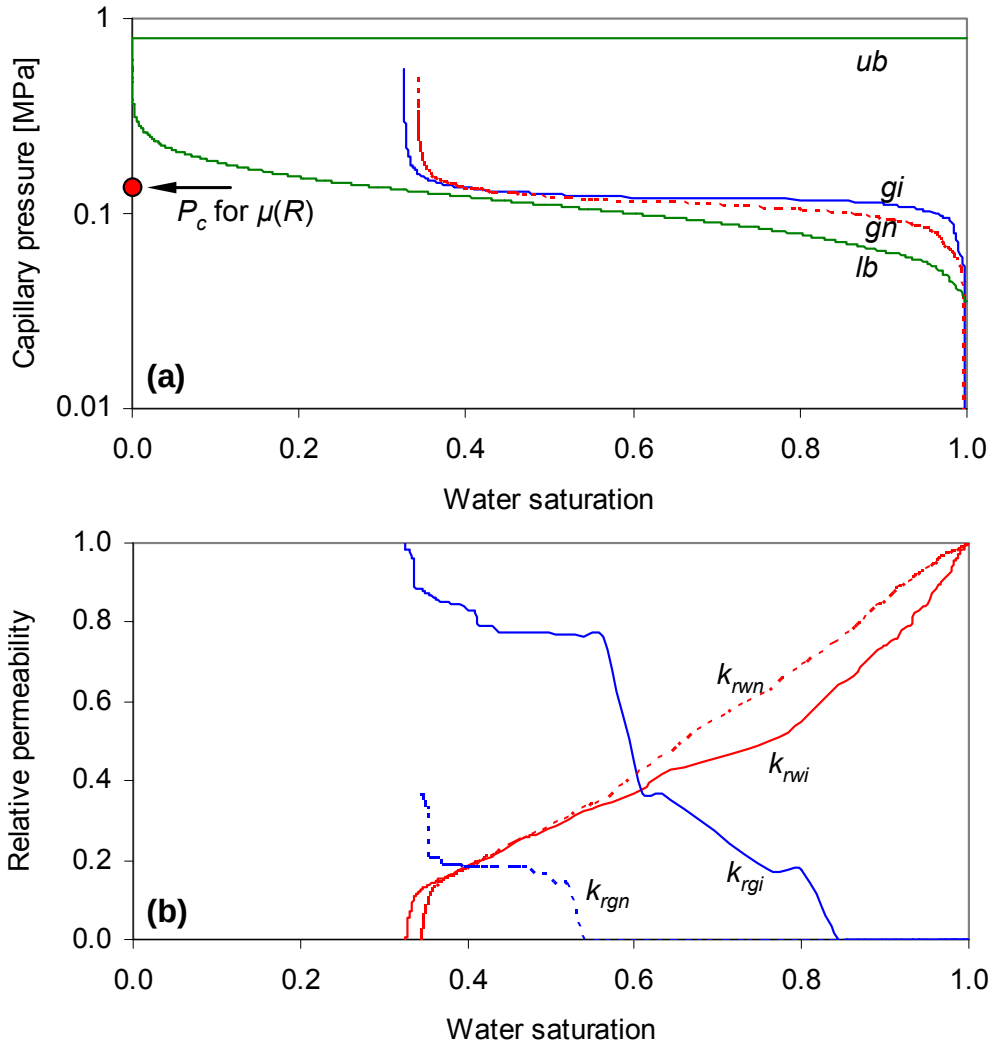

Figure 3.7. Characteristic curves and relative permeabilities during gas invasion "gi" and internal gas nucleation "gn" obtained using the tight trapping algorithm. (a) Characteristic curves. (b) Relative permeabilities. Results are obtained using a three-dimensional tube-network model: 13×13×13 nodes, 5460 tubes, coordination number cn=6, log-normal distribution of tube radius R, the mean tube size $\mu(R)$=1μm, and the standard deviation in tube radius in logarithmic scale σ(ln(R/[μm]))=0.4. Parameters for Young's equation $P_c=2T_s\cos/R$: T_s=72mN/m, θ=0°. For gas invasion, gas is injected through a total of 13^2 nodes on one boundary side of tube-network whose node size is 13×13×13. For gas nucleation, gas is injected through a total of 13^2 nodes distributed inside the tube-network. The lower bound characteristic curve "lb" is computed by sorting tubes and gradually invading from the largest pore to the smallest one.

Soil water characteristic curve. The characteristic curves for spatially-uncorrelated randomly-distributed tubes are shown in Figure 3.6a & 3.7a (network details are summarized in the figure caption). Results are almost identical for gas invasion and gas nucleation, whether tight or loose trapping algorithms are used. Water saturation at gas percolation is slightly higher for gas invasion than for gas nucleation for both algorithms (Figure 3.6b & 3.7b). This can be explained by the lower percolation thresholds of invasion percolation than that of ordinary percolation threshold [Sahimi, 1994; Wilkinson and Willemsen, 1983]. Gas invasion is simulated by invasion percolation algorithm, however gas nucleation process is very similar to ordinary percolation algorithm. When the injecting fluid pressure becomes similar to the capillary pressure of mean tube size (P_c=0.14MPa for this case where $\mu(R_{tube})$=1μm), the water saturation in loose trapping is much lower than in tight trapping. This highlights the relevant effect of selecting the proper algorithm.

Relative permeability by gas invasion and gas nucleation. Gas and water conductivities during gas invasion and nucleation are calculated at every saturation; trends are shown in Figures 3.6b and 3.7b). Computed water conductivities are normalized by the water conductivity of the fully saturated network. Gas conductivities are normalized by the gas conductivity obtained when the gas invasion process is completed, i.e., gas conductivity at the residual water saturation.

The normalized water conductivity for the water saturation range between S_w=0.5 and 1.0 is slightly lower for gas invasion k_{rwi} than for gas nucleation k_{rwn} regardless of which trapping algorithm is used. Likewise, gas permeability simulated by the loose trapping algorithm is slightly higher for gas invasion than for gas nucleation within a saturation range S_w=0.3 to 0.7. However, gas conductivity is much lower for gas nucleation

than it is for gas invasion when the tight trapping algorithm is used. It is because tight trapping algorithm does not allow the coalescence of neighboring gas clusters, which reduces the connectivity among gas clusters. Similar conclusions were reached by Poulsen et al. (2001) using different model characteristics.

3.5 Analyses and Discussion – Tube connectivity

Observation made from experimental and numerical results presented above are analyzed in this section to gain physical insight.

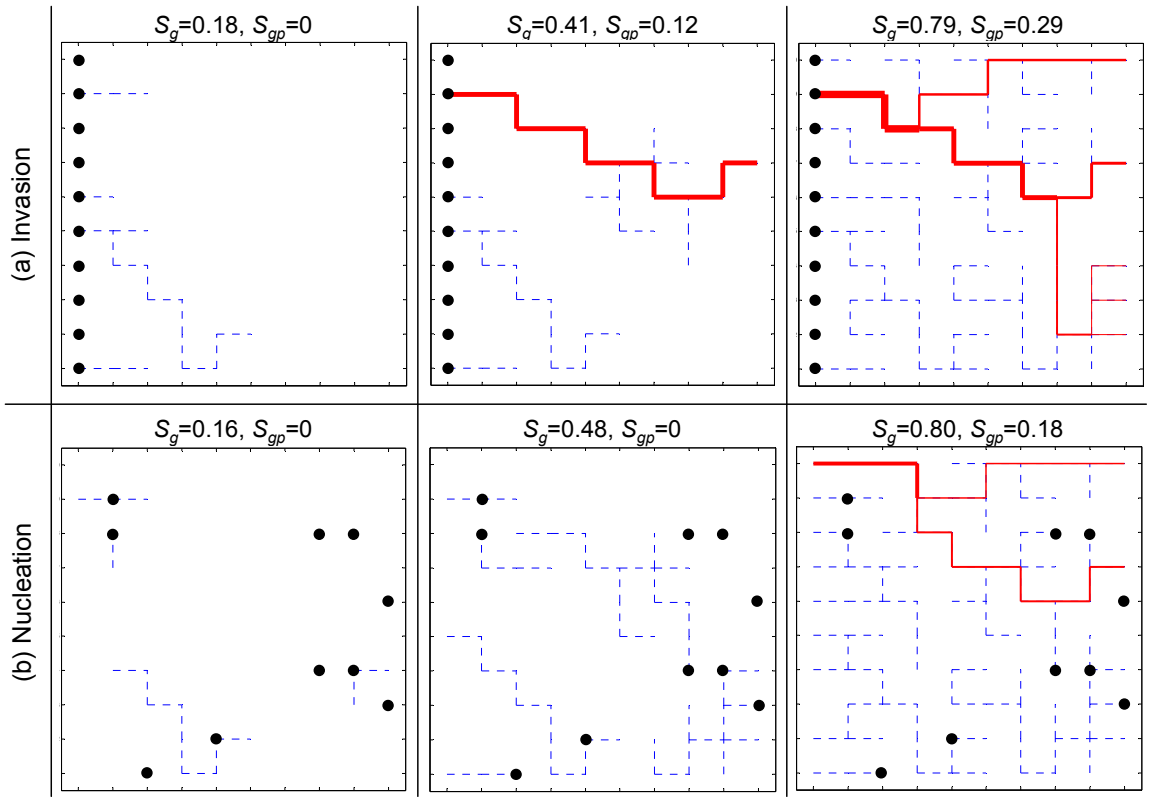

Figure 3.8. Gas invaded tubes (dotted lines) and percolating gas-filled tubes (continuous lines) during (a) gas invasion and (b) gas nucleation at different degrees of saturation. Note: water-filled tubes are not shown for clarity. Gas injection nodes are shown as solid circles. Line thickness is proportional to gas flow rate. Percolating gas saturation S_{gp} is the ratio of the volume of percolating gas-filled tubes to the volume of total tubes. Two-dimensional network model: tight trapping algorithm, 10x10 nodes, 162 tubes, coordination number cn=4, log-normal distribution of tube radius R, the mean tube size $\mu(R)$=1μm, and the standard deviation in tube radius in logarithmic scale $\sigma(\ln(R/[\mu m]))$=0.4. Parameters for Young's equation $P_c=2T_s\cos/R$: T_s=72mN/m, θ=0°.

3.5.1 Tube connectivity in gas invasion and nucleation

Let's simulate gas invasion and nucleation processes in a two-dimensional tube-network model (10×10 nodes) to help visualize flow and underlying process that cause differences in gas permeabilities. Figure 3.8 shows gas invaded tubes (blue dotted lines) and percolating gas-filled tubes (red continuous lines) for gas invasion and nucleation at various gas saturations. The thickness of the red continuous lines is proportional to the flow rate through tubes.

At low gas saturations (first column in Figure 3.8), the gas phase does not percolate in both cases. Gas percolation occurs at a gas saturation S_g=0.41 for the gas invasion process and above S_g>0.48 for gas nucleation (second column in Figure 3.8). Percolating gas clusters are observed at high gas saturation S_g≈0.8 in both the invasion and nucleation processes (third column in Figure 3.8). The thicker lines for gas invasion indicate higher gas flow rates through the tubes.

Let's define the gas saturation at percolation S_{gp} as the ratio of the volume of percolating gas-filled tubes to the total volume of tubes. The value of S_{gp} shows that the effective connectivity of gas-filled tubes is higher for invasion compared to nucleation. This explains the correspondingly higher gas permeability.

3.5.2 Effect of spatial correlation in tube size distribution

The previous simulations were conducted for spatially uncorrelated media. The effect of spatial correlation in tube size on the soil water characteristic curve and relative permeabilities is investigated using two-dimensional uncorrelated and correlated networks (20×20, Figure 3.9). While correlated and uncorrelated fields render relatively similar trends, we note that correlated conditions lead to (1) lower air entry value, (2) show higher water relative permeability. Two-dimensional simulation sometimes does not show gas permeability during gas nucleation process (Figure 3.9a); the simulations using three-dimensional correlated networks are needed.

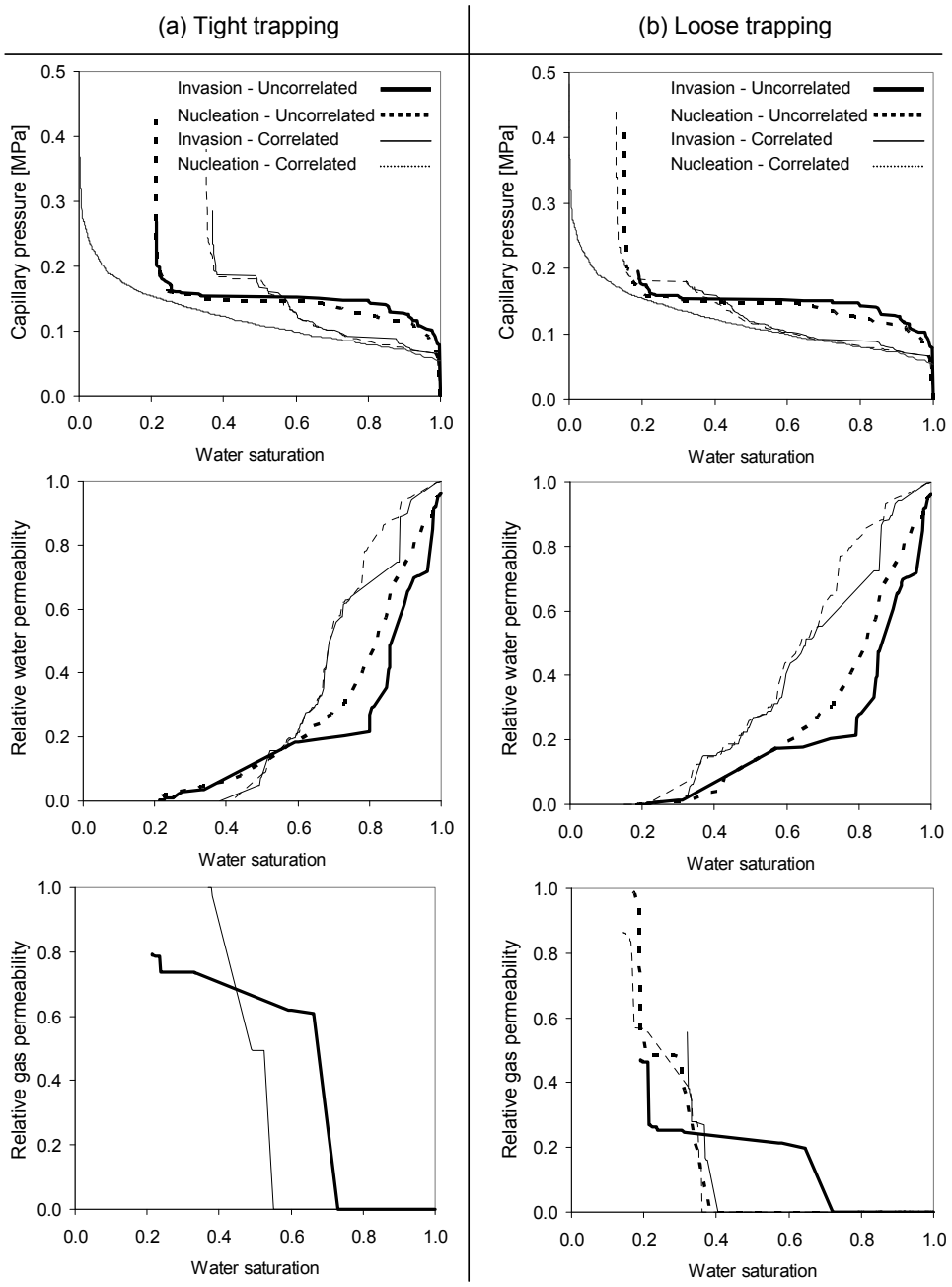

Figure 3.9. Effect of spatial correlation in tube size distribution on soil water characteristic curve and relative permeability using (a) tight trapping and (b) loose trapping algorithm. Uncorrelated and correlated networks are made of an identical set of tubes, and same number and position of injection nodes are used for gas invasion and nucleation simulation. Two-dimensional network model: 20x20 nodes, 722 tubes, coordination number cn=4, log-normal distribution of tube radius R, the mean tube size $\mu(R)$=1μm, and the standard deviation in tube radius in logarithmic scale $\sigma(\ln(R/[\mu m]))$=0.4. Parameters for Young's equation $P_c=2T_s\cos/R$: T_s=72mN/m, θ=0°. Isotropic correlation L/D=0.67 is used where L is correlation length and D is the network size.

3.6 Conclusions

Several models have been proposed to represent the soil water characteristic curve and the variation of relative permeability with saturation. These equations typically apply to gas invasion into a water saturated sediment.

Gas invasion and gas nucleation experiments using micromodels show the evolution of topologically different water and gas distributions as gas saturation increases: invading gas forms a percolating gas path while nucleating gas forms isolated gas clusters.

Numerical results obtained with a tube-network models show that the soil water characteristic curves are similar for gas invasion and nucleation. The evolution of relative water permeability with saturation shows similar trends in both cases as well. However, the evolution of relative gas permeability with unsaturation is strongly dependent on topology of gas distribution, and it is lower for gas nucleation than it is for gas invasion.

In gas nucleation, gas-filled tubes often remain isolated and do not contribute to the global gas conductivity. In other words, the percolating gas saturation S_{gp} is higher for gas invasion than for gas nucleation.

Based on the results, we conclude that existing models such as Corey's and van Genuchten's model can be used for reservoir simulation in the context of gas production from hydrate bearing sediment. However, special attention must be placed when selecting parameters for relative gas permeability. In particular, gas saturation at percolation is higher for gas nucleation than for gas invasion.

CHAPTER 4

PORE-SCALE OBSERVATIONS AND ANALYTICAL STUDIE – HYDRATE FORMATION AND DISSOCIATION PROCESSES

4.1 Introduction

Gas hydrate formation and dissociation behavior affects gas production from hydrate-bearing sediments. Complex hydro-thermo-chemo-mechanically coupled processes are involved in hydrate formation and dissociation. Their comprehension requires a clear understanding of the physical properties at the pore-scale, such as: gas solubility in water and the effect of salt on solubility; interfacial tension under changing pressure and temperature; relative contributions of viscosity and capillarity; hydrate phase boundary shift due to salinity, pore size, and mixed gas conditions; and thermal properties such as specific heat and latent heat of dissociation.

Hydrate formation and dissociation have been studied at the pore-scale using transparent micromodels and the microtomography [Kerkar et al., 2009; Jin et al., 2006; Tohidi et al., 2001; Katsuki et al., 2006; Katsuki et al., 2007; Katsuki et al., 2008]. The study reported here uses micromodels to observe hydrate response at the pore-scale in view of gas production. Two types of transparent micromodels are manufactured. An etched-micromodel is constructed using photo-fabrication and the glass etching processes to form a well defined two-dimensional pore structure on the bottom glass plate; a smooth glass plate bonded to the top (Figure 4.1a). The other one is a grain-based micromodel which consists of mono-sized grains between two smooth glass plates (Figure 4.1b). The periphery of the open micromodel is not sealed to allow for radial flow; however, the periphery of the closed micromodel is sealed to prevent external gas from reacting with water inside the micromodel (Figure 4.1c). The glass plates are naturally water-wet. The

micromodel is housed inside a high-pressure chamber. A detailed experimental configuration is shown in Figure 4.1d.

Experimental observations are complemented with analytical solutions. Simple equations are obtained for preliminary analyses by making assumptions such as mass conservation and adiabatic conditions. Other common equations and relevant dimensionless numbers are used to explain gas solubility, freezing point depression, and mixed fluid flow conditions.

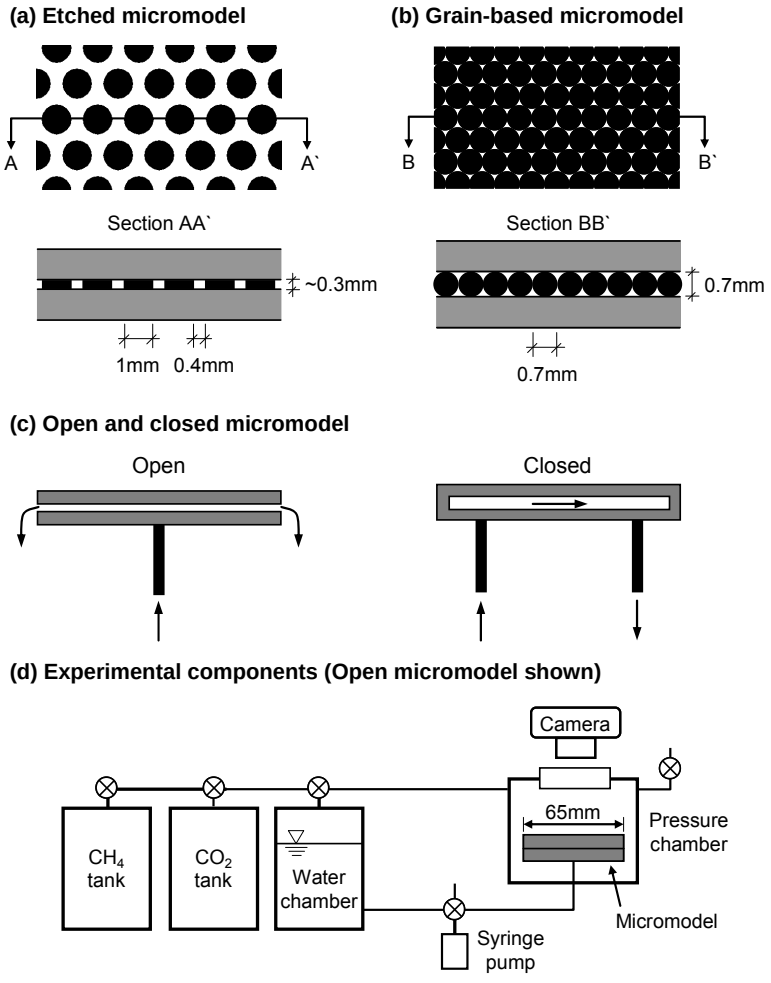

Figure 4.1. Micromodel configuration and experimental component. (a) An etched micromodel. (b) A grain-based micromodel. (c) Open and closed micromodel. (d) Experimental components.

The purpose of this study is to understand and analyze physical properties and pore-scale phenomena relevant to hydrate formation and dissociation. We identify important mechanisms during formation and dissociation and assess their implications on gas production.

4.2 Solubility of hydrate-forming gas in aqueous systems

Component *A* may dissolve or come out of solution from a neighboring component *B* depending on pressure and temperature. When equilibrium is reached, an equal number of molecules will jump A-to-B and B-to-A.

4.2.1 Equilibrium conditions - Controlling factors

The solubility of hydrate-forming gas affects hydrate formation and dissolution in water.

P-T dependent solubility in the absence of hydrate. The pressure and temperature *P-T* dependent concentration of a certain species in another component $M_{P,T}$ [mol/m^3] can be approximated using Henry's law as a linear function of pressure

$$M_{P,T} = P_{applied}\, k_H^0 \cdot \exp\left[\frac{-\Delta H}{R}\left(\frac{1}{T} - \frac{1}{298.15K}\right)\right] \tag{4.1}$$

where the enthalpy of the solution is ΔH=-14130 [J/mol] for CH_4 in water and ΔH=-19940 [J/mol] for CO_2 in water, Henry's law constant at 298.15 [K] is k_H^o=1.3×10^{-3} [M/atm] for methane and k_H^o=3.4×10^{-2} [M/atm] for carbon dioxide [Wilhelm et al., 1977; Osegovic et al., 2006], and the universal gas constant is R=8.314 [J/(mol·K)]. Hence, the solubility of gas in water increases with increasing pressure and decreasing temperature outside the hydrate stability *P-T* conditions.

Competing solutes. Solubility is affected by the presence of other phases or competing solutes. For example, the presence of hydrates facilitates further hydrate formation and the equilibrium concentration of gas in water decreases. The gas solubility trend with respect

to pressure and temperature is also altered by the presence of hydrate. Within the hydrate stability field, a temperature decrease under constant pressure or a pressure increase at constant temperature forces methane molecules in the liquid water to form more hydrate, which reduces the gas solubility in water [Waite et al., 2009; Subramanian and Sloan, 2002; Lu et al., 2008]. Salt is a competing solute for dissolved gas and therefore lowers the solubility of gas in water [Davie et al., 2004; Sun and Duan 2007; Tishchenko et al., 2005; Zatsepina and Buffett, 1998].

Table 4.1. Methane and carbon dioxide solubility in water with and without gas hydrates.

	Without hydrate (C_{bh})		With hydrate (C_{ah})	
	Pure water	Salt water (con. of NaCl)	Pure water	Salt water (con. of NaCl)
Methane concentration [mol/kg]	0.11[a] (273K,3MPa) 0.0974[f] (273K,50MPa)	0.00177[c] (1m) (273K,0.1MPa)	0.065[g] (274K,3.5MPa)	0.05184[e] (273K,10MPa)
	0.12[a] (276K,6.6MPa)		0.066[g] (274K,5MPa)	
	0.13[a] (285K,10MPa)		0.067[g] (275K,6.5MPa)	0.09689[e] (283K,10MPa)
	0.00247[c] (273K,0.1MPa)			
Carbon dioxide concentration [mol/kg]	0.0693[d] (273K,0.1MPa)	0.0557[d] (1m) (273K,0.1MPa)		
	1.39[a] (273K,3MPa) 1.63[b] (273K,3MPa)	1.21[b] (0.6m) (273K,3MPa)	0.89[f] (274K,3.7MPa)	
	1.66[a] (277K,6.6MPa) 1.88[b] (277K,6.6MPa)	1.39[b] (0.6m) (277K,6.6MPa)	1.09[f] (276K,6MPa)	
	1.66[b] (285K,10MPa)	1.25[b] (0.6m) (285K,10MPa)		

a-These values are obtained by extrapolating of solubility without hydrate to lower temperatures [Jung et al., 2010], b-Gas solubility calculator (Duan's group webpage: http://calc.geochem-model.org/Pages/Solubility.aspx), c-Duan and Mao (2006), d-Duan and Sun (2003), e-Sun and Duan (2007), f-Servio and Englezos (2001), g-Servio and Englezos (2002).

Values. Table 4.1 summarizes typical solubility data computed under various pressure and temperature conditions. Generally, the solubility of CO_2 in water is about 10 times greater than that of CH_4.

4.2.2 Implications

The solubility dependence on pressure, temperature, and the presence of hydrate can cause unique phenomena during hydrate formation. Three salient cases are analyzed next.

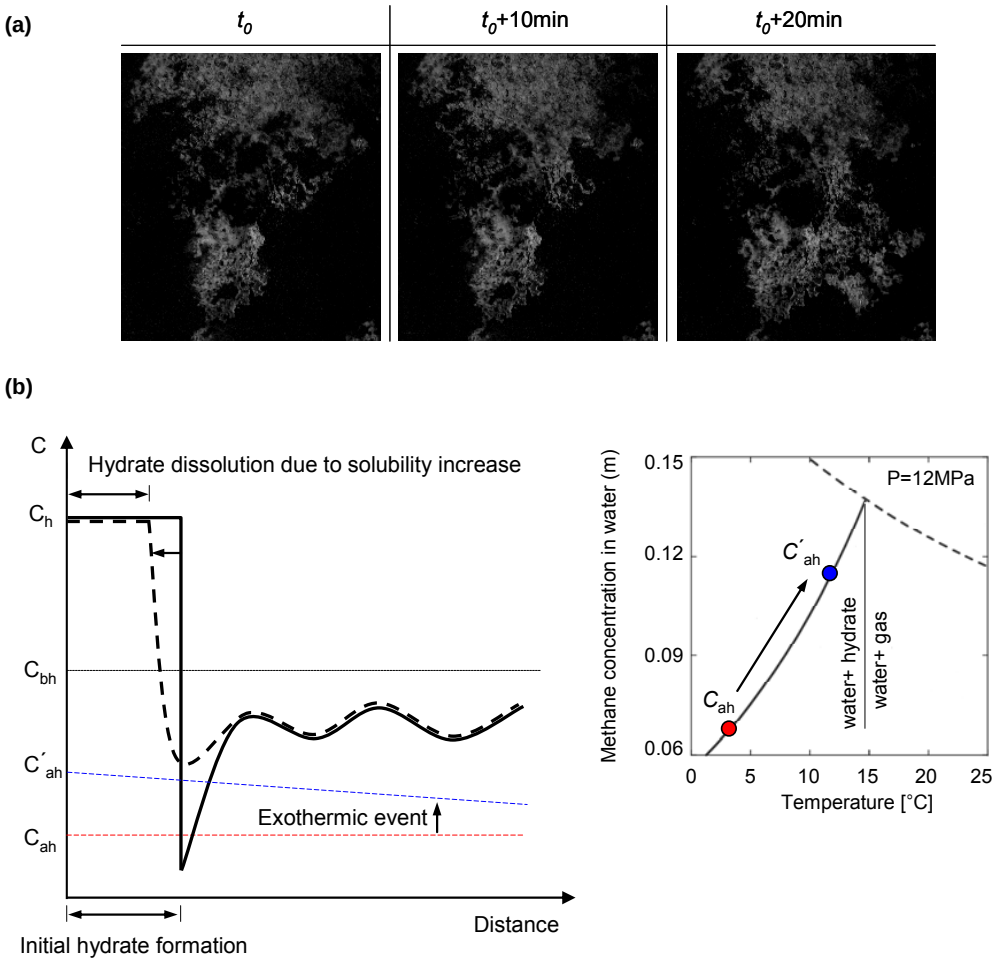

Figure 4.2. Transient hydrate formation and dissolution in the grain-based and closed micromodel. (a) Hydrate forms, dissolves, and re-forms within 20 minutes. (b) Methane concentration change during hydrate formation and dissolution, and subsequent methane solubility change due to endothermic and exothermic events.

Transient hydrate formation. The grain-based closed micromodel is used to form carbon dioxide hydrate at pressure P=3.4MPa and temperature T=2.2°C. Initially, the micromodel is water saturated. Gas is injected into the micromodel to displace some of the water under hydrate stability conditions. Gaseous CO_2 injection triggers local hydrate formation, but the newly formed hydrate mass dissolves into the water increasing the concentration of CO_2 in water. Hydrate suddenly starts to form without any triggering 440 minutes after complete hydrate dissolution. Then, oscillating transient hydrate formation and dissolution occurs during the next 1450 minutes. Snapshots during the first 20 minutes of this behavior are captured in Figure 4.2a (hydrate is shown in white).

Figure 4.2b explains dynamic and transient hydrate formation and dissolution within a gas-limited system. Once hydrate forms, the gas concentration in water near the hydrate mass may be the same (or lower at a transient condition) as the solubility in the presence of hydrate C_{ah}. On the other hand, gas solubility C'_{ah} in water near the hydrate mass will increase due to the temperature increase that results from exothermic hydrate formation (see gas solubility in the presence of hydrate in Figure 4.2b). The hydrate then dissolves again, and the gas solubility may decrease back to C_{ah}. The solubility change due to a temperature change associated with hydrate formation and dissolution and fast formation compared to diffusion (from C-to-C_{ah}) explains the transient formation-dissolution cycles.

Hydrate lens formation. Consider a sediment of initial porosity n_o and a pore water gas concentration C_o surrounded by a closed boundary, i.e., constant mass (Figure 4.3). Let's assume that a hydrate lens forms using the excess gas dissolved in the pore water. The hydrate lens thickness is calculated using the saturated gas concentration in the absence of hydrate C_o, the gas solubility in the presence of hydrate C_{ah}, gas concentration in hydrate C_h and the initial sediment porosity n_0 (Figure 4.3).

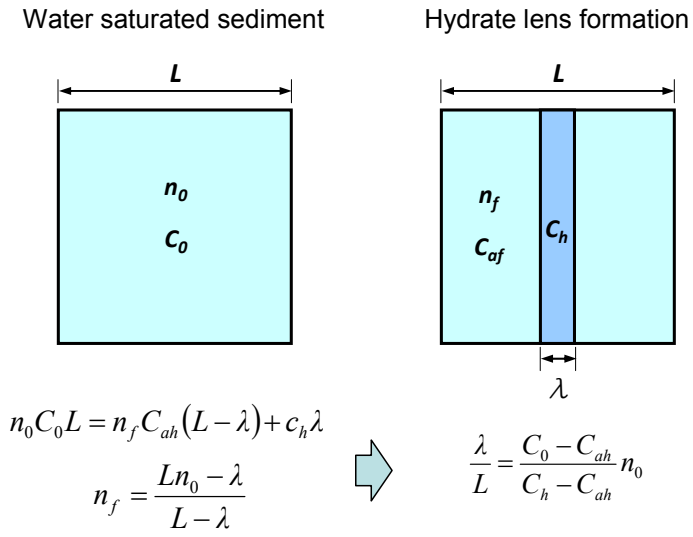

Figure 4.3. Anticipated hydrate lens thickness that could form from the initially dissolved excess gas. Hydrate lens thickness λ in a medium with lens-to-lens spacing L is a function of the initial porosity n_0, gas solubility in the absence and in the presence of gas hydrate c_0 and c_f, and gas concentration in hydrate c_h.

$$\frac{\lambda}{L} = \frac{C_0 - C_{ah}}{C_h - C_{ah}} n_0 \qquad \text{Hydrate lens thickness} \qquad (4.2)$$

For example, a hydrate lens thickness of λ=4mm is anticipated for lenses separated by L=1m in a sediment with an initial porosity n_o=0.4 if the initial methane concentration is C_0=0.14mol/kg (P=12MPa and T=288K), when the methane solubility in the presence of hydrate is C_{ah}=0.063mol/kg, given that the methane concentration in hydrate is C_h=8.06mol/kg (see values in Table 4.1 when P=6.6MPa and T=274K).

Porosity decrease in the sediment surrounding the lens is, once again, invoking mass conservation:

$$n_f = \frac{n_0 - \lambda/L}{1 - \lambda/L} \qquad (4.3)$$

Phenomena near CO_2 injection wellbore - Mutual solubility. Water solubility in liquid CO_2 is 0.063mol/kg at 8.3MPa and 287K [Song and Kobayashi, 1987], which is 1.34g of

water per 1kg of liquid CO_2. Therefore, liquid CO_2 injection during enhanced oil recovery, CO_2 geological storage, or CH_4-CO_2 replacement will remove water from the sediment beyond the irreducible water content after initial displacement. This leads to an increase in CO_2 conductivity. However, salt precipitation will take place in region of irreducible saturation when brines are involved. "Salting-out" will plug pores [Hurter et al., 2008] and CO_2 permeability will not necessarily increase above the level of irreducible saturation.

Methane solubility in liquid CO_2 causes methane hydrate dissolution when liquid CO_2 is injected. Even though the calculated decrease in hydrate saturation is as low as $\Delta S_h \approx 0.001$, the continuous injection of liquid CO_2 near the wellbore can result in substantial hydrate dissolution [Jung et al., 2010].

Table 4.2. Interfacial tension and contact angle.

	Interfacial tension [mN/m]	Contact angle [°]
Water-CO_2 (g)	72[a] (0.1MPa,298K)	38[a] on calcite (0.1MPa, 298K)
Water-CO_2 (l)	30[a] (7MPa, 298K)	30[a] on Calcite (7MPa, 298K)
Water-CH_4 (g)	72[b] (.1MPa, 298K) 64[b] (10MPa, 298K)	105[a] on PTFE (0.1MPa, 298K)
Water-Oil	33[c] H_2O-benzene 49[c] H_2O-mineral oil	98~180[d] on mineral (308-366K)
Water-Ice	32[e] 31.7[f] 29[g]	~0[h] (water on ice)
Water-CH_4 (h)	32[e] 17[g] 39[i]	no data found
Water-CO_2 (h)	30[e] 14[g]	no data found
Water-C_3H_8 (h)	25[g]	no data found
Ice- N_2&O_2 hydrate	41[g&j]	no data found

a-Espinoza and Santamarina 2010; b-Ren et al. 2000, c-Kim and Burgess 2001, d-Treiber et al. 1972, e-Anderson et al. 2003, f-Hillig 1998, g-Uchida et al. 2002, h-Knight 1971, i-Uchida et al. 1999, j-Uchida et al. 1993.

4.3 Interfacial and capillary phenomena

Surface tension and contact angle determine capillary phenomena in porous media. These two parameters and their implications on hydrate-bearing sediments are explored next.

4.3.1 Interfacial phenomena

Surface tension. Induced polarizations become anisotropic for molecules along the inter-phase and a higher van der Waals attraction develops. This situation alters the molecular organization in fluids in a zone that extends for about 5-to-10 mono-layers from the interface. For example, (1) water molecules at the water-vapor interface prefer to be oriented with their negative side facing towards the vapor phase, while random bulk conditions are attained at a distance of 1~2nm from the interface [Butt et al., 2006]; (2) there is preferential alignment of water molecules near interface ions [Bhatt et al., 2004] and of water and CO_2 molecules at the interface [da Rocha et al., 2001; Kuznetsova and Kvamme, 2002; Kvamme et al., 2007]. These molecular-scale phenomena cause the emergence of a contractile membrane along the interface and a measureable surface tension T_s [mN/m] in Liquid-Gas L-G, Liquid-Liquid L_1-L_2 and Liquid-Ice L-I interfaces.

Consider a liquid-gas LG interface. The proximity to and the number of near-neighbor charges depend on gas density. Hence, higher interaction and lower interfacial tension is expected with increased gas pressure and density (Sugden-Macleod equation T_s=f($\Delta\rho$) [Chun and Wilkinson, 1995]). Likewise, the interaction with the external fluid remains relatively constant once the pressure exceeds the vapor-liquid boundary and the gas liquefies. Data for water-CO_2 shows a pronounced sensitivity of interfacial tension on pressure, and relatively constant T_s values when pressure exceeds the CO_2 L-V boundary [Espinoza and Santamarina, 2010]. Table 4.2 summarizes interfacial tension data for mixed fluid conditions such as water-CO_2, water-CH_4, water-oil, water-ice, and water-gas hydrates.

Contact angle. The contact angle formed by two adjacent fluids resting on a mineral substrate reflects the mutual interactions between the three neighboring species [Figure 4.4; Adamson and Gast, 1997]

$$\cos\theta = \frac{T_{VS} - T_{LS}}{T_{LV}} \qquad \text{Young's equation} \qquad (4.4)$$

Table 4.2 provides contact angle data for mixed fluid conditions such as water-CO_2, water-CH_4, water-oil, and water-ice relevant to hydrate-bearing sediments.

The crystalline structure of minerals explains the different affinity for fluids. For example, when crystallization occurs in an aqueous environment, groups with water affinity develop on the surface, and the contact angle that water forms on the crystal is lower than the angle observed in the same mineral crystallized in air [Shaw, 1992].

Changes in interfacial tensions T_{VS}, T_{LS}, and T_{LV} (in particular), with respect to pressure, will alter the contact angle in liquid-gas-mineral systems such as water-CO_2-mineral and water-CH_4-mineral systems. Note that contact angle decreases on hydrophilic surfaces but increases on hydrophobic surfaces when T_{LV} decreases with increasing CO_2 pressure, as anticipated from a force equilibrium analysis (Figure 4.4 – Equation 4.4).

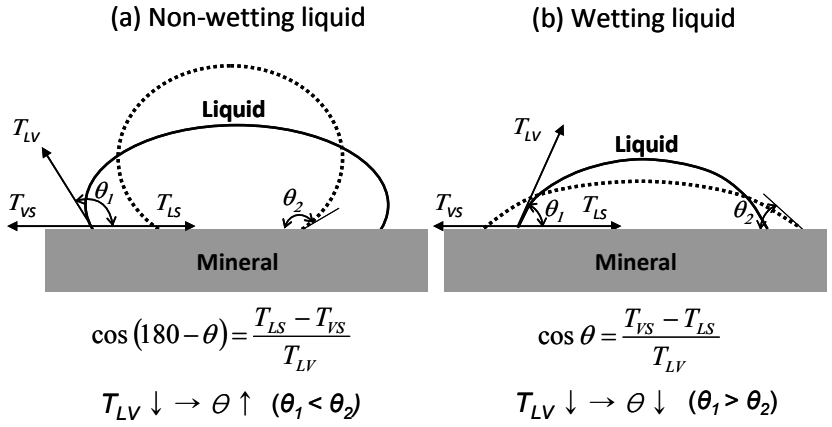

Figure 4.4. The effect of changes in interfacial tension on contact angle. The dotted line shows the droplet geometry when T_{LV} decreases.

4.3.2 Implications

Micromodel images. Phenomena described above can be seen in Figure 4.5. The images of water, ice, and hydrate in micromodels are shown. Water is a wetting phase in micromodels, while the images of ice and hydrate confirm non-wetting phase. THF hydrate visualized by X-ray tomography also shows that THF hydrate is not wetting phase in the pack of glass beads [Kerkar et al., 2009].

Hydrophilic and hydrophobic surfaces. Usually, mineral surfaces in sediments and rocks are hydrophilic and water-wet conditions prevail. The oil-wet condition may result when a water-repellent agent (for example, silicone) is absorbed onto the mineral surface. Chemisorption of organic matter on the mineral surface may also create a hydrophobic surface. However, since mineral surfaces are hydrophilic in nature, the oil-wet condition can be considered a temporary condition. Thus, given enough time, organic fluids tend to be displaced by water. In short-time processes, such as enhanced oil recovery, wettability has a significant effect on multiphase flow [Morrow, 1990].

Displacement – Mixed fluid condition. Fluid invasion, under mixed fluid conditions, is controlled by capillary F_c, viscous drag F_d and weight/bouyancy W or F_b forces. These forces can be combined into dimensionless numbers [Pennel et al., 1996; Lenormand et al., 1988 – Note: the defending and invading fluid viscosities are μ_{def} and μ_{inv}]:

$$N_C = \frac{F_d}{F_c} = \frac{3\pi d\mu_{inv} v}{\pi d T_s \cos\theta} = \frac{3\mu_{inv} v}{T_s \cos\theta} \tag{4.5}$$

$$N_M = \frac{\mu_{inv}}{\mu_{def}} \tag{4.6}$$

$$N_G = \frac{F_d}{W} = \frac{3\pi d\mu_{inv} v}{\pi G_s \gamma_w d^3/6} = \frac{18\mu_{inv} v}{G_s \gamma_w d^2} \tag{4.7}$$

$$N_B = \frac{F_b}{F_c} = \frac{\Delta\gamma\, \pi d^3/6}{\pi d T_s \cos\theta} = \frac{\Delta\gamma\, d^2}{6 T_s \cos\theta} \tag{4.8}$$

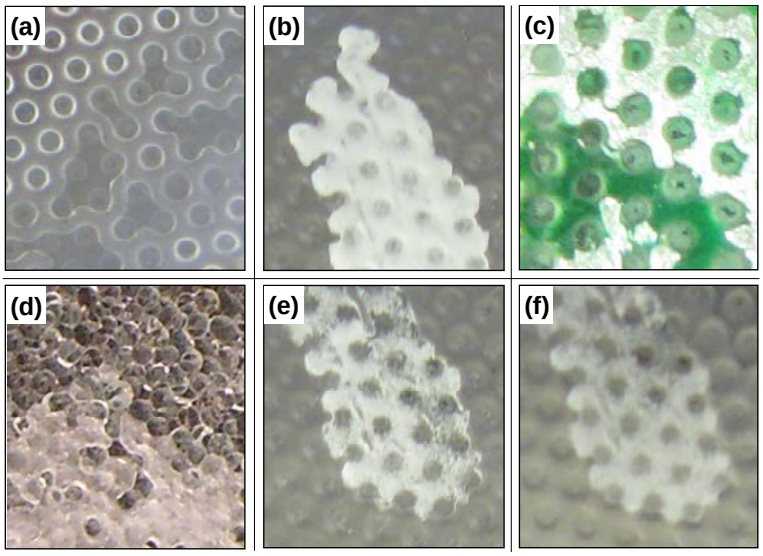

Figure 4.5. Micromodel images. (a) CH_4 gas-water. (b) CH_4 gas-ice. (c) Water-CH_4 hydrate. (d) CO_2 gas-CO_2 hydrate. (e) CH_4 gas-CH_4 hydrate. (f) liquid CO_2-CH_4 hydrate 30 minutes after CH_4 hydrate is submerged into liquid CO_2. Etched micromodel: (a), (b), (c), (e), and (f). Grain-based micromodel: (d).

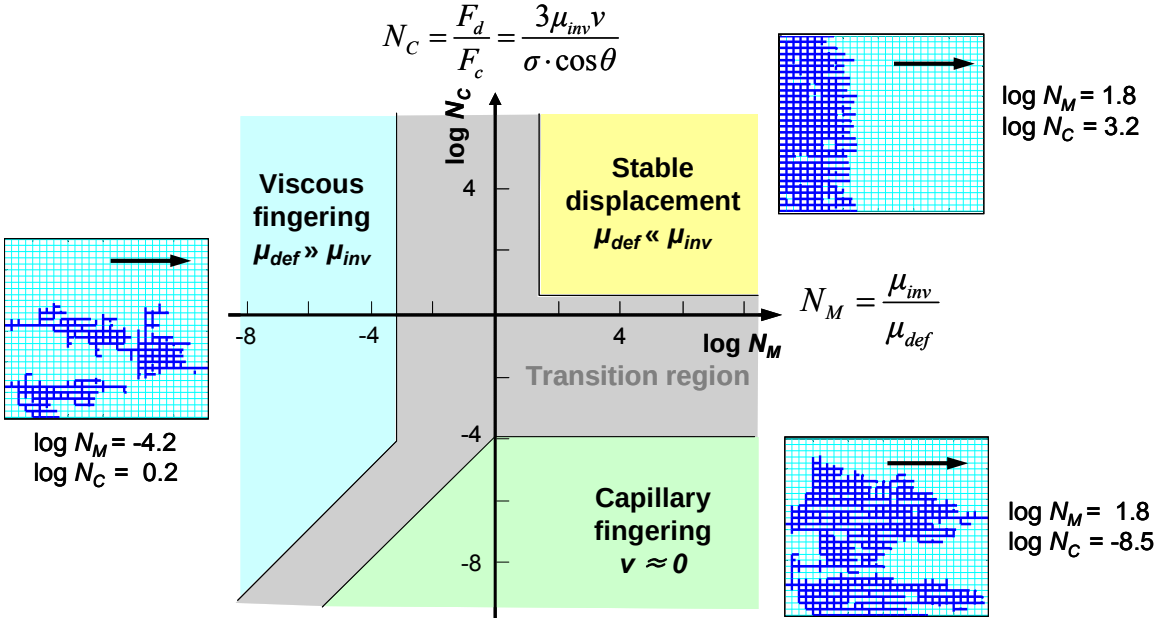

Figure 4.6. Space for viscous fingering, capillary fingering, and stable displacement in terms of dimensionless ratios N_M and N_C – refer to text (modified from Lenormand et al. 1988; tube network model simulations done by S. Dai, Georgia Tech).

Invasion conditions and emergent phenomena can be identified in the dimensionless space of these π-ratios. Figure 4.6 shows a 2D-slice of this space. Implications relevant to hydrate-bearing sediments are identified next:

- Capillary water invasion of a gas saturated sediment: the wetting fluid advances, preferentially along the smallest connected pores.
- Oil forced to invade a water-saturated sediment: during slow invasion, the non-wetting high viscosity fluid must overcome capillary resistance, and invades the largest pores first.
- Gas storage in a water-saturated sediment and gas production during hydrate dissociation: the invasion by a non-wetting low viscosity fluid may lead to fingering.
- Liquid CO_2 is injected into a water-saturated sediment: the non-wetting liquid CO_2 has a viscosity that is two orders of magnitude smaller than that of water [Jung et al., 2010], and viscous fingering will tend to develop (high N_c and low N_m in Figure 4.6 – see Qi et al. 2009).
- Ice and hydrate growth: it resembles the slow invasion of a high viscosity non-wetting phase.

4.4 Hydrate phase boundary

Hydrate formation and dissociation occurs at characteristic *P-T* conditions. However, the phase boundary is affected by the conditions that alter molecular motion, such as interaction with mineral surfaces and the presence of other ions and molecules, including salts and mixed gases.

4.4.1 Modifications of the phase boundary

The effect of pore size. Water activity decreases near a mineral surface due to the affinity of water to the mineral. Therefore, gas hydrates experience dissociation temperature

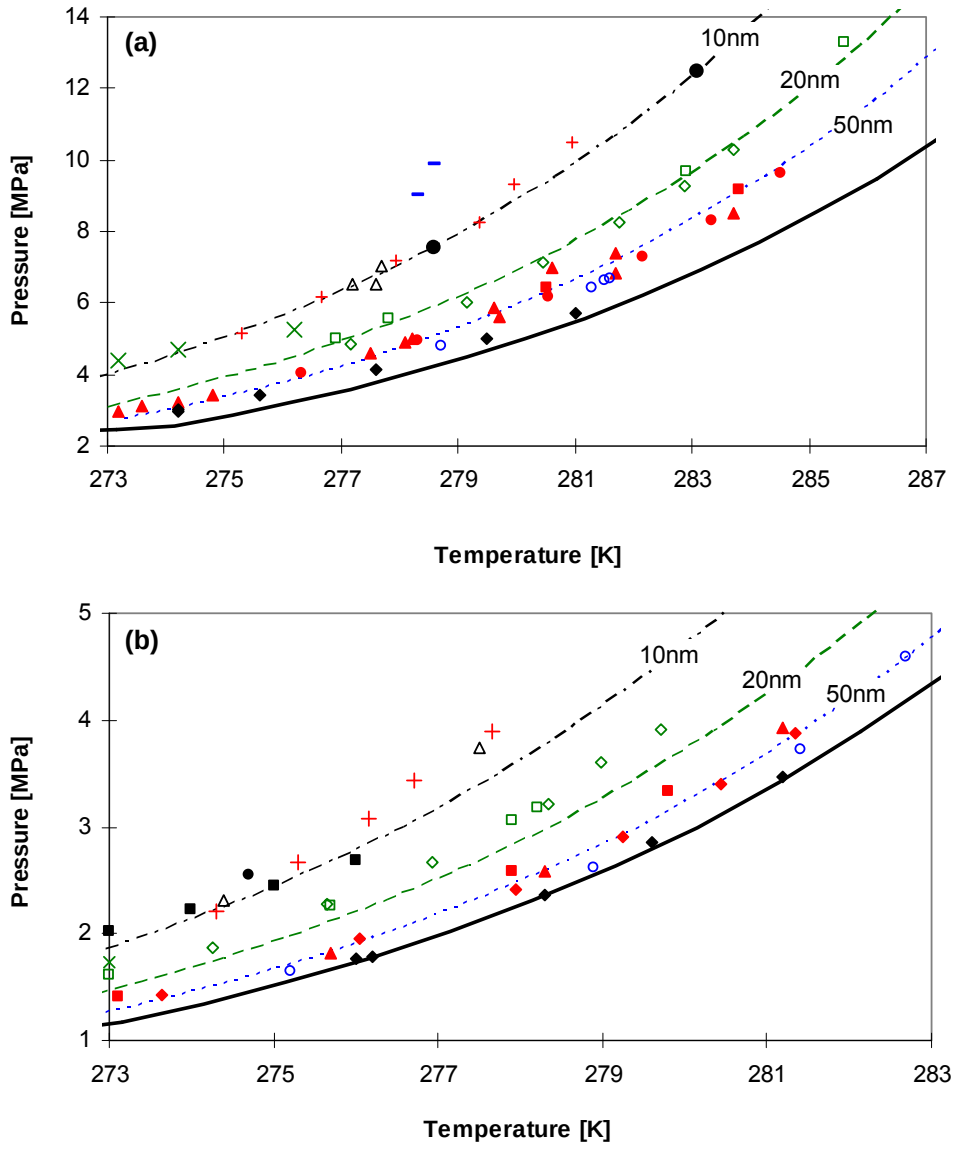

Figure 4.7. Hydrate stability in small pores. (a) CH_4 hydrate stability. Theoretical stability boundary of CH_4 hydrates in (black continuous line) bulk phase and (blue dotted line) 50nm, (green broken line) 20nm, (black chain line) 10nm pores. Experimentally obtained stability condition of CH_4 hydrate in (♦) 102.6nm [Uchida et al., 2002], (○) 49.5nm [Uchida et al., 2002], (▲) 30.9nm [Uchida et al., 2002], (●) 30nm [Set et al., 2002], (■) 30.6nm [Anderson et al., 2003], (×) 14nm [Handa and Stupin, 1992], (◊) 15nm [Set et al., 2002], (□) 15.8nm [Anderson et al., 2003], (Δ) 11.9nm [Uchida et al., 2002], (●) 9.2nm [Anderson et al., 2003], (-) 6nm [Uchida et al., 2002], (–) 6nm [Smith et al., 2002], and (+) 6nm [Seo et al., 2002] pores. Parameters for Gibbs-Thompson equation are T_s=32mN/m, m_h=119.5g/mol, cosθ=1, ρ_{CH4}=914kg/m^3, and L_f=53.2kJ/mol [Anderson et al., 2003]. (b) CO_2 hydrate stability in small pores. Theoretical stability boundary of CO_2 hydrates in (black continuous line) bulk phase and (blue dotted line) 50nm, (green broken line) 20nm, (black chain line) 10nm pores. Experimentally obtained stability condition of CO_2 hydrate

in (♦) 102.6nm [Uchida et al., 2002], (○) 49.5nm [Uchida et al., 2002], (▲) 30.9nm [Uchida et al., 2002], (●) 30nm [Set et al., 2002], (■) 30.6nm [Anderson et al., 2003], (×) 15nm [Smith et al., 2002], (◊) 15nm [Set et al., 2002], (□) 15.8nm [Anderson et al., 2003], (Δ) 11.9nm [Uchida et al., 2002], (■) 10nm [Smith et al., 2002], (●) 9.2nm [Anderson et al., 2003], and (+) 6nm [Seo et al., 2002] pores. Parameters for Gibbs-Thompson equation are T_s=30mN/m, m_h=147.5g/mol, cosθ=1, ρ_{CO2}=1065kg/m^3, and L_f=65.2kJ/mol [Anderson et al., 2003].

depression in small pores. The dissociation temperature depression is captured by the Gibbs-Thomson equation [Anderson et al., 2003; Kwon et al., 2008].

$$\Delta T_{dep} = -\frac{2}{d}\left(\frac{\gamma_{hw} m_h \cos\theta}{\rho_{h0} L_H}\right) T_{bulk} \qquad \text{Cylindrical hydrate shape} \qquad (4.9)$$

$$\Delta T_{dep} = -\frac{4}{d}\left(\frac{\gamma_{hw} m_h \cos\theta}{\rho_{h0} L_H}\right) T_{bulk} \qquad \text{Spherical hydrate shape} \qquad (4.10)$$

where γ_{hw} is the surface tension between hydrate and water, m_h is the molecular weight of gas hydrate [g/mol], ρ_h is the mass density of hydrate [kg/m^3], and L_H is the heat of hydrate dissociation [kJ/kg] (Refer Table 4.3 for typical values). Experimental measurements of the dissociation temperature depression are compiled in Figure 4.7 for CH_4 and CO_2 hydrate. Trends predicted by the Gibbs-Thomson equation are superimposed on the figure. We can conclude that the pore size effect vanishes when pores are larger than ~0.1μm.

The effect of salinity. Hydrate ions from dissolved salt in water interacts with the water dipoles through a Coulombic bond that is stronger than the hydrogen bond or the van der Waals force. The strong bonds between water and salt ions hinder hydrate formation by inducing a clustering of water molecules near the ions. Therefore, substantial sub-cooling is needed to cause hydrate formation [Sloan and Koh, 2008].

The decreased hydrate equilibrium temperature T_S^H [K] in salty water from the equilibrium temperature T_P^H [K] in pure water is related to the freezing point depression of salt water from 273.15K to T_S^I [K], the latent heat of transformation of ice L_I and hydrate L_H, and the hydration number χ [Dickens and Quinby-Hunt, 1997].

$$\left(\frac{1}{T_P^H}-\frac{1}{T_S^H}\right)=\frac{\chi L_I}{L_H}\left(\frac{1}{273.15}-\frac{1}{T_S^I}\right) \tag{4.11}$$

The top figure in Figure 4.8 shows the phase boundary shift in salty water. Figure 4.8 shows experimental data obtained with a micromodel. Liquid CO_2 is injected into the water-saturated micromodel outside of the hydrate stability field (Figure 4.8a) to maximize carbon dioxide solubility in water (~1.53mol/kg at P=4.5MPa and T=11.5°C). Note that much of the water diffuses into the liquid CO_2 (Figure 4.8b). Finally, substantial cooling triggers CO_2 hydrate formation (Figure 4.8c). Brine is then injected into the micromodel (6.3% NaCl). Figure 4.8d~f shows that the hydrate mass eventually dissociates in the presence of the brine.

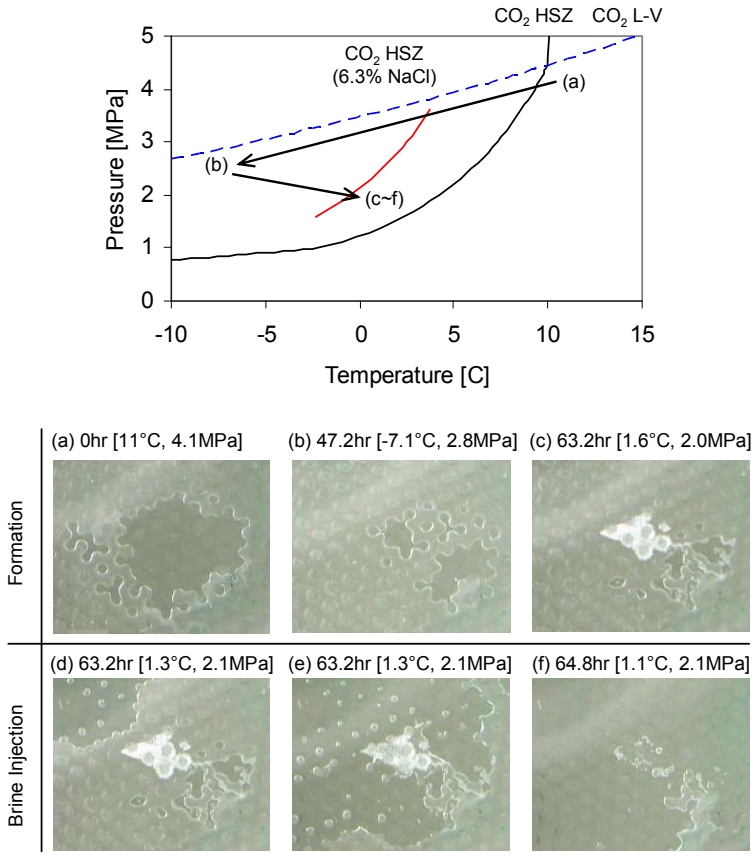

Figure 4.8. CO_2 hydrate formation, followed by dissociation by brine injection. (a) Water in gaseous CO_2. (b) Water in gaseous CO_2 after CO_2 flooding. (c) CO_2 hydrates in gaseous CO_2. (d) and (e) Brine injection. (f) CO_2 hydrates dissociation after brine injection.

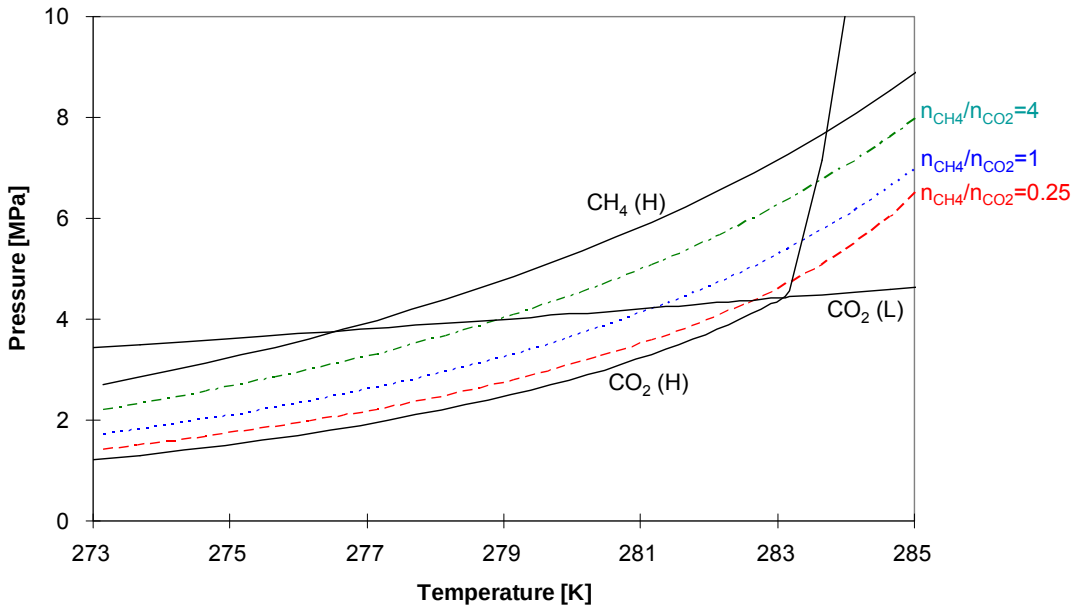

Figure 4.9. Hydrate phase boundary – different methane and carbon dioxide gas mixtures. Molar fractions of methane n_{CH4} and carbon dioxide n_{CO2}: (red broken line) $n_{CH4}/n_{CO2}=0.25$, (blue dotted line) $n_{CH4}/n_{CO2}=1$, (green chain line) $n_{CH4}/n_{CO2}=4$.

The effect of mixed gases. The phase boundary for methane mixed with carbon dioxide hydrate is calculated using HydraFLASH [from HYDRAFACT]; the results are shown in Figure 4.9. This algorithm combines the solid solution theory [van der Waals and Platteeuw, 1959], and a spherical molecule model to calculate of the potential function for compounds forming the hydrate phase [Kihara, 1953], in a general multi-phase routine [Cole and Goodwin, 1990] to calculate the hydrate composition at specified temperature, pressure, and system composition [user guide HydraFLASH v2.2].

4.4.2 Implications

Pore size, salinity, and mixed-gas driven changes in hydrate stability field have many potential implications: Pore size decreases with increased sediment depth; therefore, the degree of freezing point depression can become substantial in clayey sediments.

- Pore size-dependent shifts in the phase boundary for montmorillonite, illite, and kaolinite are shown in Dai et al. (2011).
- In-situ mixed gas conditions can explain apparent inconsistencies in theoretical calculations of Bottom Simulating Reflector.
- Increased salt concentration in trapped water during hydrate formation in excess gas systems results in coexisting gas, water (brine), and hydrate.

4.5 Thermal properties

Hydrate dissociation is a pronounced endothermic process. Therefore, thermal properties of hydrate-bearing sediments are critical for gas production.

4.5.1 Specific heat and latent heat of transformation

Thermal properties of water, ice, mineral, methane and carbon dioxide gas, and methane and carbon dioxide hydrate are compiled in Table 4.3. Note that the energy required to dissociate methane hydrate ($CH_4 6H_2O$) ~440kJ/kg is higher than the energy required to melt ice ~335kJ/kg (Table 4.3). It is enlightening to compare the energy needed to heat water $\rho_w c_w \Delta T_w$ to the energy needed to melt ice $\rho_i L_i$ or dissociate methane hydrate $\rho_h L_h$, where the water density is ρ_w=1000kg/m^3, the methane hydrate density is ρ_h=914kg/m^3, the latent heat of ice melting is L_i=335kJ/kg, the latent heat of methane hydrate dissociation is L_h=440kJ/kg, and the specific heat of water is c_w=4.2kJ/(kg·°C) (refer to Table 4.3).

$$\Delta T_{iw} = \beta_i = \frac{\rho_i L_i}{\rho_w c_w} = 73.1°C \tag{4.12}$$

$$\Delta T_{hw} = \beta_h = \frac{\rho_h L_h}{\rho_w c_w} = 95.8°C \tag{4.13}$$

Table 4.3. Physical properties of water, ice, mineral, methane, carbon dioxide, and methane and carbon dioxide hydrate - Specific heat, heat of transformation, and density.

	Specific heat [kJ/(kg·°C)]	Heat of transformation [kJ/kg]	Density [kg/m^3]
Water	4.218 (273K)[a] 4.192 (283K) [a] 4.2174 (273K)[c]	For water mass, 334.2 (273.2K)[b] 336 (273.1K)[c]	999.9 (273K)[a] 999.7 (283K)[a]
Ice	2.014 (260K)[b] 1.957 (260K)[c] 2.097 (270K)[b] 2.052 (270K)[c] 2.097 (273K)[d]	-	917 (273K)[e]
Quartz	0.73 (273K)[d] 0.71 (273K)[f] 0.8 (286~373K)[f]	-	2650[e] 2620[f]
CH_4 (g)	2.26 (298K, 0.1MPa)[f] 2.259 (280K, 1MPa)[g] 3.813 (280K+, 20MPa)[g]	2290 (Heat of combustion)[f]	7.04 (280K, 1MPa)[g] 177.56 (280K, 20MPa)[g]
CO_2 (g)	0.819 (275K)[f] 2.47 (273K)[f]	-	983[f] (273K, 3.4MPa)
CO_2 (l)	2.5694 (274K 3.5642MPa)[h] 2.8141 (280K, 4.1607MPa)[h] 2.2798 (280K, 10MPa) [h]]	-	922.3 (274K 3.5642MPa)[h] 883.58 (280K, 4.1607MPa)[h] 938.22 (280K, 10MPa)[h]
CH_4 hydrate	2.003 (260K for $CH_4 \cdot 6H_2O$)[i] 2.077 (270K for $CH_4 \cdot 6H_2O$)[i] 0.0061 ·(T-273) + 2.16 (274~290K, 31.5MPa)[j] 0.0033 ·(T-273) + 2.14 (287.4K, 31.5~102MPa)[j]	For $CH_4 \cdot nH_2O$ 437.1[i] 430.3 (283.15K, n=5.98)[k] 470.4 (278.15K, n=5.97)[k] 429.8[l] 434.4 (273.65K, n=6.38)[m]	929 (263K)[j]
CO_2 hydrate	No data found	For $CO_2 \cdot nH_2O$ 374.5 (273.65K, n=7.23)[m] 374.4 (281K, n=6.16)[n] 343.0 (279K, n=6.16) [n]	1065[o] 1054[p]

a-Weast (1987), b-Handa et al. (1984), c-Leaist et al. (1982), d-Kaye and Laby, d-National Physical Laboratory, e-Dvorkin et al. (2000), f-Engineering ToolBox, g-Sychev et al. (1987), h-Span and Wagner (1996), i-Handa (1986), j-Waite et al. (2007), k-Lievois et al. (1990), l-Rueff et al. (1988), m-Kang and Lee (2001), n-Nagayev et al. (1979), o-Anderson et al. (2003), p-Uchida et al. (2002).

Therefore, the energy required to melt ice is the same as the energy required to heat water by ΔT_{iw}=73.1°C, while the energy required to dissociate hydrate is equivalent to the energy required to heat water by ΔT_{hw}= 95.8°C.

4.5.2 Implications on gas production

Let's assume a hydrate-bearing sediment dissociating under adiabatic conditions so that the heat for hydrate dissociation is supplied by the sensible heat of the hydrate-bearing sediment. The initial temperature T_i and pressure P_i conditions are inside of the hydrate stability field (Figure 4.10a). As pressure P_i decreases across the stability boundary P_f, the hydrate dissociates and the temperature of the hydrate-bearing sediment decreases to a final temperature T_f due to endothermic nature of hydrate dissociation.

The sensible heat available in the volume V_T of the hydrate-bearing sediment E_{HBS} is expressed as a function of the heat available in the mineral, water, and hydrate and the energy produced by ice formation.

$$\begin{aligned} E_{HBS} = {} & V_T\left[(1-n)\rho_m c_m\left(T_i - T_f\right) + n(1-S_h)\rho_w c_w\left(T_i - T_f\right) + nS_h\rho_h c_h\left(T_i - T_t\right)\right] \\ & + V_T\left[0.8nS_h\rho_w c_w\left(T_t - T_f\right) + nS_h\rho_g c_g\left(T_t - T_f\right)\right] \\ & + V_T\left[n(1-S_h) + 0.8nS_h\right]\rho_w L_i FR_{wi} \end{aligned} \tag{4.14}$$

where the densities of the mineral, water, hydrate, and gas are ρ_m, ρ_w, ρ_h, and ρ_g=16ρ_h/119.5 [kg/m^3] and their specific heats are c_m, c_w, c_h, and c_g [kJ/kg]. The term FR_{wi} represents the fraction of the total water (the summation of the initial water and the water produced from hydrate dissociation) that is converted into ice.

On the other hand, the energy needed to dissociate hydrate E_{DIS} is a function of the total sediment volume V_T, porosity n, hydrate saturation S_h, hydrate density ρ_h, and the latent heat of hydrate dissociation L_h,

$$E_{DIS} = V_T nS_h\rho_h L_h \tag{4.15}$$

When the final temperature of the sediment is assumed to be T_f=0°C and there is no ice formation, the maximum initial hydrate saturation S_h, which does not induce ice formation during hydrate dissociation, is derived by equating Equation 4.14 to Equation 4.15 disregarding the heat of ice formation (third term in Equation 4.14).

$$S_h = \frac{(1-n)\alpha_m(T_i - T_f) + n(T_i - T_f)}{n\beta_h + n(T_i - T_f) - n\alpha_h(T_i - T_t) - 0.8n(T_t - T_f) - n\alpha_g(T_t - T_f)} \tag{4.16}$$

where the density times the specific heat of each species $\rho_i c_i$ is normalized by the value for water $\rho_w c_w$, so that $\alpha_m = \rho_m c_m / \rho_w c_w$, $\alpha_h = \rho_h c_h / \rho_w c_w$, and $\alpha_g = \rho_g c_g / \rho_w c_w$; the same normalization is enforced for the product of the hydrate density and the latent heat of dissociation $\beta_h = \rho_h L_h / \rho_w c_w$ (refer to discussion above).

For example, when initial temperatures of hydrate-bearing sediments T_i=5, 10, 15, and 20°C, hydrate equilibrium temperature T_t=2.5°C (when P_{eq}=3MPa), and final temperature T_f is assumed to be T_f=0°C, the maximum hydrate saturation which does not induce ice formation during dissociation is S_h=0.09, 0.17, 0.25, and 0.32 for each initial temperature conditions (other parameters in Table 4.3), that is, hydrate can fully dissociate with the heat available in the hydrate-bearing sediments without forming ice when the initial hydrate saturation is less than 9% for T_i=5°C, 17% for T_i=10°C, 25% for T_i=15°C and 32% for T_i=20°C.

The fraction of ice formed from hydrate dissociation FR_{wi} when S_h>0.09~0.32 is obtained by combining Equations 4.14 and 4.15.

$$FR_{wi} = \frac{nS_h\beta_h - (1-n)\alpha_m(T_i - T_f) - n(1-S_h)(T_i - T_f) - nS_h\alpha_h(T_i - T_t) - 0.8nS_h(T_t - T_f) - nS_h\alpha_g(T_t - T_f)}{[n(1-S_h) + 0.8nS_h]\beta_h} \tag{4.17}$$

As the initial hydrate saturation S_h increases, some of the water is converted into ice in order to provide heat for hydrate dissociation. Figure 4.10b shows the fraction of the total water converted into ice by hydrate dissociation at various saturations. When the hydrate saturation is S_h≈0.78~0.94 for initial temperature T_i=5~20°C, all of the water needs to be converted into ice to provide heat for hydrate dissociation.

Given the large amount of heat needed for hydrate dissociation, extra heat should be transported from neighboring regions in high hydrate saturation deposits considered for gas production. In fact, numerical simulations show that the gas production rate and cumulative gas amount are higher for deeper and warmer hydrate-bearing reservoirs than

for shallower and cooler sediments when a constant depressurization pressure is applied to the wellbore [Anderson et al., 2011; Moridis et al., 2011].

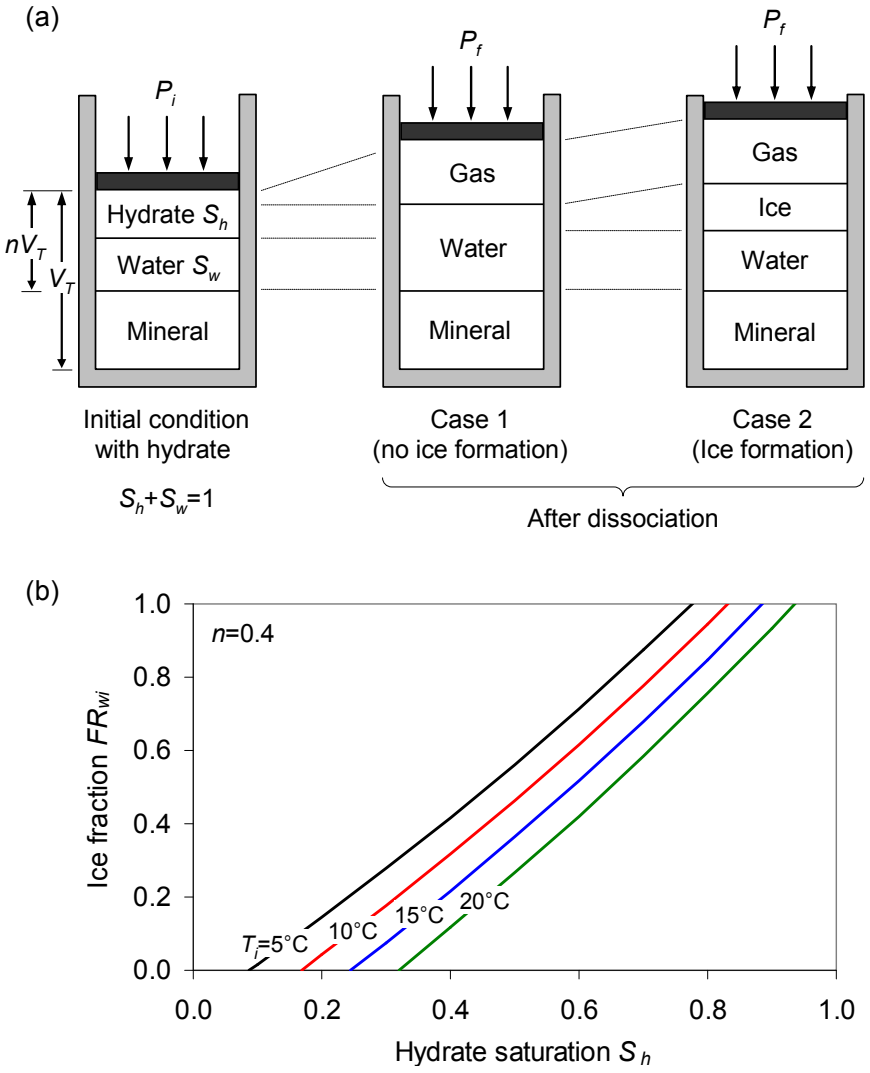

Figure 4.10. Hydrate dissociation and subsequent possible ice formation. (a) Hydrate bearing sediment with initial hydrate saturation S_h. Under adiabatic conditions, the energy needed to dissociate hydrate can be supplied by the medium's latent heat (case 1); additional heat may be gained from exothermic ice formation (case 2). (b) Consider hydrate bearing sediments with porosity n=0.4 at initial temperatures T_i=5, 10, 15, and 20°C depressurized to P_{eq}=3MPa so that the hydrate equilibrium temperature is T_{eq}=2.5°C. Ice does not form if initial hydrate saturation is S_h=0.09, 0.17, 0.25, and 0.32 for each initial temperature conditions. As the initial hydrate saturation increases, the amount of ice formed due to hydrate dissociation also increases. Ice fraction FR_{wi} is the portion of water (initial water and water from hydrate dissociation) converted into ice. Refer the Table 4.3 for specific heat of mineral, water, gas, and hydrate and for latent heat of hydrate dissociation and ice formation.

4.6 Conclusions

The complex behavior of hydrate formation and dissociation requires a thorough understanding of physical properties at the pore-scale for the determination of optimal gas production methods.

The solubility of hydrate-forming gas in water and the mutual solubility of these gases and water affect hydrate formation and dissociation. Salt in water reduces gas solubility. Gas solubility in water in the presence of hydrate shows an opposite temperature dependence compared to the gas solubility outside of the hydrate stability field. The solubility change due to the presence of hydrate causes early transients in hydrate formation and dissolution, and can justify some of the hydrate lenses observed in fine-grained sediments. Liquid CO_2 injection into the hydrate-bearing sediment can dry the sediment or dissolve the hydrate due to the solubility of water and methane in liquid CO_2.

Interfacial tension is pressure-dependent. The change in interfacial tension brings about a change in contact angle. Interfacial tension, contact angle, viscosity and flow rate determine the displacement pattern of the invading and defending fluids in the sediment under mixed fluid conditions. Liquid CO_2 injection into a water-saturated medium may result in viscous fingering.

Decreasing pore size with increased sediment depth and dissolved salts shift the phase boundary to higher pressure and lower temperature conditions. Hydrates of a methane and carbon dioxide gas mixture have an intermediate phase boundary between pure methane and pure carbon dioxide hydrate phase boundaries. In-situ mixed gas condition causes a shift in the depth of the bottom of the hydrate stability zone.

Hydrate dissociation requires a substantial amount of heat that is equivalent to the energy needed to warm the same volume of water by as much as $\Delta T_w \approx 96°C$. The heat needed for endothermic hydrate dissociation may be contributed by the latent heat in the sediment when the hydrate concentration is low (S_h<9~32% for T_i=5~20°C). Higher initial hydrate concentration may be compensated by exothermic ice formation, or heat transport

from neighboring regions in the sediment. Hydrate dissociation when S_h≈0.78~0.94 would require all water to turn into ice (if T_i=5~20°C). Clearly, the thermal conductivity and in-situ temperature of the hydrate-bearing sediment will determine the attainable gas production rates.

CHAPTER 5

RECOVERABLE GAS FROM HYDRATE-BEARING SEDIMENTS: PORE-NETWORK MODEL SIMULATION AND MACRO-SCALE ANALYSES

5.1 Introduction

Hydrate formation is controlled by pressure, temperature, fluid chemistry and the availability of hydrate-forming gases. In sediments, hydrate distribution and saturation are also determined by the sediment pore size distribution, connectivity, and spatial variability [Waite et al., 2009].

Pressure-temperature *P-T* conditions for several hydrate bearing reservoirs are plotted in Figure 5.1. In each case, the potential hydrate bearing sediment is bounded by the reported seafloor *P-T* conditions on the left and the methane hydrate phase boundary on the right (shown for 3.5% salinity). The local geothermal gradient determines the slope of dotted lines that represent each formation. The superimposed thick lines show hydrate bearing layers inferred from pore fluid chemistry, electrical resistivity logs, gamma ray logs, and wave velocity data. These results confirm that hydrates are not necessarily found throughout the gas hydrate stability zone, and sometimes the presence of hydrates is restricted to specific layers (e.g., Mt. Elbert and Gulf of Mexico).

We note that hydrate saturation S_h and grain size distribution vary widely among hydrate bearing reservoirs or even within a given borehole: gas hydrate bearing sands in the Nankai Trough and Gulf of Mexico may reach up to 80% saturation whereas gas hydrates in fine grained sediments often contain low hydrate saturation [Uchida et al., 2004; Boswell et al., 2009; Tréhu et al., 2004]. The mean grain size of hydrate bearing sediments ranges from 2-to-5μm for Blake Ridge and Hydrate Ridge to 0.1-to-0.3mm for the Nankai Trough and Mallik [Soga et al., 2007]. Hydrates can be found filling pores

typically in coarse grained sediments, or in veins and lenses typically in fine grained sediments [Waite et al., 2009].

Several numerical simulators have been developed to analyze gas production from hydrate bearing sediments [Wilder et al., 2008; Anderson et al., 2011; Hong and Pooladi-Darvish, 2003; Uddin et al., 2008; Nazridoust and Ahmadi, 2007; Gamwo and Liu, 2010; Moridis et al., 2007; Moridis and Sloan, 2007; Moridis et al., 2011; Kurihara et al., 2009]. Most simulators consider mixed fluid conditions, adopt van Genuchten-type relative permeability models, and capture the thermodynamics of hydrate dissociation to estimate gas and water production rates. However, it is difficult to extract prevailing trends and to identify governing process from these simulations given their complexity and the large number of both physical and fitting parameters involved. In addition, the relative permeability models that are used were derived for an invading gas phase that percolates from the boundary as in a drying unsaturated soil: however, hydrate dissociation implies the formation of a gas phase within the medium. We also note that back-analyzed field cases are based on cumulative recovered gas at the boundary, and complete dissociation is not necessarily attained within the medium [Anderson et al., 2011; Moridis et al., 2011; Moridis et al., 2007; Konno et al., 2010; Hong and Pooladi-Darvish, 2003]. Hence, recoverable gas cannot be properly determined in these cases.

In this manuscript, we use pore network models defined with a minimal set of physically meaningful pore-scale parameters to elucidate gas recovery and water production as a function of the initial hydrate saturation, pore size distribution, and *P-T* conditions. First, we compute fluid volume expansion during hydrate dissociation and gas recovery as a function of in-situ *P-T* conditions and anticipated *P-T* changes. Then, we evaluate the effect of fluid expansion, initial hydrate saturation and pore size distribution on recoverable gas and on the evolution of gas saturation during hydrate dissociation and subsequent depressurization. Results are applicable to gas production by either

depressurization or thermal stimulation when production rates prevent secondary hydrate or ice formation.

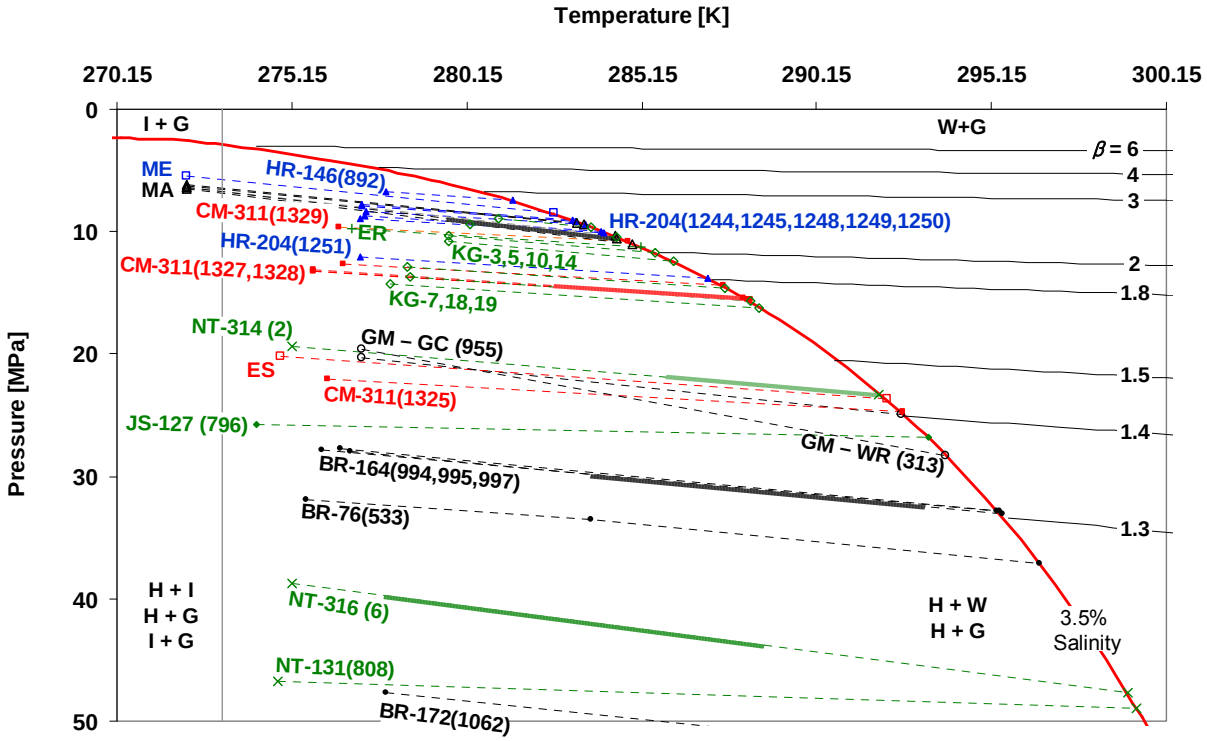

Figure 5.1. Pressure and temperature condition for worldwide hydrate reservoirs (to the left of the phase boundary). Lines of equal hydrate-to-fluid expansion factor $\beta=(V_g+V_w)/V_h$ are shown to the right (see Section 5.2 for the derivation of the expansion factor β). Plotted cases correspond to: (•) Blake Ridge BR [DSDP 76 (Site 533), ODP 164 (Site 994, 995, and 997), ODP 172 (Site 1062)], (×) Nankai Trough NT [ODP 131 (Site 808) IODP 314], (•) Japan Sea JS [ODP 127 (Site 796)], (■) Northern Cascadia Margin CM [ODP 146 (Site 889 and 890), IODP 311 (Site 1325, 1327, 1328, and 1329)], (□) East Sea (Korea) ES, (○) Gulf of Mexico GM [Green Canyon 955H, Walker Ridge 313], (◊) Krishna-Godavari Basin (India) KG [NGHP 01 (3,5,7,10,14,18, and 19)], (▲) Hydrate Ridge HR [ODP 146 (Site 892), ODP 204 (Site 1244, 1245, 1248, 1249, 1250, and 1251)], (+) Eel River Basin (California) ER [ODP 167 (Site 1019)], (Δ) Mallik MA [2~5L-38], and (□) Mt. Elbert ME [ME-01] (Hydrate zone only below permafrost is considered here). The methane hydrate phase transformation boundary is shown for 3.5% salinity water [Sloan and Koh, 2008]. The modified Peng-Robinson equation of state [Stryjek and Vera, 1986] is used to calculate fluid expansion. We assume no solubility of methane gas in water, constant mass density for water, and no capillary effects, i.e., coarse grains.

5.2 Preliminary analyses – Fluid expansion

Hydrates dissociate into methane-saturated water and water-saturated methane gas. There is a pronounced pressure dependent fluid expansion across the phase boundary during hydrate dissociation, followed by additional gas expansion due to depressurization.

Let's derive an expression for fluid expansion as a function of reservoir *P-T* conditions and pore throat size. Since the solubility of methane in water is very low, it can be neglected for first order estimation of fluid expansion. We define the fluid expansion factor associated with hydrate dissociation β as the ratio of the combined gas and water volumes (V_g and V_w respectively) to the initial volume of hydrate V_h, so that $\beta=(V_g+V_w)/V_h$. The dissociated methane volume V_g is a function of *P-T* conditions; we use the modified Peng-Robinson equation of state (PRSV) to relate V_g to P_g and T_g [Stryjek and Vera, 1986]:

$$P_g = \frac{RT_g}{V_g - b} - \frac{a}{V_g\left(V_g + b\right) + b\left(V_g - b\right)} \qquad \text{Modified Peng-Robinson (per mole of methane)} \qquad (5.1)$$

The values of a and b parameters for methane gas and the universal gas constant R are summarized in Table 5.1.

Gas and water are at different pressures in a porous medium. The capillary pressure P_c is the pressure difference between gas P_g and water P_w pressures. It is a function of surface tension Γ, contact angle θ, and pore throat radius R_{th},

$$P_c = P_g - P_w = \frac{2\,\Gamma\cos(\theta)}{R_{th}} \qquad \text{Capillary pressure} \qquad (5.2)$$

The volume of water V_w that results from hydrate dissociation is related to the initial volume of hydrate V_h as $V_w/V_h=(18\chi)/(16+18\chi)\cdot\rho_h/\rho_w$ where χ is the hydration number; for a theoretical value of $\chi=5.75$, then $V_w=0.79V_h$. The molar concentration of methane in hydrate is λV_h where λ is the amount of methane per unit volume of hydrate ($\lambda=\rho_h/(16+18\chi)$ and equals $\lambda=\rho_h/(119.5$ g/mol) [mol/cm^3] when $\chi=5.75$). Combining these expressions, the fluid expansion factor β can be written as

$$\beta = \frac{V_g + V_w}{V_h} = \frac{V_g}{V_h} + \frac{V_w}{V_h} = f\left(P_w, P_c, T_g\right) + \frac{18\chi}{16+18\chi}\frac{\rho_h}{\rho_w} \quad \text{Fluid expansion factor} \qquad (5.3)$$

The full equation for β is used in subsequent computations but it is not included in the text given its complexity (The volume of gas V_g is obtained by solving cubic equation - Equation 5.1).

A simple expression for the fluid expansion factor β can be obtained using the "modified ideal gas law"

$$\begin{aligned}\beta &= \frac{V_g + V_w}{V_h} \\ &= \frac{z\lambda RT_g}{P_g} + \frac{18\chi}{16+18\chi}\frac{\rho_h}{\rho_w} \\ &= \frac{z\lambda RT_g}{P_w + \frac{2\Gamma}{R_{th}}\cos\theta} + \frac{18\chi}{16+18\chi}\frac{\rho_h}{\rho_w}\end{aligned} \quad \text{Approximate fluid expansion factor} \qquad (5.4)$$

where λ is the amount of methane per unit volume of hydrate and z is a "compression factor" added to the ideal gas law to fit the PRSV equation within the P-T range of interest. For z=0.7, the expansion factor calculated with Equation 5.4 closely matches the factor computed with the modified Peng-Robison equation of state (Equation 5.3). This simple and explicit close-form expression for the fluid expansion factor β highlights the interplay between pressure, temperature, surface tension, and pore throat radius.

Table 5.1. Parameters used in the equation of state [Stryjek and Vera, 1986].

Parameters	Symbols	Values
Universal gas constant	R	83.15 [bar·cm^3 / mol·K]
Attraction term parameter	a	$(0.457235R^2T_c^2/P_c)\alpha$
Repulsion term parameter	b	$0.077796RT_c/P_c$
	α	$[1+\kappa(1-T_r^{0.5})]^2$
Adjustable parameter	κ	$\kappa_0+\kappa_1(1+T_r^{0.5})(0.7-T_r)$
Adjustable parameter	κ_0	$0.378893+1.4897153\omega -0.17131848\omega^2+0.0196544\omega^3$
Adjustable parameter	κ_1	-0.00159 for methane
Acentric factor	ω	0.01045 for methane
Critical pressure	P_c	4.595MPa for methane
Critical temperature	T_c	190.555K for methane
Reduced temperature	T_r	T/T_c

Lines of equal hydrate-to-fluid expansion factor β are plotted in Figure 5.1 to the right of the phase boundary. There is a significant volume increase across the phase boundary: an initial hydrate volume V_0 immediately inside the stability field converts into βV_0 immediately outside the stability field. For example, the initial expansion is β~1.3 near the bottom of the gas hydrate stability zone in Blake Ridge [ODP 164 (Site 994, 995, and 997)], and β~2.8 for Mt. Elbert formation. No grain-size dependent capillary effect is assumed in this case, $P_g=P_w$, therefore, trends apply to coarse, sandy sediments. The pore-size dependent expansion factor $\beta=f(P_w, P_c, T_g)$ computed with the PRSV-based Equation 5.3 is used in the following pore-network model simulations.

5.3 Pore-network model simulation

Let us define a pore-network model as a system of pores connected by zero-volume throats (Figure 5.2a). Capillary pressure (Equation 5.2) develops at throats and determines gas pressure and fluid movement.

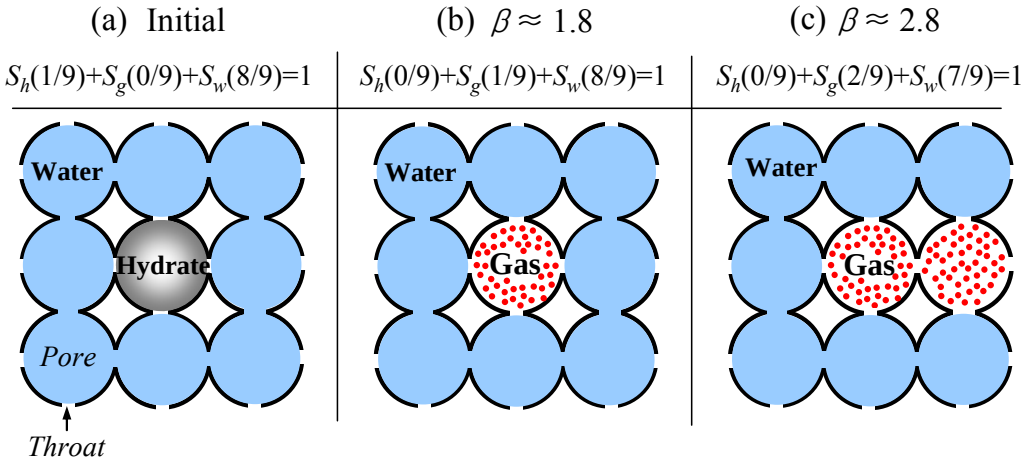

Figure 5.2. Pore-network model configuration and evolution of gas saturation during dissociation. (a) A pore-network model consists of pores interconnected by throats. Hydrate starts to dissociate and release gas when β>1. (b) Gas occupies the initially hydrate-filled pore when β≈1.8. (c) Gas expands into neighboring pores as expansion increases beyond β>1.8.

5.3.1 Model parameters

The size of pores is log-normally distributed with a characteristic mean pore size $\mu(R_p)$ and the standard deviation defined in terms of the natural logarithm of pore radius $\sigma(\ln(R_p/[\mu m]))$. Compiled mercury intrusion porosimetry data for a wide range of sediments suggest that $\sigma(\ln(R_p/[\mu m]))\approx 0.4\pm 0.2$ [Phadnis and Santamarina, 2011].

The size of any given throat is determined by the size of the two neighboring pores. The ratio of throat to pore size $\alpha=R_{th}/R_p$ is a function of the sediment packing geometry. For example, α=0.565 for simple cubic, α=0.374 for face-centered cubic, and α=0.688 for tetrahedral mono-size packings [Kruyer, 1958]. Experimentally determined values are α=0.242~0.698 for glass beads [Al-Raoush and Wilson, 2005], α=0.519 for Berea sandstone [Oren and Bakke, 2003], α=0.364~0.520 for Fontainebleau sandstone [Sok et al., 2002]. In this simulation, we set the throat size equal to half the size of the smaller of the two neighboring pores, $R_{th}=0.5\cdot min(R_{p1}, R_{p2})$; the average value α=0.5 is chosen from this compilation of theoretical and experimental values. As a result, the throat size distribution is inherently correlated with the pore size distribution.

The hydration number χ establishes the ratio between water and gas in a hydrate mass $CH_4\cdot\chi H_2O$. The theoretical hydration number χ in structure I methane hydrate is χ=5.75 (=46/8) [Sloan and Koh, 2008]. Slightly higher values (typically between 6.0 and 6.3) are found in natural and laboratory-made gas hydrates [Kida et al., 2009a; Kida et al., 2009b; Kim et al., 2005; Lu et al., 2005; Uchida et al., 1999; Ripmeester et al., 2005; Ripmeester and Ratcliffe, 1988; Sum et al., 1997; Seo et al., 2002]. The mass density of hydrates ρ_h=0.92g/cm^3 used in this study assumes full cage occupancy χ=5.75 ($8CH_4\cdot 46H_2O$) in the unit lattice whose volume is (~12Å)^3.

Capillary pressure is proportional to surface tension (Equation 5.2). The water-methane surface tension depends on pressure and temperature [Ren et al., 2000]. At a temperature of 25°C, it decreases from 0.07N/m to 0.06N/m as the pressure increases from 1.0MPa to 10MPa [Sachs and Meyn, 1995]. In this study, a constant surface tension

Γ=0.07N/m is used. The contact angle θ is assumed to be zero so that cos(θ)=1 to represent a water-wet mineral surface.

The spatially uncorrelated pore-network is generated with a pre-selected pore size distribution. Hydrates are disseminated at random to satisfy a target initial hydrate saturation S_h. Due to Ostwald ripening, we anticipate that hydrates and water do not coexist in the same pore in natural gas hydrate bearing sediments. Therefore, pores are fully filled with either hydrate or water in these simulations (see Section 5.6.1 for a detailed discussion of this hypothesis).

5.3.2 Boundary conditions

A periodic boundary is used to effectively represent a large hydrate bearing reservoir using a relatively small size 15×15×15 cubic pore-network. Pores on two parallel boundary faces are assumed to be connected to each other. Gas in the pore on one boundary can expand into the pore on the other parallel boundary face. Gas expansion continues with increasing expansion factor β until the gas cluster percolates in the flow direction towards the drainage boundary. Once a gas cluster percolates, it is no longer taken into consideration for further gas expansion since it is already connected to a drainage boundary. Gas production starts when a gas cluster percolates to the boundary and increases with gas expansion.

The algorithm properly captures the hindered expansion of fluids in pores due to the emergence of capillary pressure at pore throats. Water drains during gas expansion as long as water pores form a percolating path connected to the drainage boundary. If an isolated water pore develops during gas expansion, water remains in the pore and is not displaced by further gas expansion.

5.3.3 Hydrate dissociation and gas expansion

The simulation is run by gradually lowering the pressure at the boundary, i.e., pressure-controlled boundary conditions. The temperature is maintained constant during a given simulation. However, all results are plotted in terms of the expansion factor β. A given value of the expansion factor β can be reached by changes in either pressure or temperature, or both. Therefore, results in terms of β are valid for production strategies using depressurization or heating in the absence of secondary hydrate or ice formation, i.e., dissociation progresses slowly so that the rate of heat transport is much higher than the rate of heat consumption during hydrate dissociation (Note: ice formation during gas production would change the pore size distribution and could alter results reported here).

Furthermore, we assume that there is no pressure gradient across the network given its small length scale (Note: pressure gradient is considered in Tsimpanogiannis and Lichtner, 2006).

These assumptions allow us to anticipate the evolution of the local gas-water balance in a reservoir as a function of the fluid expansion factor β only, within the restrictions identical above. We emphasize that the gas production algorithm using pore-network models does not consider dissociation kinetics and heat conduction, and can not provide gas production rates.

During early stage of dissociation, gas remains in the same pore and displaces the water produced from hydrate dissociation. Then, gas expands to invade neighboring water-filled pores if the gas pressure P_g is higher than the water pore pressure P_w in the neighboring pore plus the capillary pressure P_c at the throat connecting the gas-filled pore and its neighboring water-filled pore:

$$P_g > P_w + P_c \qquad \text{Condition for gas invasion into a water-filled pore} \qquad (5.5)$$

The gas cluster expands into neighboring water-filled pores that have the smallest combined water and capillary pressure P_w+P_c. As the gas expands, the gas pressure decreases.

Figure 5.2 captures hydrate dissociation and gas expansion stage discussed above as a function of the fluid expansion factor β. Hydrates start to dissociate and release gas when β>1 (Figure 5.2a). When the gas expansion factor is $\beta\approx1.8$, the gas dissociated from hydrates fully occupies the pore which was initially filled with hydrates and has displaced the water produced by hydrate dissociation (Figure 5.2b). At this stage, gas saturation S_g is the same as the initial hydrate saturation S_h. Additional water drains when the gas expands to invade a neighboring water-filled pore (Figure 5.2c). The assessment of water pore connectivity and the identification of gas clusters are done using the Hoshen-Kopelman algorithm at every expansion step [Hoshen and Kopelman, 1976; Al-Futaisi and Patzek, 2003]. If two gas clusters expand to occupy neighboring pores, the two gas clusters coalesce and the pressure of the coalesced gas cluster is calculated with new gas cluster volume and the gas mass contained in two gas clusters.

5.3.4 Gas production evaluation

Gas recovery efficiency is determined at each expansion step. The gas in clusters is under high pressure P_{g1}. As soon as the gas cluster percolates, gas is produced and the pressure in the gas cluster equalizes to the external fluid pressure P_{g2}. The recovered gas $\Delta n=n_1-n_2$ [mol] is the difference between the gas n_2 remaining in the percolated gas cluster at pressure P_{g2} and the gas n_1 originally contained in the gas cluster at pressure P_{g1}. Gas recovery efficiency E is defined as the ratio of the recovered gas $\Delta n=n_1-n_2$ to the initial gas n_1 which is the same as the mass of methane contained in the initially available hydrate mass:

$$E = \frac{n_1 - n_2}{n_1} \qquad \text{Gas recovery efficiency} \qquad (5.6)$$

The gas in isolated gas clusters is not recovered and remains within the network; the cluster gas pressure is higher than the externally imposed fluid pressure.

5.3.5 Cluster visualization (in 2D)

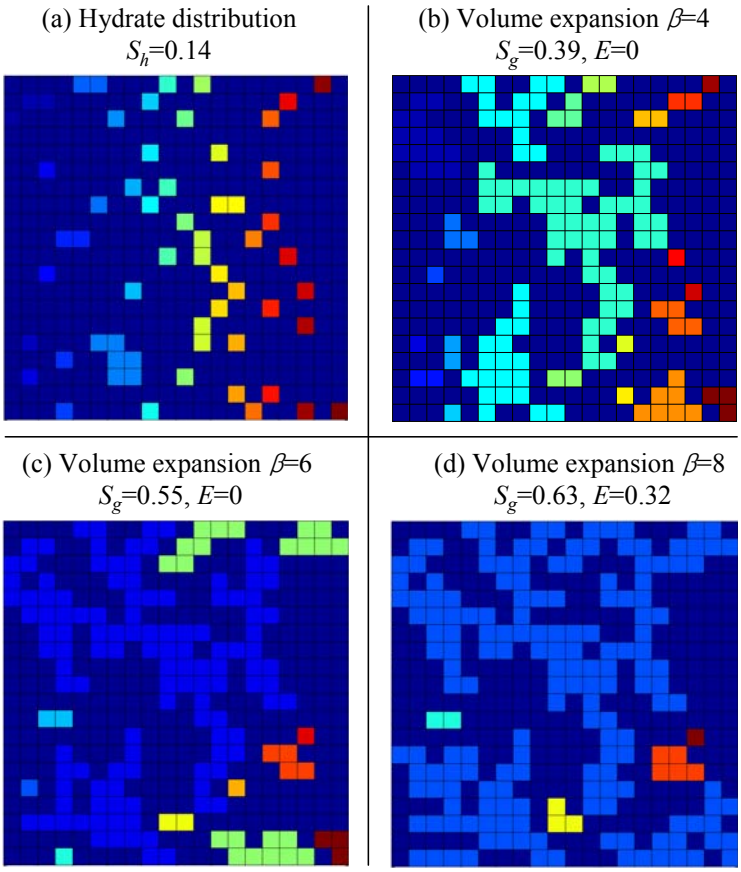

Figure 5.3. Initial hydrate distribution and evolution of gas saturation during hydrate dissociation and gas expansion. (a) Initial hydrate distribution for a hydrate saturation of S_h=15%; uncorrelated random distribution is assumed. (b)~(c) Gas cluster formation during gas expansion; the different colors indicate different gas clusters. (d) Percolating gas cluster (blue) after the completion of gas expansion (β=8) is considered for the calculation of gas recovery efficiency. Two-dimensional pore-network model with periodic boundary condition: 20×20 pores, randomly distributed pore radius with constant mean $\mu(R_p)$=1μm and standard deviation $\sigma[\ln(R_p)]$=0.4. The throat radius R_{th} between two neighboring pores is equal to half of the minimum of the two pore radii R_{th}=0.5·$min(R_p^1, R_p^2)$.

Hydrate dissociation and gas production are simulated by applying the rules and assumptions described above. To facilitate visualization, results shown in Figure 5.3 were obtained for a two-dimensional pore-network (Note: simulation parameters are listed in the figure caption). Distributed hydrates dissociate, release gas, and displace water. The gas occupies the initially hydrate-filled pores as soon as hydrates dissociate (Figure 5.3a). Gradually, gas expands into its neighboring water pores as the expansion factor β increases

(Figure 5.3b and c). Eventually, gas clusters coalesce until they percolate the pore-network horizontally and gas is produced (Figure 5.3d). Some gas clusters cannot overcome the capillary pressure and remain trapped.

Isolated water pores may be found surrounded by gas clusters. Gas clusters cannot expand into these isolated water clusters because water cannot drain. Similarly, gas clusters do not expand into neighboring water pores once gas percolates, and gas production continues from these gas clusters with the increasing expansion factor. In two-dimensional pore-networks with coordination number cn=4, the expansion of gas cluster is more often inhibited due to trapped water than in 3D networks. Therefore, the gas recovery efficiency in 2D pore-networks is lower than in 3D simulation. In the rest of this manuscript, three-dimensional pore-networks are used to compute all results (simple cubic packing, cn=6).

5.4 Numerical results

The following results are plotted in terms of the expansion factor β to generalize their validity to gas production by either thermal stimulation or depressurization in the absence of secondary hydrate or ice formation.

5.4.1 Effect of pore-network size

Pore-networks of two different sizes (15×15×15 and 15×15×30) are used to assess the size effect on gas recovery efficiency. The size of pore-networks along the two axes transverse to the flow direction are the same (15×15), but the length along the flow direction is different (15 vs. 30). Percolating gas clusters in the flow direction are considered to calculate the gas recovery efficiency. The gas recovery efficiencies computed from both pore-networks of different sizes are very similar especially for higher hydrate saturation (Figure 5.4). At low hydrate saturation (S_h≤30%), the efficiency obtained from long pore-networks (15×15×30) is slightly smaller than that of the short pore-networks (15×15×15).

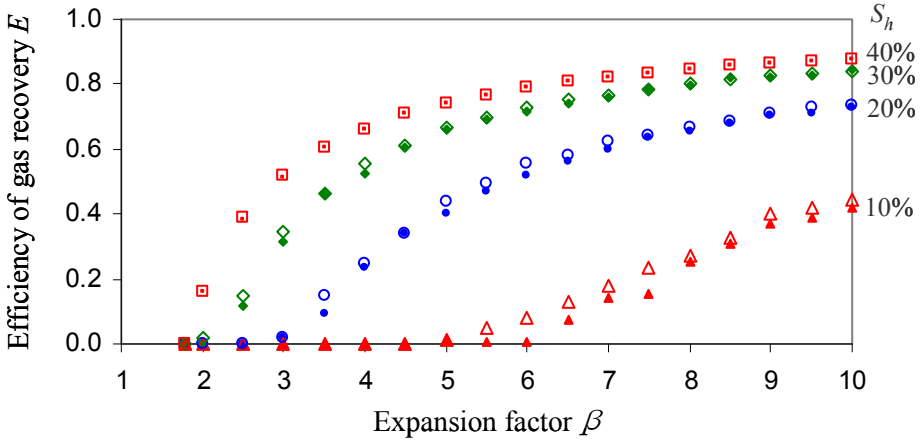

Figure 5.4. The effect of pore-network size on computed efficiency. Each point is an average of 10 realizations. Pore-network size: 15×15×30 (solid) and 15×15×15 (empty).

5.4.2 Effect of gas expansion and initial hydrate saturation

Gas recovery efficiency as a function of gas expansion factor β is obtained from simulations using different initial hydrate saturations S_h. The initial hydrate saturation varied from S_h=5 to S_h=40% (Figure 5.5 – Network parameters listed in the caption). Each data point in Figure 5.5a represents the gas recovery efficiency averaged over 20 realizations. The gas recovery efficiency E increases as the expansion factor increases at a given initial hydrate saturation, and also increases with initial hydrate saturation at a given gas expansion (Figure 5.5a).

Figure 5.5b and c show residual and isolated gas saturation. The residual gas saturation S_g^{res} is the same as the initial hydrate saturation S_h when the gas expansion factor is $\beta \approx 1.8$ (Figure 5.5b – Refer to Figure 5.2b). Gas clusters start to inter-connect and form percolating gas clusters; both residual and isolated gas saturations increase with increasing gas expansion. The isolated gas saturation starts to decrease when the residual gas saturation exceeds 30~35% as most of the gas clusters are inter-connected (Note: the percolation threshold of 3D simple cubic arrangement cn=6 is 25% [Sahimi, 1994]). Once most of the gas clusters are connected, there is not much increase in the residual gas

saturation and the gas recovery efficiency markedly increases with increasing gas expansion (Figure 5.5). At high expansion β, the residual gas saturation converges at 40~45% for all initial S_h cases. On the other hand, the maximum isolated gas saturation is less than 30%. Notice the low isolated gas saturation when S_h=40%, even at a low expansion factor β≈1.8 (Figure 5.5c) because most of the hydrate pores are initially inter-connected at such a high initial hydrate saturation.

5.4.3 Effect of pore and throat size

Throat size R_{th} (dependent of pore size R_p) defines capillary pressure (Equation 5.2), determines capillary gas trapping (Equation 5.5), and affects the gas recovery efficiency (Equation 5.6). Several mean pore radii $\mu(R_p)$=0.05μm, 0.1μm, 1μm, 10μm and 100μm with constant standard deviation in pore size $\sigma(\ln(R_p/[\mu m]))$=0.4 are simulated while maintaining the initial hydrate saturation at S_h=10% in all cases. Results show that the capillary pressure P_c at throats inhibits gas expansion, but its effect is not significant on recovery efficiency when the mean pore radius is larger than 1μm, $\mu(R_p)$>1μm (Figure 5.6a). Likewise, residual and isolated gas saturations are similar when $\mu(R_p)$>1μm (Figure 5.6b and c).

When $\mu(R_p)$<0.1μm, small throats cause high capillary pressure and inhibit gas expansion so that gas clusters are smaller and less connected. For example, the capillary pressure at a throat size R_{th}=0.05μm is P_c=2.8MPa compared to P_c=0.14MPa at the throat of radius R_{th}=1μm (see Equation 5.2 and Section 5.3). Therefore, simulations with small mean pore size $\mu(R_p)$ show low gas recovery efficiency even after pronounced expansion (Figure 5.6a). Conversely, the isolated gas saturation remains around 30% in the cases of $\mu(R_p)$=0.05 and 0.1μm while the isolated gas saturation in the case of larger mean pore $\mu(R_p)$≥1μm decreases as expansion increase (Figure 5.6c).

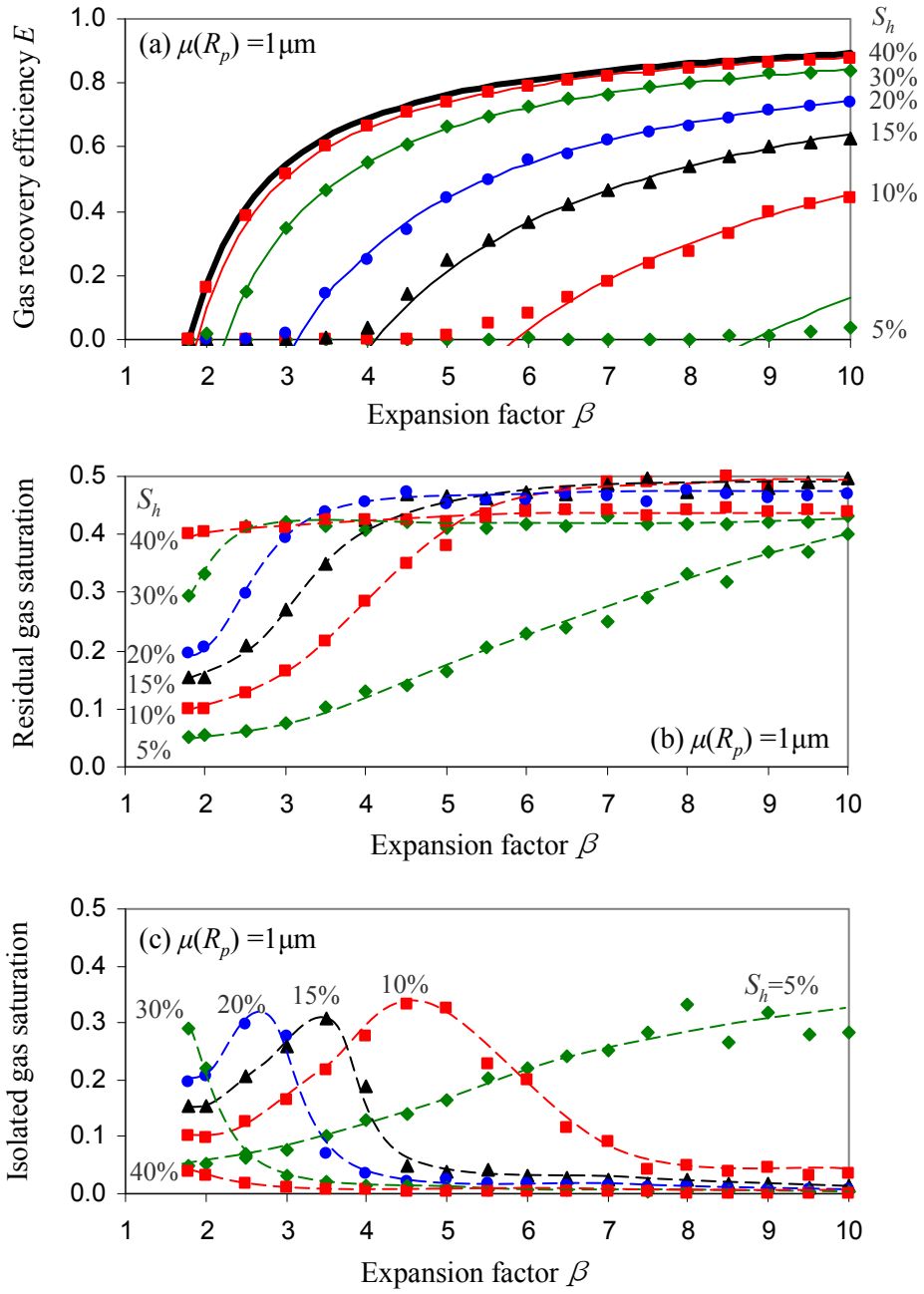

Figure 5.5. The effect of initial S_{hyd}. Gas recovery efficiency E, and evolution of residual and isolated gas saturation as a function of expansion factor β for different initial hydrate saturation S_h=5%, 10%, 15%, 20%, 30% and 40%. (a) Efficiency in gas recovery. (b) Residual gas saturation. (c) Isolated gas saturation. Each point is an average of 20 realizations. Three-dimensional pore-network model: 15×15×15 pores. Randomly distributed pore radius with constant mean $\mu(R_p)$=1μm and standard deviation $\sigma[\ln(R_p)]$=0.4. Pore throat R_{th}=0.5·$min(R_p^1, R_p^2)$. Note: Symbols: numerical results (panes a, b, and c), Thin and thick lines: analytical model (pane a), Broken lines: trend added to facilitate the visualization of numerical results (panes b and c).

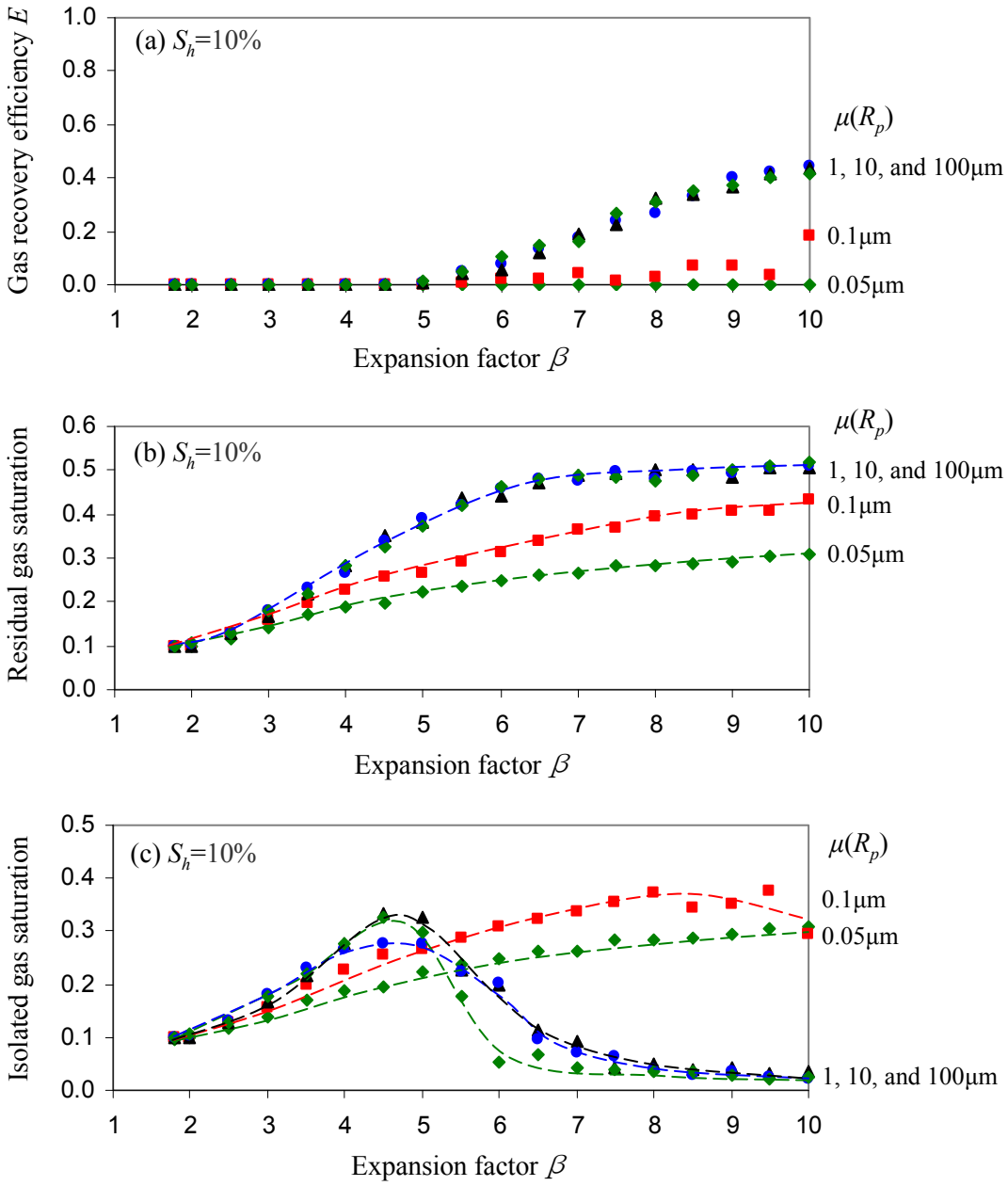

Figure 5.6. The effect of mean pore size. Gas recovery efficiency E, and evolution of residual and isolated gas saturation as a function of expansion factor β for various mean pore size $\mu(R_p)$=0.05, 0.1, 1, 10, and 100µm. Initial hydrate saturation S_h=15%. (a) Efficiency in gas recovery. (b) Residual gas saturation. (c) Isolated gas saturation. Each point is an average of 20 realizations. Three-dimensional pore-network model: 15×15×15 pores. Randomly distributed pore radius with constant mean $\mu(R_p)$=1µm and standard deviation $\sigma[\ln(R_p)]$=0.4. Pore throat $R_{th}=0.5 \cdot min(R_p^1, R_p^2)$. Note: Symbols: numerical results (panes a, b, and c), Broken lines: trend added to facilitate the visualization of numerical results (panes b and c).

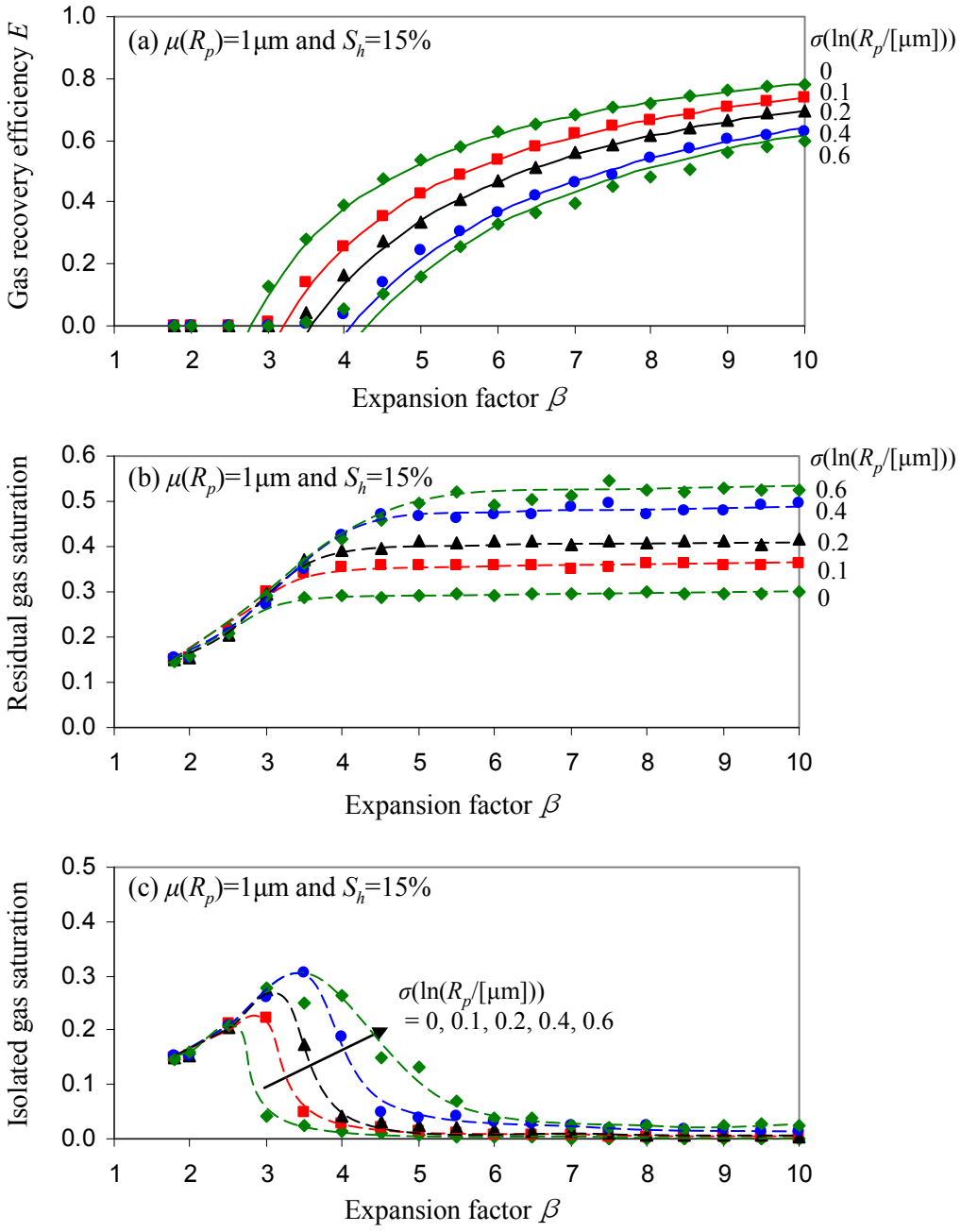

Figure 5.7. The effect of pore size variability. Gas recovery efficiency E, and evolution of residual and isolated gas saturation as a function of the pore size variability in terms of standard deviation for a lognormal pore size distribution: $\sigma[\ln(R_p/[\mu m])]$=0 (uniform distribution), 0.1, 0.2, 0.4, and 0.6. Initial hydrate saturation S_h=15%. (a) Efficiency in gas recovery. (b) Residual gas saturation. (c) Isolated gas saturation. Each point is an average of 20 realizations. Three-dimensional pore-network model: 15×15×15 pores. Randomly distributed pore radius with constant mean $\mu(R_p)$=1μm. Pore throat R_{th}=0.5·$min(R_p^1, R_p^2)$. Note: Symbols: numerical results (panes a, b, and c), Thin and thick lines: analytical model (pane a), Broken lines: trend added to facilitate the visualization of numerical results (panes b and c).

5.4.4 Effect of pore size variability

The effect of pore size variability in terms of standard deviation in pore size $\sigma(\ln(R_p/[\mu m]))$ on the gas recovery efficiency is shown in Figure 5.7. As the standard deviation in pore size increases, the gas recovery efficiency decreases (Figure 5.7a). Conversely, the residual gas saturation when pore size is uniform $\sigma(\ln(R_p/[\mu m]))\rightarrow 0$ is lower than when pore size is well distributed $\sigma(\ln(R_p/[\mu m]))>0$ (Figure 5.7b).

These results can be understood by noting that: (1) the number of small pores increases as the standard deviation in pore size $\sigma(\ln(R_p/[\mu m]))$ increases for a constant mean pore size $\mu(R_p)$; and (2) the throat size depends on the smaller size of neighboring pores. Therefore, the mean throat size $\mu(R_{th})$ decreases as the standard deviation in pore size $\sigma(\ln(R_p/[\mu m]))$ increases (from $\mu(R_{th})=0.5\mu m$ to $0.34\mu m$ as the standard deviation changes from $\sigma(\ln(R_p/[\mu m]))=0$ to 0.6 even though the mean pore size remains constant $\mu(R_p)=1\mu m$).

5.5 Analytical solution for gas recovery efficiency

Let's derive an expression for gas recovery efficiency based on macro-scale concepts, but guided by pore-scale information gathered from the previous pore-network simulations. Figure 5.8a shows the initial pore volume V_p occupied by hydrate and water in a gas-limited hydrate bearing sediment. Figure 5.8b through 5.8e show the volumes of gas and water for several production scenarios. The volume of water V_w^{dis} that results from hydrate dissociation is $V_w^{dis}=0.79V_h^{ini}$ where V_h^{ini} is the initial hydrate volume (for a theoretical hydration number $\chi=5.75$ - see Section 5.2). The combined volume of gas and water from dissociation is equal to $V_g^{dis}+V_w^{dis}=\beta V_h^{ini}$. The gas recovery efficiency $E=V_g^{rec}/V_g^{dis}$ is a function of the gas expansion factor $\beta=(V_g^{dis}+V_w^{dis})/V_h^{ini}$, the residual gas saturation $S_g^{res}=V_g^{res}/V_p$, and initial hydrate saturation $S_h=V_h^{ini}/V_p$. Several production cases are analyzed next.

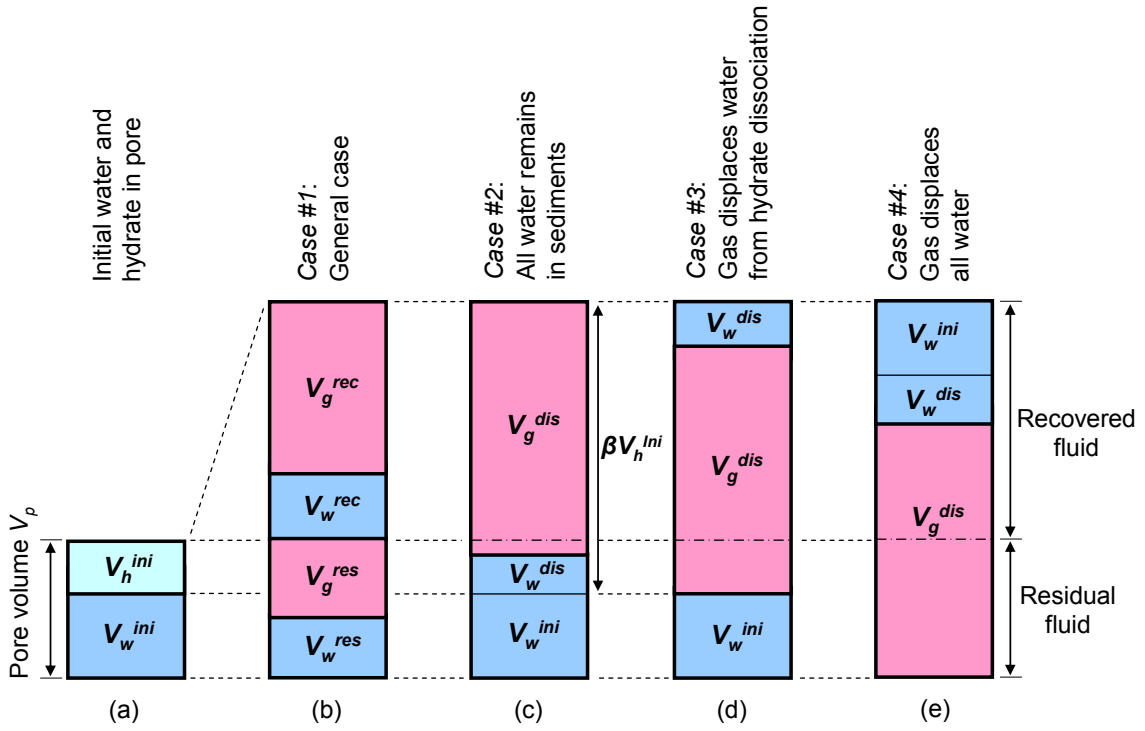

Figure 5.8. Macroscale analysis. Several cases of gas and water production during hydrate dissociation and gas expansion. (a) Initial hydrate and water saturation. (b) Gas displaces water and fills the pores in sediments. (c) All water remains in sediments (S_g^{res}=0.21S_h). (d) Gas displaces the water from hydrate dissociation (S_g^{res}=S_h). (e) Gas displaces all water (S_g^{res}=1).

Case #1: Gas displaces water (both initial and from dissociation - Figure 5.8b). Then, efficiency depends on residual gas saturation S_g^{res},

$$E_1 = \frac{V_g^{rec}}{V_g^{dis}} = \frac{V_g^{dis} - V_g^{res}}{V_g^{dis}} = \frac{\beta V_h^{ini} - 0.79 V_h^{ini} - V_g^{res}}{\beta V_h^{ini} - 0.79 V_h^{ini}}$$
$$= \frac{\beta - 0.79 - S_g^{res} / S_h}{\beta - 0.79} \quad (0.21 S_h \le S_g^{res} \le 1) \tag{5.7}$$

Case #2: All the water (both initial V_w^{ini} and from dissociation V_w^{dis}) remain within the sediment (Figure 5.8c). In this case, the residual gas saturation becomes S_g^{res}=1-S_w=1-(S_w^{ini}+S_w^{dis})=1-(1-S_h)-0.79S_h=0.21S_h. Then,

$$E_2 = \frac{V_g^{rec}}{V_g^{dis}} = \frac{V_g^{dis} - 0.21V_h^{ini}}{V_g^{dis}} = \frac{\beta V_h^{ini} - V_h^{ini}}{\beta V_h^{ini} - 0.79V_h^{ini}}$$
$$= \frac{\beta - 1}{\beta - 0.79} \tag{5.8}$$

This case could apply to a water-limited reservoir where gas percolates. Then, high gas recovery efficiency could be reached (Equation 5.8) because the dissociated gas is produced along the existing percolating gas path as soon as hydrates dissociate.

Case #3: Gas displaces only the water from dissociation V_w^{dis} (Figure 5.8d). In this case, gas will occupy the space initially filled with hydrate and the residual gas saturation becomes $S_g^{res} = S_h$. Then, the gas recovery efficiency is

$$E_3 = \frac{V_g^{rec}}{V_g^{dis}} = \frac{V_g^{dis} - V_h^{ini}}{V_g^{dis}} = \frac{\beta V_h^{ini} - 1.79V_h^{ini}}{\beta V_h^{ini} - 0.79V_h^{ini}}$$
$$= \frac{\beta - 1.79}{\beta - 0.79} \tag{5.9}$$

Case #4: Gas displaces all water, both initial and from dissociation $V_w^{ini} + V_w^{dis}$, before gas recovery begins so that $S_g^{res} = 1$ (Figure 5.8e). Then,

$$E_4 = \frac{V_g^{rec}}{V_g^{dis}} = \frac{V_g^{dis} - V_v}{V_g^{dis}} = \frac{\beta V_h^{ini} - V_w^{dis} - V_v}{\beta V_h^{ini} - V_w^{dis}} = \frac{\beta V_h^{ini} - 0.79V_h^{ini} - V_v}{\beta V_h^{ini} - 0.79V_h^{ini}}$$
$$= \frac{\beta - 0.79 - 1/S_h}{\beta - 0.79} \tag{5.10}$$

From a gas production point of view, this is the worst scenario.

Numerical simulations presented in Figure 5.4 through 5.7 assumed that all the water that resulted from hydrate dissociation is displaced from the pore and that water in initially water-filled pores can be also displaced during gas expansion. Therefore, simulation results show an intermediate efficiency between the values obtained by case #3

(Equation 5.9) and case #4 (Equation 5.10). The thin lines in Figure 5.5a and 5.7a show the gas recovery efficiency obtained by the general analytical solution (case #1 Equation 5.7) using the numerically predicted residual gas saturation for each hydrate saturation (Figure 5.5b and Figure 5.7b). Analytical results are consistent with the numerical results (There is some discrepancy for the case of low hydrate saturations S_h<10% in Figure 5.5a).

When the initial hydrate saturation exceeds S_h>40%, gas recovery efficiencies from numerical simulations are similar to case #3 (Figure 5.8d). In fact, the thick line in Figure 5.5a is obtained using Equation 5.9. This result shows that when the initial hydrate saturation is high, hydrate-filled pores are inter-connected and eventually become a percolating path for gas production. Therefore, gas is produced without the need to invade neighboring water-filled pores during gas expansion, resulting in high gas recovery efficiency.

5.6 Discussion

5.6.1 Hydrate habit in pores – Ostwald ripening

We assumed full hydrate occupancy as a starting point for our simulations, in apparent contradiction to some laboratory observations. However, we note that hydrate formation experiments in the laboratory are conducted within relatively short-times compared to the long geological time involved in hydrate formation in natural sediments [Tohidi et al., 2001; Katsuki et al., 2006 2007 2008]. In fact, pore-scale experiments clearly show a pronounced transient behavior during early hydrate formation, involving formation/dissolution cycles within stability *P*-*T* conditions [Jung, 2010].

In long-time conditions, the higher saturation around smaller nuclei promotes diffusion from small nuclei towards larger ones. Therefore a large crystal will tend to grow at the expense of smaller neighboring nuclei (Ostwald ripening). This diffusion-controlled aging process alters the crystal size distribution with time [Myerson, 2002; Salamatin et

al., 2003]. For example, data gathered for in-situ N_2 and O_2 hydrates in polar ice show the change in crystal size distribution through Ostwald ripening [Pauer et al., 1999; Uchida et al., 1994; Salamatin et al., 2003]. Our assumption of full pore occupancy reflects Ostwald ripening.

5.6.2 Macro-scale vs. Pore-scale analyses

At the macro-scale, gas production is determined by the "characteristic curve" of the sediment, i.e., the (u_g-u_w)-vs-S_g trend. This curve depends on pore size distribution and connectivity. Pore-scale models inherently capture this behavior and naturally produce the residual water and gas saturation as a function of pore size distribution, initial hydrate saturation and pore connectivity.

5.6.3 Field situations

Our simulations are pressure-controlled. Yet, results plotted in terms of the expansion factor β are relevant to gas production by either thermal stimulation or depressurization in the absence of secondary hydrate or ice formation. Likewise, the analytical solution for the recovered gas volume is applicable to both depressurization and thermal stimulation (Equations 5.7~5.10 – Figure 5.8). Note that iso-expansion lines superimpose on the phase boundary, i.e., P-T conditions remain on the phase boundary during volume expansion until all the hydrate mass has dissociated. This study does not capture endothermic dissociation and heat conduction. Therefore, results provide recoverable gas but can not be used to predict rate.

Results show that fluid expansion factor β determines gas recovery efficiency (all else being constant). Deeper reservoirs will have a higher initial P_0 and will require a higher depressurization $\Delta P=P_0-P_f$ to attain the same fluid expansion β and gas recovery efficiency (Note: higher temperatures at depth may support higher production rates).

Gas recovery efficiency away from the production well should consider the fluid expansion factor as a function of pressure during depressurization, i.e., the distance from the production well in depressurization-based production. Therefore, gas recovery efficiency E is inversely proportional to the distance from the bore-hole.

5.6.4 Sediment internal stability during gas production

Hydrate dissociation in clayey sediments can induce gas-driven fracture formation due to high capillary entry pressures compared to the in-situ effective stress σ_3' [Shin and Santamarina, 2010]. Let's make an order of magnitude estimation of this condition.

The pore size or distance d between clay particles can be estimated from the sediment specific surface S_s [m^2/g] and porosity n as $d=2n/[(1-n)\cdot S_s\cdot\rho_m]$ where ρ_m [g/m^3] is the mineral mass density. Then, the Laplacian capillary pressure $P_c=2\Gamma/d$ can be written as

$$P_c = \frac{2\Gamma}{d} = \Gamma S_s \rho_m \frac{1-n}{n} \tag{5.11}$$

For example, the sediment in the Krishna-Godavari basin in India has a porosity $n\approx0.62$ and specific surface $S_S\approx90 m^2/g$ (see sediment data in Yun et al. 2010), so the capillary entry pressure is $P_c\approx10$MPa.

An estimate of the effective stress σ_3' starts by recognizing that typical depths for the gas hydrate stability zone in the ocean are shallower than 800mbsf [MacDonald, 1990; see data compiled in Figure 5.1]. This implies a maximum horizontal effective stress $\sigma_3' \leq 0.5\times8\text{MPa}=4\text{MPa}$ expected in marine hydrate bearing sediments.

These results suggest that hydrate dissociation will induce gas-driven fracture $\sigma_3'<P_c$ even at slow dissociation rates in fine-grained sediments. Gas recovery efficiency in the fracturing regime is beyond the scope of the analysis presented in this manuscript.

5.6.5 Gas migration

Let's analyze the gas migration in a single pore due to buoyancy. The ratio between the buoyant force and the capillary resistance is (Bond number - Pennell et al., 1996):

$$B = \frac{F_{buoyancy}}{F_{capillary}} = \frac{\Delta\rho\, g\, V_p}{2\pi R_{th}\Gamma} = \frac{\Delta\rho\, g\, R_p^2}{3\Gamma} \tag{5.12}$$

where $\Delta\rho$ is the density difference between gas and fluid, V_p is the volume of pore $V_p = 4\pi R_p^3/3$, and the throat radius R_{th} is half of the pore radius $R_{th}=0.5R_p$. Buoyancy and capillary resistance are equal, i.e., $B=1$, when $R_p \approx 4.6$mm (assumed that $\Delta\rho \approx \rho_w$). Therefore, gas in a single pore will not migrate even in coarse clean sand. However, tall gas clusters can create the buoyancy drive required to allow them to migrate through intermediate grain size sediments without causing sediment instability [Geistlinger et al., 2006; Santamarina and Jang, 2010].

5.7 Conclusions

Proper pressure and temperature, and the availability of methane are required for hydrate formation. Yet, hydrate distribution and saturation in hydrate bearing sediments are determined by the sediment pore size distribution, connectivity, and spatial variability. These sediment characteristics also affect recoverable gas, the evolution of gas saturation, and the sediment internal stability during production.

Pore-network models permit the study of recoverable gas using a minimal set of pore-scale parameters. Pore-network simulation results can guide the selection of physically meaningful parameters for capillary pressure functions and relative permeability equations adopted in FEM simulations.

There is a pronounced hydrate-to-fluid volume expansion across the hydrate phase boundary. Additional expansion occurs during heating and depressurization after dissociation. Gas expansion is hindered in fine-grained sediments due to capillarity in small pores.

A simple close-form approximation can be derived for the expansion factor β using the modified ideal gas law. The hydrate-to-fluid volume expansion is primarily determined by the final fluid pressure imposed on the boundary P_f. A given depressurization $\Delta P = P_o - P_f$

will cause higher fluid volume expansion in shallower reservoirs with lower initial pressure P_o.

The recoverable gas increases with gas expansion and with hydrate saturation. There is very low gas recovery in hydrate bearing sediments with low hydrate saturation (S_h<~5~10%), even when high gas expansion conditions are imposed.

The effect of pore size on gas recovery efficiency vanishes when the mean pore size is larger than 1μm. A mean pore size smaller than 1μm limits the gas recovery efficiency because small pore throats cause high capillary pressures, limit gas expansion, and lead to capillary trapping. However, highly conductive gas-driven fractures may form in fine-grained sediments and facilitate gas migration.

Gas recovery efficiency, defined as the ratio between the recovered and the initial mass of gas, can be estimated using macro-scale analytical solutions verified against numerical results:

$$\frac{\beta - 0.79 - 1/S_{hyd}}{\beta - 0.79} \le E \le \frac{\beta - 1.79}{\beta - 0.79}$$

where β is the fluid expansion factor and S_h is the initial hydrate saturation.

The gas recovery efficiency approaches the upper estimate when the hydrate saturation exceeds S_{hyd}>40. In water limited systems, the recoverable gas approaches

$$E = \frac{\beta - 1}{\beta - 0.79}.$$

$$E = \frac{\beta - 1}{\beta - 0.79}.$$

CHAPTER 6

GAS PRODUCTION FROM HYDRATE-BEARING SEDIMENTS

- EMERGENT PHENOMENA -

6.1 Introduction

Gas production from hydrate-bearing sediments causes fluid volume expansion, gas and water flow, temperature decrease due to endothermic hydrate dissociation, ice and secondary hydrate formation, softening of the sediment skeleton and changes in porosity and effective stress. Other phenomena may develop as well, including fines migration and clogging [Kampel et al., 2008; Valdes et al., 2008], sand production [Papamichos et al., 2001], grain crushing [Guimaraes et al., 2007], and gas-driven fractures in sediments [Santamarina and Jang, 2009; Shin and Santamarina, 2010]. These emergent processes may cause sediment instability, formation clogging, bore hole failure, retardation of gas production and low gas recovery efficiency.

Several numerical simulators have been developed to analyze gas production from hydrate-bearing sediments [Rutqvist et al., 2009; Wilder et al., 2008; Kwon et al., 2008; Garg et al., 2008; Moridis et al., 2007; Ahmadi et al., 2004]. These analytical and numerical models capture the fundamental thermodynamic conditions in hydrate-bearing sediments, but have not yet considered emergent phenomena such as those identified above.

Small-scale laboratory experiments have focused on the effect of pressure, temperature, and inhibitors on the hydrate dissociation rate and the cumulative amount of produced gas [Kawamura et al., 2009; Tang et al., 2005; Linga et al., 2009a; Linga et al., 2009b; Kono et al., 2002; Oyama et al., 2009]. Large-scale laboratory experiments of gas production from hydrate-bearing sediments are needed to identify potential emergent phenomena which may hinder (or help) gas production. Yet, large-scale testing is

particularly challenging in the study of hydrate-bearing sediments because of the high pressure needed to attain stability conditions, the need for concurrent effective stress control, and ensuing safety considerations

In this study, we used the large-scale Seafloor Process Simulator (SPS) at the Oak Ridge National Laboratory [Phelps et al., 2001]. The test sequence was designed to explore production-related phenomena that would not be observed in smaller cells using typical experimental designs

6.2 Experimental study

6.2.1 Devices

Seafloor Process Simulator (SPS). This 72-L vessel is constructed from corrosion-resistant Hastelloy (Figure 6.1a). The simulator has a maximum 21MPa working pressure, and 41 ports for instrumentation. It is housed inside of a cold room with a working temperature range from -2 to 20°C.

Instrumented soil chamber. A stainless steel soil chamber is placed inside the SPS (Figure 6.1b). The fixed bottom plate has a fluid injection port. The perforated top plate allows for free-gas and water flow and can move up and down depending on the sediment volume change. A spring (k=306N/cm) rests on the top plate and is used to apply a pre-determined effective stress on the sediment while maintaining zero lateral-strain conditions. In this study, a nominal 100kPa vertical effective stress is applied to the sediment in all tests.

Instrumentation. The sediment vertical displacement during hydrate formation and gas production is measured using a Linear Variable Differential Transformer (LVDT) that rests on the top plate of the internal soil chamber (Figure 6.1b). Three pairs of bender elements are located at different heights in the sediment (Figure 6.1b). The source bender elements in each pair are connected to a signal generator which sends a step function signal every 20

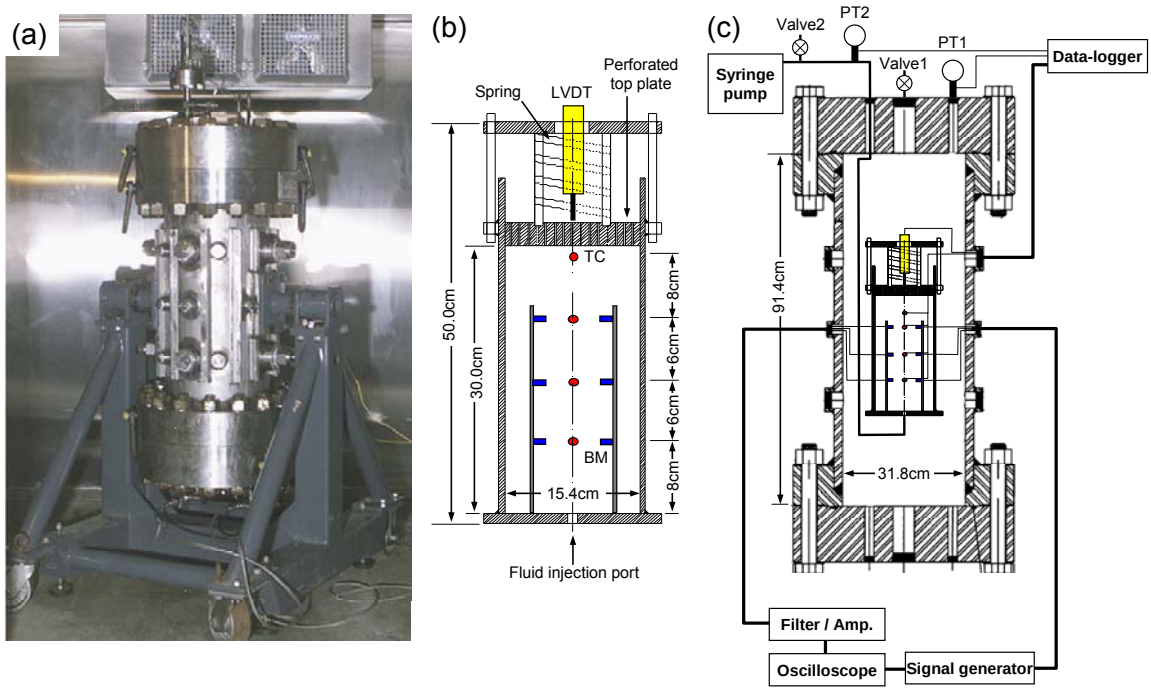

Figure 6.1. Devices and instrumentation: (a) Seafloor Process Simulator. (b) Internal instrumented soil cell; LVDT for sediment displacement measurements, bender element BM for S-wave velocity measurements, and thermocouples TC for temperature measurements (c) Complete system including peripheral electronics and pressure transducers for pressure measurement.

ms; the receiver bender elements are connected to a pre-amplifier and a digital storage oscilloscope. Three thermocouples are buried in the sediment at the same heights as the three pairs of bender elements. A fourth thermocouple is located inside the fluid injection port of the internal chamber, and a fifth thermocouple is located inside the SPS to measure the gas temperature. A pressure transducer is inserted into the SPS to provide gas pressure measurements, and a second one is connected to the fluid injection port at the bottom plate of the internal soil chamber. A data logger is used to record all pressures, temperatures, and the vertical displacement every four seconds.

Sediments. The first two tests (Test #1 and #2) involved clean Ottawa 20/30 sand (passing US standard #20 sieve of size 850μm, but being retained on #30 sieve of size 600μm),

which was placed in the soil chamber with an initial porosity n=0.4 at dry condition. A mixture of Ottawa 80/140 sand (passing US standard #80 sieve of size 180μm, but being retained on #140 sieve of size 106μm) and kaolinite clay whose size is 4.5~6.0μm was used for additional two tests (Tests #3 and #4), packed at an initial porosity n=0.35; the initial water content was S_w=0.5 for Test #3 and 0.65 for Test #4.

6.2.2 Test procedure

All tests involved four main stages: (1) specimen preparation, (2) hydrate formation, (3) water injection and drainage, and (4) hydrate dissociation. And we used CO_2 hydrate for safety restriction. CO_2 gas forms structure I hydrate which is the same structure as methane hydrate.

Specimen preparation. The instrumented soil chamber was initially filled with the selected sediment while sensors were placed at appropriate locations. Then, the vertical effective stress was applied using the spring-based loading system. Finally, the chamber was placed inside the SPS where all fluid and electrical connections were established. Table 6.1 summarizes sediment conditions in each of the tests. The clean Ottawa 20/30 sand was placed in dry condition in Tests #1 and #2; then, a water table was established at ~6 cm from the bottom (see Table 6.1). In Tests #3 and #4, kaolinite was saturated with pre-calculated amount of water that was mixed with Ottawa 80/140 sand to have target initial water saturation, until a homogeneous sample was formed. A water table was established at ~6 cm from the bottom. In all tests, the sediment was densified by rodding at each layer to attain the desired porosity, barely invading the previously rodded lower layer. Also, rodding is done carefully to prevent damaging the sensors.

Hydrate formation. The SPS was kept in a cold room at about 4°C in all experiments. The SPS was pressurized with CO_2 to ~3.4 MPa and kept inside the CO_2 hydrate stability field overnight.

Table 6.1. Summary of test conditions and procedures

	Measurements	Soil type/Initial conditions	Procedure
Test 1	Pressure (1) Temperature (4) S-wave (2 pairs)	Ottawa 20/30 sand Porosity n=0.4 Dry soil 6 cm water table	Set-up the chamber Pressurize chamber and lower T* First water injection and drainage Second water injection Depressurize SPS (top plate)
Test 2	Pressure (2) Temperature (4) S-wave (2 pairs) Surface settlement	Ottawa 20/30 sand Porosity n=0.4 Dry soil 7 cm water table	Set-up the chamber Pressurize chamber and lower T* First water injection and drainage Second water injection Depressurize SPS (top plate)
Test 3	Pressure (2) Temperature (6) S-wave (3 pairs) Surface settlement	95% Ottawa 80/140 sand + 5% Kaolinite Porosity n=0.35 Initial water saturation S_w=0.5	Set-up the chamber Pressurize chamber and lower T* First water injection and drainage Second water injection and drainage Third water injection and drainage Depressurize SPS (top plate)
Test 4	Pressure (2) Temperature (6) S-wave (3 pairs) Surface settlement	95% Ottawa 80/140 sand + 5% Kaolinite Porosity n=0.35 Initial water saturation S_w=0.65	Set-up the chamber Pressurize chamber and lower T* First water injection and drainage Second injection using salt water Drainage and depressurization through the bottom port

Note: * operating environmental conditions are P = ~3.4 MPa, T = ~4ºC

Water injection and drainage. De-ionized degassed water was injected into the gas-rich sediment at an injection rate of 8ml/min through the port in the bottom plate. The water was then quickly (in 20min) drained through the same port used for injection. Various injection and drainage cycles were imposed in the different tests (Table 6.1).

Hydrate dissociation. Hydrate was eventually dissociated via depressurization. First, the SPS pressure is lowered to a value near the hydrate phase transformation boundary. Then, depressurization continued either through the SPS pressure port so that the sediment lost pressure from the top plate (slow depressurization for Tests #1 and #2, and fast depressurization for Test #3), or through the bottom fluid port in the internal chamber (Test #4).

6.3 Experimental results

Pressure-temperature histories during hydrate formation, growth, water injection, drainage, and dissociation were obtained during the tests to monitor the sediment response during hydrate formation and dissociation.

6.3.1 Hydrate formation

There was no evidence of hydrate formation in the dry sediment with low water level in Tests #1 and #2 during the first ~14 hrs within stability P-T conditions (Note: the capillary rise in this sand is ~58 mm). However, the partially water saturated sediment in Tests #3 and #4 spontaneously started to form hydrate after approximately 1 hour within the P-T conditions for CO_2 hydrate stability (Figure 6.2a). Correspondingly, the hydrate formation caused the S-wave velocity and temperature to increase and pressure to decrease. The internal thermocouples show that the reaction affected the sediment temperature for more than ~8 hrs particularly at the center of the specimen (Figure 6.2a).

6.3.2 Water injection in a gas-filled hydrate-free sediment

The first gas-free water injection caused hydrate formation in the sediment without fines as indicated by temperature increase (Test #2 – Figure 6.2b). The initial injection lasted 3.5 hours and the water front moved up at a rate of 76 mm/hr in agreement with the timing of temperature peaks. The S-wave velocity increased where hydrate formed (Figure 6.3). The second injection of gas-free water dissolved hydrate near the entry port and the

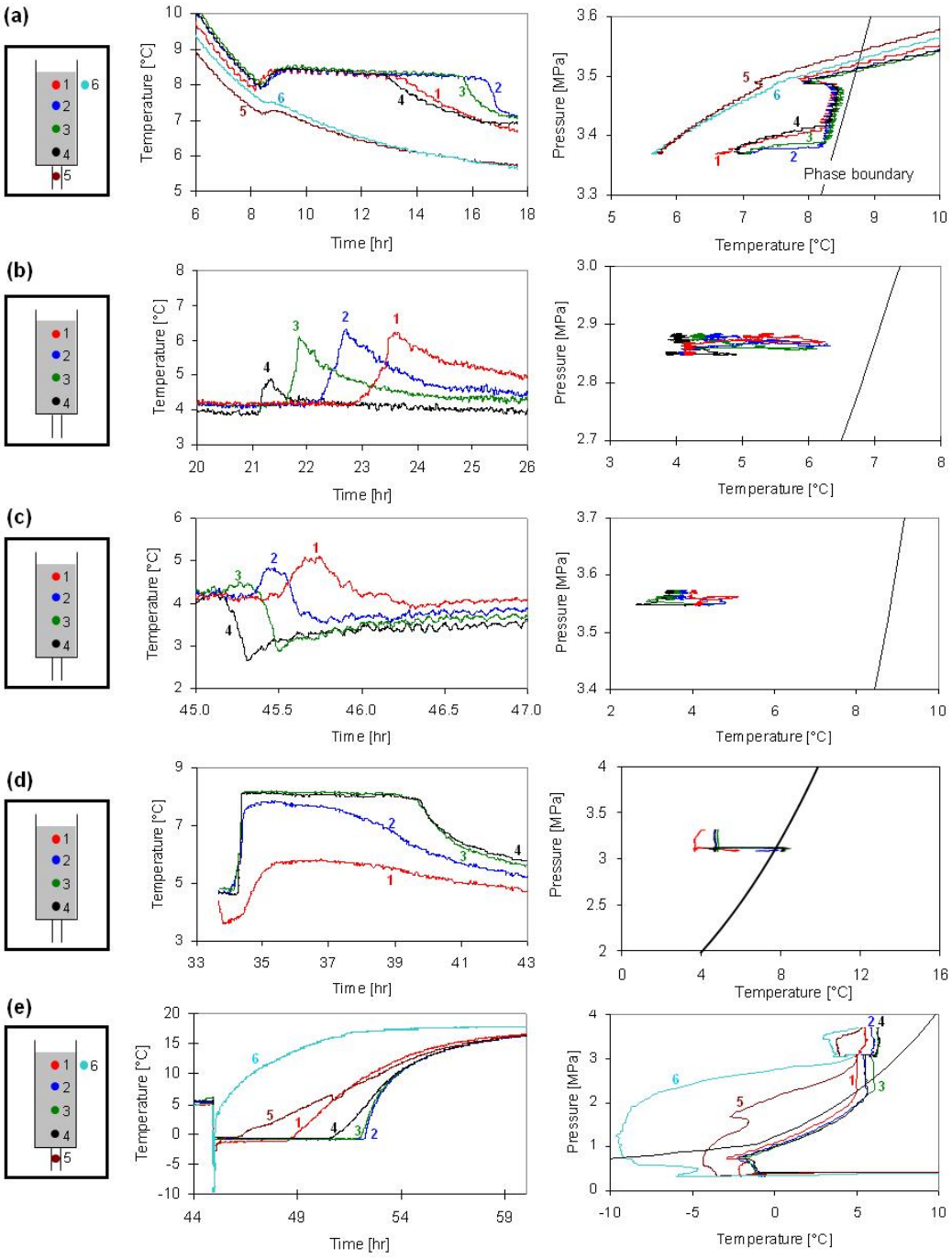

Figure 6.2. Pressure and temperature histories during hydrate formation. (a) Spontaneous hydrate formation in a gas-filled sand-clay mixture with initial water saturation S_w=50% (Test #3). (b) Hydrate formation in an initially dry, gas-filled sand triggered by water injection (Test #2). (c) Hydrate formation and dissolution during deaired-water injection in gas-filled sand that had some initial hydrate saturation (Test #2). (d) Hydrate formation in an initially water saturated sand triggered by water drainage and gas invasion (Test #1). (e) Hydrate dissociation by depressurization (final stage in Test #3).

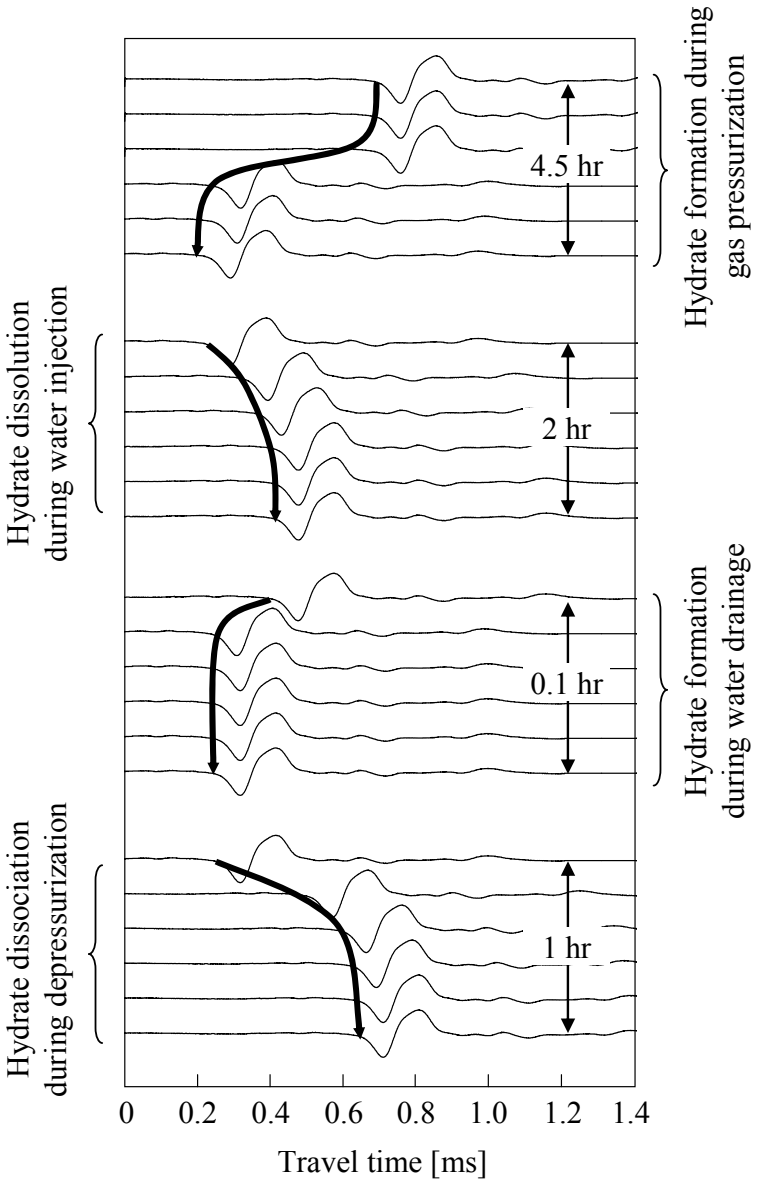

Figure 6.3. S-wave velocity changes during hydrate formation, dissolution, and dissociation (Test #3).

temperature decreased (Figure 6.2c - thermocouple #4). The S-wave velocity increased when hydrate formed and decreased when hydrate dissolved (Figure 6.3).

6.3.3 Water drainage and gas invasion

Hydrate formed when water drainage was allowed (Figure 6.2d) and the invading gas phase reacted with the residual free water left behind. Water was drained in 20 min while the reaction continued for about ~3 hrs (Figure 6.2d). Note the cooling accompanied depressurization near the drainage port (see the response of thermocouple #4).

6.3.4 Hydrate dissociation

The sediment temperature decreased following the fast depressurization (from an initial pressure near the CO_2-hydrate phase boundary, Figure 6.2e, Test #3). Free water formed ice, as indicated by the constant temperature of 0°C.

6.4 Analyses and discussion

6.4.1 Fluid flow and hydrate formation

A water-gas mixture may remain inside the thermodynamic hydrate-stability field without forming hydrate for a long time under quiescent conditions. Conversely, hydrate formation is observed if the sediment is subjected to a triggering mechanism such as agitation, mechanical shock, and shear [Mullin, 2001]. Results in Figure 6.2 clearly show that water flow, gas invasion, and increase in interfacial area between water and gas are effective hydrate formation triggers as well.

6.4.2 Hydrate dissolution

The injection of CO_2-free water in hydrate-bearing sediments induced hydrate dissolution, as indicated by the temperature drop near the injection port in Figure 6.2d (trace 4). The amount of hydrate that will dissolve in a pore volume of gas-free water can be estimated from the mass balance of CO_2 gas in the system as a function of water density ρ_{water}=1g/cm^3, hydrate density ρ_{hyd}, gas solubility in water C_{gas}^{w} [mol/kg], gas molar concentration in hydrate C_{gas}^{hyd} [mol/kg], and the water saturation S_w. The change in hydrate saturation ΔS_h for each pore volume of gas-free water that is replaced during injection is

(Note: the amount of water from hydrate dissolution is assumed small compared to the pore volume),

$$\Delta S_h = \frac{C_{gas}^{w}}{C_{gas}^{hyd}} \frac{\rho_w}{\rho_{hyd}} S_w \qquad \text{per pore volume} \qquad (6.1)$$

For CO_2 hydrate ρ_{hyd}=~1.11 g/cm^3, C_{CO2}^{w} =0.89 mol/kg, C_{CO2}^{hyd} =6.58 mol/kg at P=3MPa and T=273K [Aya et al., 1997; West et al., 2003], Equation 6.1 becomes,

$$\Delta S_h \approx 0.12 S_w \qquad \text{for } CO_2 \text{ hydrate} \qquad (6.2)$$

For CH_4 hydrate ρ_{hyd}=~0.94 g/cm^3, C_{CH4}^{w} =0.06 mol/kg, C_{CH4}^{hyd} =8.20 mol/kg at P=3MPa and T=273K, Equation 6.1 anticipates,

$$\Delta S_h \approx 0.008 S_w \qquad \text{for } CH_4 \text{ hydrate} \qquad (6.3)$$

The computed values are per pore volume of gas-free water, and in our experiment, hydrates near water injection port will experience more enhanced dissolution.

6.4.3 Fines migration

Test specimens were dissected at the end of each test and grain size using sieve analyses were obtained at six equally spaced locations. Fines migrated toward the top of the sediment column when depressurization occurred through the top plate (e.g., Test #3, Figure 6.4a). However, fines migrated towards the lower part of the sediment column when depressurization occurred through the bottom port of the chamber (e.g., Test #4, Figure 6.4b).

Fines migration and clogging depend on geometric constraints, such as the relative size of the migratory fines with respect to the pore throat size in the host sediment skeleton. A single particle with diameter *d* can migrate through a packing of grains size *D* when *D/d*>2.4 (simple cubic) to *D/d*>6.4 (cubic tetrahedral). When many migrating particles reach a pore throat at once, 3-to-5 migrating particles can form a bridge;

therefore, clogging can occur when migrating fines are D/d=12-to-30 times smaller than the sediment grains [Valdes et al., 2008].

The particle diameter D of Ottawa 80/140 sand is ~0.105 mm and the particle diameter d of kaolinite is 4.5-6.0μm. Given that D/d ~20, single kaolin particles can migrate through the sediment; indeed, data in Figure 6.4 confirm that small particles migrated during gas production.

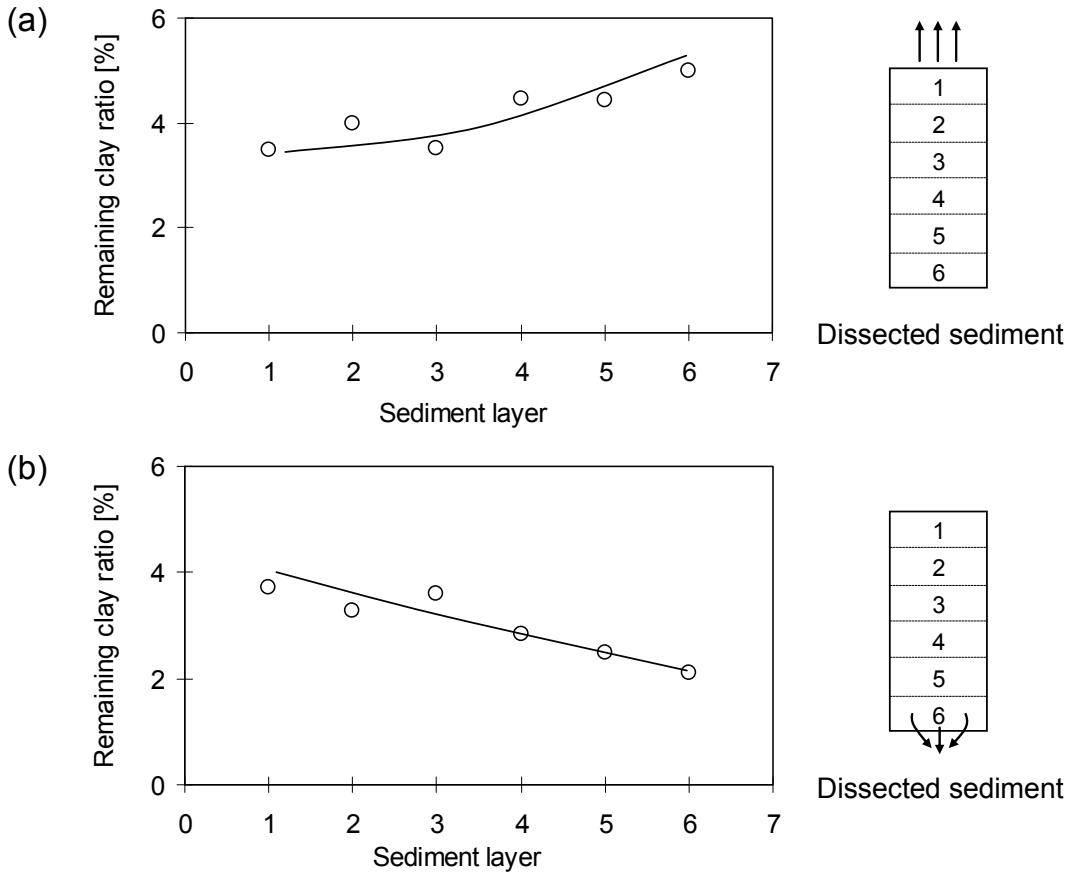

Figure 6.4. Fines migration during hydrate dissociation. (a) Fines migration during upwards flow (Test #3). (b) Fines migration due to drainage through the bottom port (Test #4).

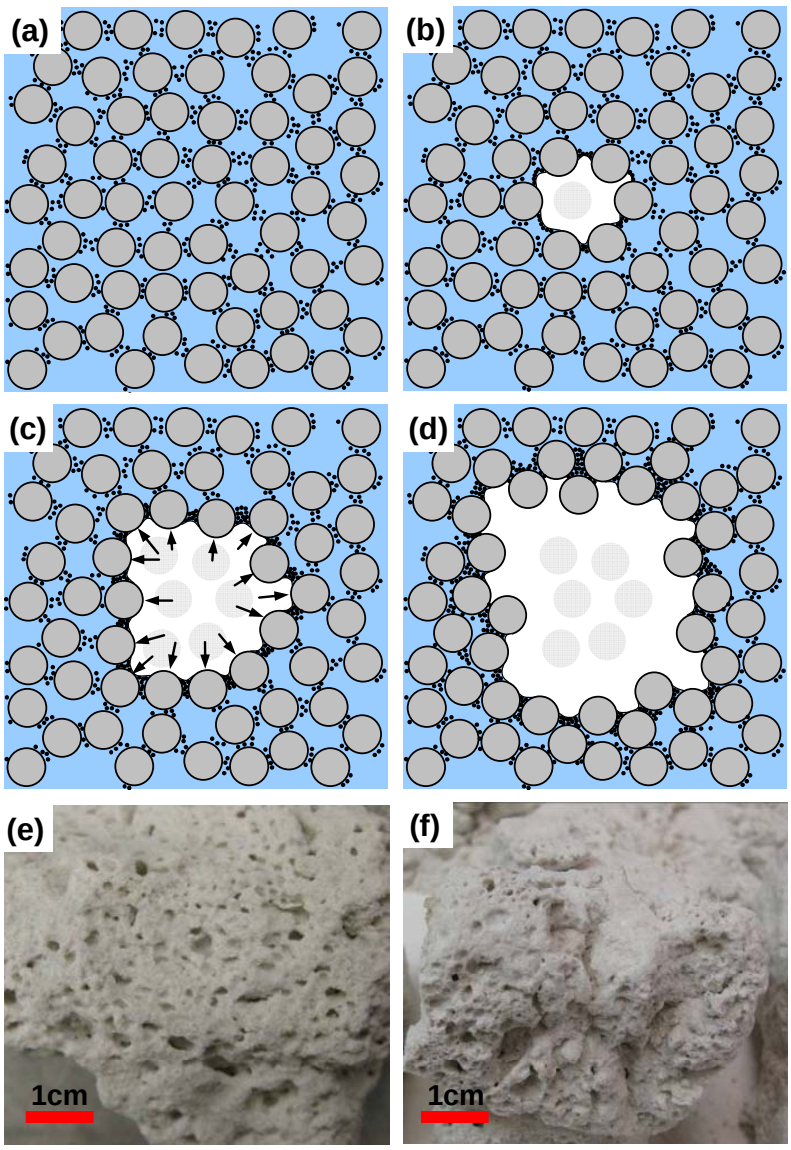

Figure 6.5. Vuggy structure formation due to local clogging and particle displacement during gas bubble expansion (Text #3). (a) Distributed fines in a water-saturated sediment. (b) Gas bubble nucleation during hydrate dissociation: fines move with the gas-water interface as the gas bubble grows. (c) High fines concentration clogs pore throats. (d) Further gas bubble growth can push sand particles away. (e and f) Observed vuggy sediment structure.

6.4.4 Vuggy structure formation

The ratio D/d ~20 for Ottawa 80/140 and kaolinite mixtures also suggests that a high concentration of kaolin particles may lead to bridge formation and sediment clogging.

Let's consider a growing gas bubble in water-saturated sandy sediment with clay fines (Figure 6.5). The fine particles that are not part of the load-carrying granular skeleton move along with the interface of the expanding bubble surface due to capillary effects. The bubble can grow without displacing the skeletal sand particles when the fines content on the bubble surface is low (Figure 6.5a). If the mass of fines per unit surface area of the bubble is high enough to form bridges and clog pore throats in the sand (Figure 6.5b), then the expanding gas bubble will locally push away the skeletal sand particles as long as the pressure of the gas bubble can create a sufficiently high force against the boundary sand grains (Figure 6.5c). This sequence of events explains the vuggy structure (similar to a sponge structure) observed after depressurization in Test # 3 (Figure 6.5d and pictures in Figures 6.5e and 6.5f).

Continued gas expansion can lead to gas driven fractures as observed in Figure 6.6 (Test #3). Together, these results suggest that the probability of gas-driven fracture formation will increase if fines are present in otherwise sandy sediments

6.4.5 Shear wave velocity

The shear-wave velocity of hydrate-free sediment is determined by the effective stresses in the direction of wave propagation $\sigma'_{//}$ and particle motion $\sigma'_{\perp}$. Once hydrate grows in the sediment, the shear wave velocity of hydrate-bearing sediments $V_{s\text{-}hbs}$ increases with hydrate saturation S_{hyd} [Santamarina and Ruppel, 2008],

$$V_{s\ hbs}^2 = \alpha\left(\frac{\sigma'_{//}+\sigma'_{\perp}}{2kPa}\right)^{\beta} + \left(\frac{V_h S_h^2}{n}\right)^2 \theta \qquad (6.4)$$

where V_h is the shear-wave velocity of pure hydrate, the factor θ captures the hydrate pore-habit (e.g., cementing or pore filling) and parameters α and β are extracted from tests conducted on sediments without hydrate ("α" is the shear wave velocity at 1 kPa and the exponent "β " captures the sensitivity of the velocity to the state of stress). This expression can be used to analyze geophysical data, such as the time series presented in Figure 6.3.

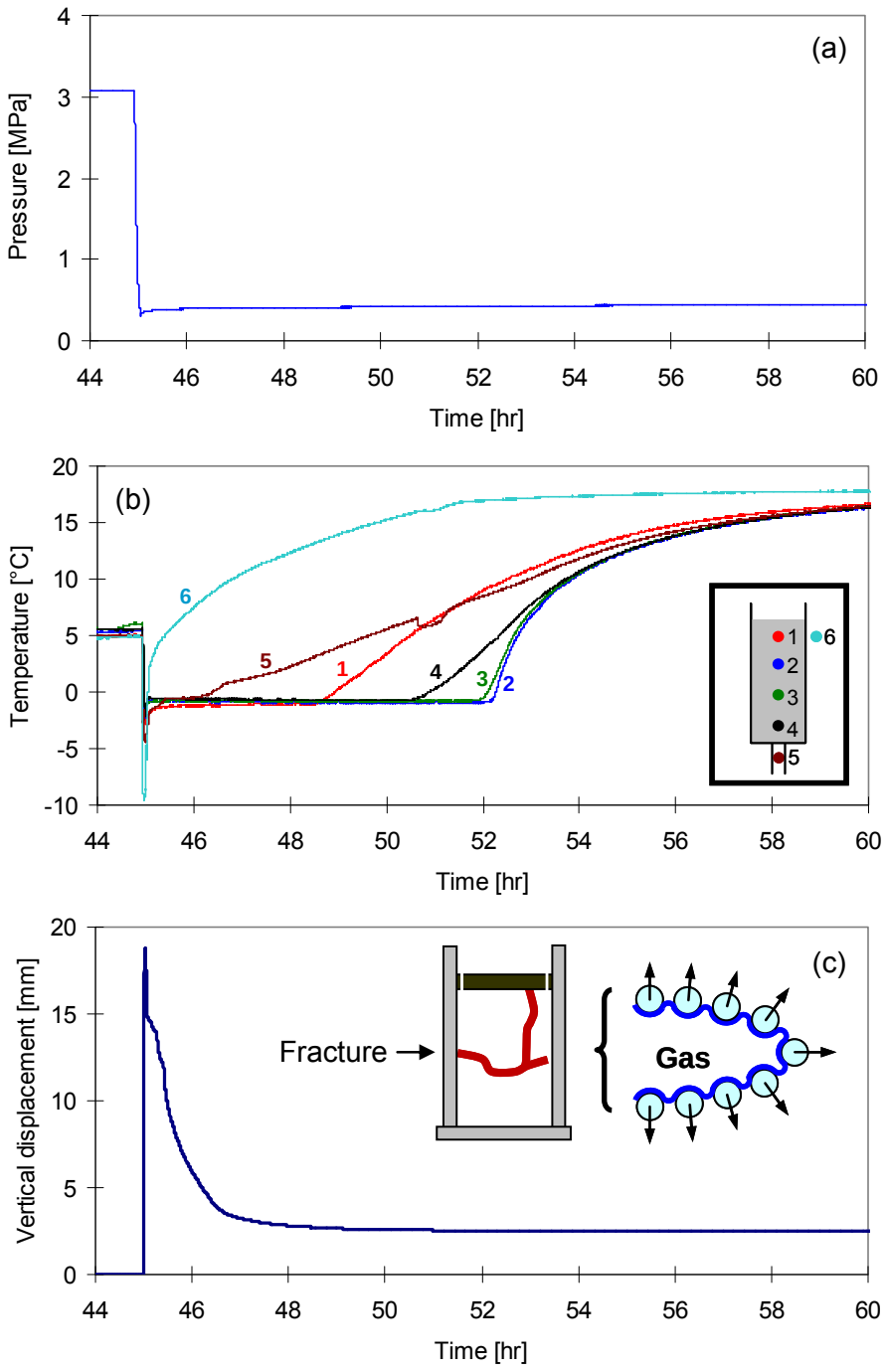

Figure 6.6. Gas driven fracture formation (Text #3). (a) Hydrate dissociation by SPS depressurization (i.e., decrease in the boundary total stress). (b) Rapid depressurization induces ice formation concurrent with hydrate dissociation. (c) Gas expansion creates gas-driven fracture formation that facilitates gas evacuation.

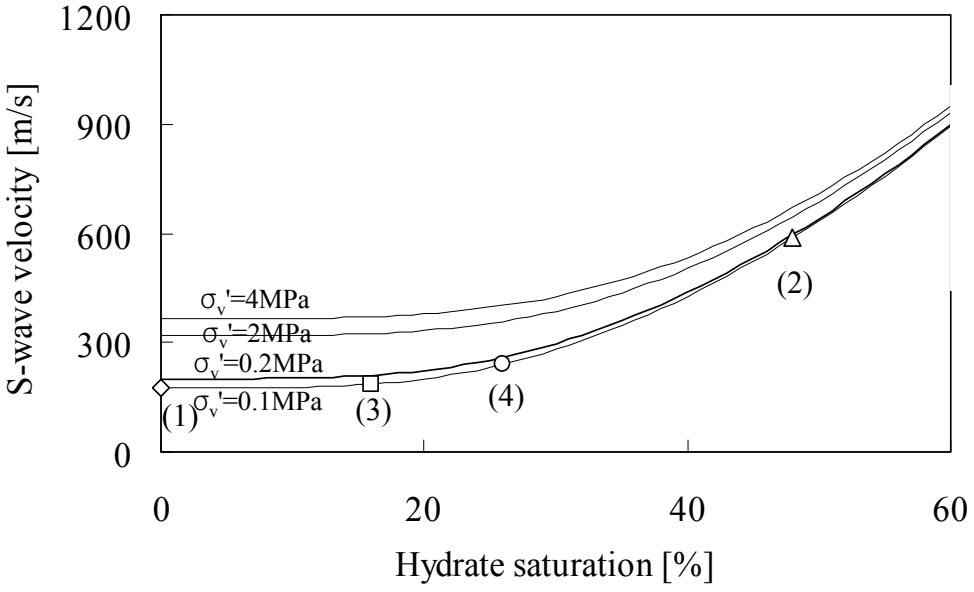

Figure 6.7. Shear wave velocity in hydrate-bearing sediments. Trends shown are for sands (Equation 6.3). Experimental results correspond to Test #3: (1) ◊ No hydrate – before hydrate formation or after hydrate dissociation. (2) Δ After initial hydrate formation. (3) □ Drop due to hydrate dissolution after gas-free water injection. (4) ○ Hydrate re-growth after water drainage and gas invasion.

Figure 6.7 shows the variation of S-wave velocity versus hydrate saturation, for different effective stress levels. Parameters α=80m/s, β=0.25 are selected for sand [Santamarina et al., 2001], V_h=1963.6 m/s [Sloan and Koh, 2008], and θ = 0.246 (typical range of θ is 0.08-to-0.25 suggested by Santamarina and Ruppel, 2008) is obtained using S-wave velocity V_s=588m/s measured at S_h=48-64% (based on pressure drop and initial water saturation) in Test #3. Using this plot, one can estimate the hydrate saturation during experiments from the measured S-wave velocities. For example, consider Test # 3: if the hydrate saturation after initial hydrate formation was S_h=48%, dissolution near the entry port caused a drop in hydrate saturation to S_h=16%, and hydrate re-grew after drainage and gas invasion to reach S_h=27% (Figure 6.7).

6.5 Conclusions

The induction time for hydrate formation in quiescent laboratory experiments can exceed weeks. Fluid flow, such as water injection into water-limited sediments or gas invasion into water-saturated sediments, triggers hydrate nucleation.

The advection of gas-free water into hydrate-bearing sediments dissolves hydrate. The change in hydrate saturation ΔS_h for each pore volume of replaced water can be estimated as a function of the water saturation S_w. It is found that $\Delta S_h \approx 0.12 S_w$ in CO_2 hydrate and $\Delta S_h \approx 0.008 S_w$ in CH_4 hydrate.

The evolution of the shear-wave velocity provides insightful information related to the sediment stress–hydrate history. The hydrate saturation can be obtained from the measured S-wave velocities using properly calibrated semi-empirical relationships that account for effective stress, porosity, and hydrate pore habit.

The migration of fine particles that are not part of the load-carrying granular skeleton depends on geometric constraints such as the relative size of the migratory fines with respect to the size of pore throats in the sediment. When the geometric conditions are satisfied, gas production in hydrate-bearing sediments containing fines can induce fines migration and lead to clogging.

A gas bubble growing in a water-saturated sediment experiences an increase in fines content on the bubble surface. Eventually, the fines content per unit surface area of the bubble can be high enough to clog pore throats. Thus, the presence of fines in otherwise clean sands will hinder gas recovery.

The expanding gas bubble may push away the skeletal particles, creating a vuggy structure. Vugs are precursors to gas-driven fracture formation.

CHAPTER 7

CONCLUSIONS

This study investigated the effects of pore-scale properties and phenomena on gas production from hydrate bearing sediments, including the effect of pore size distribution on hydraulic conductivity, the effect of gas generation methods on the soil water characteristic curves, the evolution of relative permeabilities with unsaturation, and the physical properties relevant to hydrate formation and dissociation. In addition, gas recovery efficiency and emergent phenomena during gas production were analyzed. Two types of network models (tube-network and pore-network) allowed upscaling pore-scale properties in order simulate macro-scale sediment behavior. New high pressure chambers, micromodels, and effective stress cells were developed and used to make unprecedented observations of complex hydrate-related processes in sediments. Salient conclusions follow.

Hydraulic conductivity in spatially varying media.

- In most cases, hydraulic conductivity decreases as the variance in pore size increases because flow becomes gradually localized along fewer flow paths. As few as 10 percent of the pores may be responsible for 50 percent of the total flow in sediments with high pore-size variability.
- Spatial correlation reduces the probability that small pores will plug highly conductive flow paths. Spatially correlated networks show a higher focused channeling of fluid flow than uncorrelated networks with the same pore size distribution**.** Hydraulic conductivity increases with increased correlation length.
- The hydraulic conductivity in anisotropic uncorrelated pore networks is bounded by the two extreme ‘parallel-of-series’ and ‘series-of-parallel’ tube configurations.

Anisotropic correlated networks show increased hydraulic conductivity with an increasing correlation length parallel to the flow direction.

Evolution of gas saturation during gas invasion and gas nucleation and implications on relative permeability.

- The topology of gas distributions during gas invasion and gas nucleation are fundamentally different: Invading gas forms a percolating path, while nucleating gas forms isolated gas-filled lacunae.
- Tube-network model simulation results show that the soil water characteristic curve and relative water permeability are similar for both gas invasion and nucleation. However, gas permeability is lower for gas nucleation than it is for gas invasion because some of the gas-filled tubes remain isolated without contributing to the global gas conductivity.
- Existing relative permeability equations can be used to simulate gas production in hydrate bearing sediments. However, special attention must be devoted to determine appropriate parameters for relative gas permeability as a function of saturation.

Pore-scale observations and analytical studies.

- The solubility of hydrate-forming gas in water in the presence or absence of hydrate affects hydrate formation and dissolution. Solubility changes associated with temperature changes within the hydrate stability zone and the presence/absence of a hydrate phase can trigger oscillating hydrate formation and dissolution cycles during early stage of hydrate formation. Dissolved gas in the pore water of fine grained sediments can be used to form hydrate lenses. The methane hydrate lens density can reach 4/1000.
- Gas-water interfacial tension is pressure dependent. The contact angle changes as interfacial tension changes. The fluid displacement pattern under mixed fluid flow conditions is affected by interfacial tension, contact angle, viscosity, and flow rate.

The viscosity difference between gas-water or liquid CO_2-water systems can cause viscous fingering. This will affect the efficiency of CH_4-CO_2 replacement, or the injection of liquid CO_2 for geological storage.

- The hydrate phase boundary is affected by pore size, salinity, and gas mixtures. Small pores and salts in water lower the activity of water, which shifts the phase boundary to lower temperature and higher pressure conditions. Methane and carbon dioxide gas mixtures have intermediate phase boundaries between the boundaries for pure methane and pure carbon dioxide hydrates, depending on the mass ratio of each component in the mixture. These complex conditions are found in in-situ hydrate reservoirs, they determine the lower bound of the hydrate stability zone, and affect gas recovery.
- The energy needed to dissociate hydrate is equivalent to the energy needed to increase the temperature of water up to $\Delta T \approx 96°C$. Hydrate in a sediment with porosity n=0.4 can be dissociated without causing ice formation when the initial hydrate saturation is lower than S_h=0.09 (for T_i=5°C) to S_h=0.32 (for T_i=20°C). Hydrate dissociation in sediments with high hydrate saturations from S_h~0.78 (for T_i=5°C) to S_h~0.94 (for T_i=20°C) requires all water to convert into ice in order to supply the energy needed for dissociation.

Recoverable gas from hydrate bearing sediments.

- Hydrate distribution and saturation in sediments are determined by pore size distribution, connectivity, and spatial variability. These sediment characteristics also affect recoverable gas, the evolution of gas saturation, and the internal sediment stability during production.
- There is a pronounced hydrate-to-fluid volume expansion during hydrate dissociation. The volume expansion upon hydrate dissociation is a function of pressure and temperature.

- Pore-network model simulations show that the recoverable gas increases with gas expansion and initial hydrate saturation. The gas recovery efficiency is very low, even under a high expansion condition where the initial hydrate saturation is less than S_h=5%.
- The pore size effect on the gas recovery efficiency vanishes when the mean pore size is larger than $\mu(R_p)$=1μm. If the mean pore size is smaller than $\mu(R_p)$=1μm, high capillary pressures at the pore throats inhibit gas expansion, which can cause gas-driven fractures in sediments.

Emergent phenomena during gas production from hydrate-bearing sediments.

- Water injection into water-limited sediments triggers hydrate nucleation. Conversely, gas-free water advection in water-saturated hydrate-bearing sediments dissolves hydrates.
- The presence of fines in clean sands can lead to fines migration and clogging. During dissociation, gas bubbles grow and displace fines. The fines content on the bubble surface gradually increases, and fines eventually clog the pore throats. Therefore, the expanding gas bubble may push away the skeletal particles, creating a vuggy structure. This is a precursor for gas-driven fracture formation.
- The evolution of the shear wave velocity provides insightful information related to the sediment stress-hydrate history. The hydrate saturation can be obtained with the measured S-wave velocities using semi-empirical relationships.

REFERENCES

Acharya, R.C., van der Zee, S.E.A.T.M., and Leijnse, A. (2004), Porosity-permeability properties generated with a new 2-parameter 3D hydraulic pore-network model for consolidated and unconsolidated porous media, *Advances in water resources*, 27, 707-723.

Adamson, A.W. and Gast, A.P. (1997), *Physical chemistry of surfaces* 6th Ed., New York: Wiley.

Ahmadi, G., Ji, C., Smith, D.H. (2004), Numerical solution for natural gas production from methane hydrate dissociation, *Journal of petroleum science and engineering*, 41(4), 269-285.

Albrecht, K.A., Logsdon, S.D., Parker, J.C., and Baker, J.C. (1985), Spatial variability of hydraulic properties in the emporia series, *Soil science society of America journal*, 49, 1498-1502.

Al-Futaisi, A. and Patzek, T.W. (2003), Extension of Hoshen-Kopelman algorithm to non-lattice environments, *Physica A*, 321, 665-678.

Al-Kharusi, A.S. and Blunt, M.J. (2007), Network extraction from sandstone and carbonate pore space images, *Journal of petroleum science and engineering*, 56, 219-231.

Al-Kharusi, A.S. and Blunt, M.J. (2008), Multiphase flow predictions from carbonate pore space images using extracted network models, *Water resources research*, 44, W06S01, doi:10.1029/2006WR005695.

Al-Raoush, R.I., Willson, C.S. (2005), Extraction of physically realistic pore network properties from three-dimensional synchrotron X-ray microtomography images of unconsolidated porous media systems, *Journal of Hydrology*, 300, 44-64.

Anderson, B.J., Kurihara, M., White, M.D., Moridis, G.J., Wilson, S.J., Pooladi-Darvish, M., Gaddipati, M., Masuda, Y., Collett, T.S., Hunter, R.B., Narita, H., Rose, K., and Boswell, R. (2011), Regional long-term production modeling from a single well test, Mount Elbert gas hydrate stratigraphic test well, Alaska North slope, *Marine and petroleum geology*, 28(2), 493-501.

Anderson, R., Llamedo, M., Tohidi, B., and Burgass, R.W. (2003), Experimental measurement of methane and carbon dioxide clathrate hydrate equilibria in mesoporous silica, *Journal of physical chemistry B*, 107, 3507-3514.

ASTM D6836-02 (Reapproved 2008), Standard test methods for determination of the soil water characteristic curve for desorption using hanging column, pressure extractor, chilled mirror hydrometer, or centrifuge.

Balhoff, M.T., Thompson, K.E., and Hjortsø, M. (2007), Coupling pore-scale networks to continuum-scale models of porous media, *Computer & Geosciences*, 33, 393-410.

Benson, C. (1993), Probability distributions for hydraulic conductivity of compacted soil liners, *Journal of geotechnical engineering*, 119(3), 471-486.

Benson, C. and Daniel, D. (1994), Minimum thickness of compacted soil liners: II. Analysis and case histories, *Journal of geotechnical engineering*, 120(1), 153-172.

Bernabé, Y. and Bruderer, C. (1998), Effect of the variance of pore size distribution on the transport properties of heterogeneous networks, *Journal of geophysical research*, 103, B1, 513-525.

Bhatt, D., Newman, J., and Radke, C.J. (2004), Molecular dynamics simulations of surface tensions of aqueous electrolytic solutions, *Journal of physical chemistry B*, 108, 9077-9084.

Bjerg, P.L., Hinsby, K., Christensen, T.H., and Gravesen, P. (1992), Spatial variability of hydraulic conductivity of an unconfined sandy aquifer determined by a mini slug test, *Journal of hydrology*, 135, 107-122.

Blunt, M.J. (2001), Flow in porous media – pore-network models and multiphase flow, *Current opinion in colloid & interface science*, 6(3), 197-207.

Boswell, R. and Collett, T. (2006), The gas hydrate resource pyramid, DOE Fire in the ice, Fall 2006, 5-7.

Boswell, R. and Collett, T. (2011), Current perspectives on gas hydrate resources, Energy & environmental science, 4, 1206-1215.

Boswell, R., Shelander, D., Lee, M., Latham, T., Collett, T., Guerin, G., Moridis, G., Reagan, M., and Goldberg, D. (2009), Occurrence of gas hydrate in Oligocene Frio sand: Alaminos Canyon Block 818: Northen Gulf of Mexico, *Marine and petroleum geology*, 26(8), 1499-1512.

Brooks, R.H. and Corey, A.T. (1964), Hydraulic properties of porous medium, *Hydrology paper oo.3*, Civil engineering department, Colorado state university, Fort Collins, Colorado.

Bruderer, C. and Bernabé, Y. (2001), Network modeling of dispersion: Transition from Taylor dispersion in homogeneous networks to mechanical dispersion in very heterogeneous ones, *Water resources research*, 37(4), 897-908.

Bruderer-Weng, C., Cowie, P., Bernabé, Y., and Main, I. (2004), Relating flow channelling to tracer dispersion in heterogeneous networks, *Advances in water resources*, 27, 843-855.

Bryant, S.L., Mellor, D.W., and Cade, C.A. (1993), Physically representative network models of transport in porous media, *American institute of chemical engineers journal*, 39(3), 387-396.

Butt, H.-J., Graf, K., and Kappl, M. (2006), *Physics and chemistry of interface* 2nd Ed., Weinheim: Wiley-VCH Verlag GmbH & Co. KGaA.

Cassel, D.K. (1983), Spatial and temporal variability of soil physical properties following tillage of Norfolk loamy sand, *Soil science society of America journal*, 47, 196-201.

Chun, B.-S. and Wilkinson, G.T. (1995), Interfacial tension in high-pressure carbon dioxide mixtures, *Industrial & engineering chemistry research*, 34, 4371-4377.

Cole, W.A. and Goodwin, S.P. (1990), Flash calculations for gas hydrates: a rigorous approach. *Chemical engineering science*, 45(3), 569-573.

Corey, A.T. (1954), The interrelation between gas and oil relative permeabilities, *Producers monthly*, 19(1), 38~41.

Dagan, G. (1979), Models of groundwater flow in statistically homogeneous porous formations, *Water resources research*, 15(1), 47-63.

da Rocha, S.R.P., Johnston, K.P., Westacott, R.E., and Rossky, P.J. (2001), Molecular structure of the water–supercritical CO_2 interface, *Journal of physical chemistry B*, 105, 12092-12104.

David, C. (1993), Geometry of flow paths for fluid transport in rocks, *Journal of geophysical research*, 98, 267-278.

Davie, M.K., Zatsepina, O.Y., and Buffett, B.A. (2004), Methane solubility in marine hydrate environments, *Marine geology*, 230, 177-184.

Degroot, D.J. (1996), Analyzing spatial variability of in situ soil properties, Uncertainty in the geologic environment, from theory to practice, *Proceedings of uncertainty '96, Geotechnical special publication No. 58*, Madison, Wisconsin, 210-238.

Dickens, G.R. and Quinby-Hunt, M.S. (1997), Methane hydrate stability in pore water: A simple theoretical approach for geophysical applications, *Journal of geophysical research*, 102(B1), 773-783.

Ditmars, J.D., Baecher, G.B., Edgar, D.E., and Dowding, C.H. (1988), Radioactive waste isolation in salt: a method for evaluating the effectiveness of site characterization measurements, Final report ANL/EES-TM-342, Argonne National Laboratory.

Dong, H. and Blunt, M. (2009), Pore-network extraction from micro-computerized-tomography images, *Physical review E*, 80, 036307.

Duan, Z. and Mao, S. (2006), A thermodynamic model for calculating methane solubility, density and gas phase composition of methane-bearing aqueous fluids form 273 to 523K and from 1 to 2000bar, *Geochimica et Cosmochimica Acta*, 70, 3369-3386.

Duan, Z. and Sun, R. (2003), An improved model calculating CO_2 solubility in pure water and aqueous NaCl solutions from 273 to 533K and from 0 to 2000bar, *Chemical geology*, 193, 257-271.

Duffera, M., White, J.G., and Weisz, R. (2007), Spatial variability of southeastern U.S. coastal plain soil physical properties: implications for site-specific management, *Geoderma*, 137, 327-339.

Dvorkin, J., Helgerud, M.B., Waite, W.F., Kirby, S.H., and Nur, A. (2000), Introduction to physical properties and elasticity models, in *Natural gas hydrate: In oceanic and permafrost environments*, edited by M.D. Max, pp. 245-260, Kluwer Acad., Dordrecht, Netherlands.

Egermann, P. and Vizika, O. (2001), A new method to determine critical gas saturation and relative permeability during depressurization in the near-wellbore region, *Petrophysics*, 42(4), 352-361.

Engineering ToolBox (Material properties, available at http://www.engineeringtoolbox.com)

Espinoza, D.N. and Santamarina, J.C. (2010), Water-CO_2-mineral systems: interfacial tension, contact angle and diffusion–Implications to CO_2 geological storage, *Water resources research*, 46, W07537, doi.10.1029/2009WR008634.

Fatt, I. (1956a), The network model of porous media, I. Capillary pressure characteristics, *Trans. Am. Inst. Min. Metall. Pet. Eng.*, 207, 144-159.

Fatt, I. (1956b), The network model of porous media, II. Dynamic properties of a single size tube network. *Trans. Am. Inst. Min. Metall. Pet. Eng*., 207, 160-163.

Fatt, I. (1956c), The network model of porous media, III. Dynamic properties of networks with tube radius distribution, *Trans. Am. Inst. Min. Metall. Pet. Eng*., 207, 164-177.

Francisca, F.M. and Arduino, P. (2007), Immiscible displacement model for anisotropic and correlated porous media, *International journal of geomechancis*, 7, 311-317.

Fredd, C.N. and Fogler, H.S. (1998), Influence of transport and reaction on wormhole formation in porous media, *American institute of chemical engineers journal*, 44(9), 1933-1949.

Fredlund, D.G. (2002), Use of the soil-water characteristic curve in the implementation of unsaturated soil mechanics, *Proceedings of third international conference on unsaturated soils*, Recife, Brazil, March, 887-902.

Fredlund, D.G. and Xing, A. (1994), Equations for the soil-water characteristic curve, *Canadian geotechnical engineering*, 31, 521-532.

Freeze, R.A. (1975), A stochastic-conceptual analysis of one-dimensional groundwater flow in nonuniform homogeneous media, *Water resources research*, 11(5), 725-741.

Gamwo, I.K. and Liu, Y. (2010), Mathematical modeling and numerical simulation of methane production in a hydrate reservoir, *Industrial & engineering chemistry research*, 49, 5231-5245.

Garg, S.K., Pritchett, J.W., Katoh, A., Baba, K., and Fujii, T. (2008), A mathematical model for the formation/dissociation of methane hydrates in the marine environment, *Journal of Geophysical Research*, 113, B01201.

Geistlinger, H., Krauss, G., Lazik, D., and Luckner, L. (2006), Direct gas injection into saturated glass beads: Transition from incoherent to coherent gas flow pattern, *Water resources research*, 42, W07403.

Grattoni, C.A., Hawes, R.I., and Dawe, R.A. (1998), Relative permeablities for the production of solution gas from waterflooded residual oil, SCA-9817, *International symposium of the society of core analysts*, 14-16, Sep., The Hague.

Griffiths, D.V. and Fenton, G.A. (1993), Seepage beneath water retaining structures founded on spatially random soil, *Géotechnique*, 43(4), 577-587.

Griffiths, D.V. and Fenton, G.A. (1997), Three-dimensional seepage through spatially random soil, *Journal of geotechnical and geoenvironmental engineering*, 123(2), 153-160.

Griffiths, D.V., Paice, G.M., and Fenton, G.A. (1994), Finite element modeling of seepage beneath a sheet pile wall in spatially random soil, in *Computer methods and advances in geomechanics*, pp. 1205-1209, eds, Siriwardane, H.J. and Zaman, M.M., Balkema, Rotterdam.

Guimaraes, M.S., Valdes, J.R., Palomino, A.M., and Santamarina, J.C. (2007), Aggregate production: Fines generation during rock crushing, *International journal of mineral processing*, 81, 237-247.

Gupta, A. (2007), Methane hydrate dissociation measurements and modeling: The role of heat transfer and reaction kinetics, *Ph.D. thesis*, Colorado School of Mines.

Gutjahr, A., Gelhar, L.W., Bakr, A.A., and MacMillan, J.R. (1978) Stochastic analysis of spatial variability in subsurface flows 2. Evaluation and application, *Water resources research*, 14(5), 953-959.

Handa, Y.P. (1986), Compositions, enthalpies of dissociation, and heat capacities in the range 85 to 270 K for clathrate hydrates of methane, ethane, and propane, and enthalpy of dissociation of isobutene hydrates, as determined by a heat-flow calorimeter, *Journal of chemical thermodynamics*, 18, 915-921.

Handa, Y.P., Hawkins, R.E., and Murray, J.J. (1984), Calibration and testing of a Tian-Calvet heat-flow calorimeter enthalpies of fusion and heat capacities for ice and tetrahydrofuran hydrate in the range 85 to 270K, *Journal of chemical thermodynamics*, 16, 623-632.

Handa, Y.P. and Stupin, D. (1992), Thermodynamic properties and dissociation characteristics of methane and propane hydrates in 70-Å-radius silica gel pores, *Journal of physical chemistry*, 96, 8599-8603.

Hashin, Z. and Shtrikman, S. (1962), A variational approach to the theory of the effective magnetic permeability of multiphase materials, *Journal of applied physics*, 33(10), 3125-3131.

Hillel, D. (1980), Fundamentals of soil physics, Academic, San Diego.

Hillig, W.B. (1998), Measurement of interfacial free energy for ice/water system, *Journal of crystal growth*, 183, 463-468.

Hoefner, M.L. and Fogler, H.S. (1988), Pore evolution and channel formation during flow and reaction in porous media, *American institute of chemical engineers journal*, 34(1), 45-54.

Hoeksema, R.J. and Kitanidis, P.K. (1985), Analysis of the spatial structure of properties of selected aquifers, *Water resources research*, 21(4), 563-572.

Hong, H. and Pooladi-Darvish, M. (2003), A numerical study on gas production from formations containing gas hydrates, *Canadian international petroleum conference-54th Annual technical meeting*, June 10-12, Calgary, Canada.

Hoshen, J. and Kopelman, R. (1976), Percolation and cluster distribution. I. Cluster multiple labeling technique and critical concentration algorithm, *Physical Review B*, 14(8), 3438-3445.

Hurter, S., Labregere, D., Berge, J., and Desitter, A. (2008), Impact of mutual solubility of H_2O and CO_2 on injection operations for geological storage of CO_2, 15th *International conference on the properties of water and steam*, Berlin, Sep. 8-11.

HYDRAFACT (2011), http://www.hydrafact.com/index.html.

Jang, J., Narsilio, G.A., and Santamarina, J.C. (2011), Hydraulic conductivity in spatially varying media – a pore-scale investigation, *Geophysical journal international*, 184, 1167-1179.

Jin, S., Nagao, J., Takeya, S., Jin, Y., Hayashi, J., Kamata, Y., Ebinuma, T., and Narita, H. (2006), Structural investigation of methane hydrate sediments by microfocus X-ray computed tomography technique under high-pressure conditions, *Japanese journal of applied physics*, 45(27), L714-L716.

Johnson, A., Patil, S., and Dandekar, A. (2011), Experimental investigation of gas-water relative permeability for gas-hydrate-bearing sediments from the Mount Elbert gas hydrate stratigraphic test well, Alaska north slope, *Marine and petroleum geology*, 28, 419-426.

Jung, J.W. (2010), Gas production from hydrate-bearing sediments: Geo-mechanical implications, *Ph.D. thesis*, Georgia Institute of Technology, Atlanta.

Jung, J.W., Espinoza, D.N., and Santamarina, J.C. (2010), Properties and phenomena relevant to CH_4-CO_2 replacement in hydrate-bearing sediments, *Journal of geophysical research*, 115, B10102, doi:10.1029/2009JB000812.

Kamath, J. and Boyer, R.E. (1995), Critical gas saturation and supersaturation in low permeability rock, *SPE Formation evaluation*, 10(4), 247-253.

Kampel, G, Goldsztein, G.H., and Santamarina, J.C. (2008), Plugging of porous media and filters: Maximum clogged porosity, *Applied physics letters*, 92, 084101:1~3.

Kang, Q., Tsimpanogiannis, I.N., Zhang, D., and Lichtner, P.C. (2005) Numerical modeling of pore-scale phenomena during CO_2 sequestration in oceanic sediments, *Fuel processing technology*, 86, 1647-1665.

Kang, S.P. and Lee, H. (2001), Enthalpies of dissociation of clathrate hydrates of carbon dioxide, nitrogen, (carbon dioxide_nitrogen), and (carbon dioxide+nitrogen+tetrhydrofuran), Journal of chemical thermidynamics, 33, 513-521.

Katsuki, D., Ohmura, R., Ebinuma, T., and Narita, H. (2006), Formation, growth and ageing of clathrate hydrate crystals in a porous medium, *Philosophical magazine*, 86(12), 1753-1761.

Katsuki, D., Ohmura, R., Ebinuma, T., and Narita, H. (2007), Methane hydrate crystal growth in a porous medium filled with methane-saturated liquid water, *Philosophical magazine*, 87(7), 1057-1069.

Katsuki, D., Ohmura, R., Ebinuma, T., and Narita, H. (2008), Visual observation of dissociation of methane hydrate crystals in a glass micro model: Production and transfer of methane, *Journal of applied physics*, 104, 083514.

Kawamura, T., Ohtake, M., Sakamoto, Y., Yamamoto, Y., Haneda, H., Komai, T., and Higuchi, S. (2009), Gas recovery from gas hydrate bearing sediments by inhibitor or steam injection combined with depressurization, *International offshore and polar engineering conference,* Osaka, Japan, Jun. 21-26.

Kerkar, P., Jones, K.W., Klineberg, R., Lindquist, W.B., Tomov, S., Feng, H., and Mahajan, D. (2009), Direct observations of three dimensional growth of hydrates hosted in porous media, *Applied physics letters*, 95, 024102.

Kida, M., Hachikubo, A., Sakagami, H., Minami, H., Krylov, A., Yamashita, S., Takahashi, N., Shoji, H., Khlystov, O., Poort, J., and Narita, H. (2009)a, Natural gas hydrates with locally different cage occupancies and hydrate numbers in Lake Baikal, *Geochemistry Geophysics Geosystems*, 10(5), Q05003, doi:10.1029/2009GC002473

Kida, M., Suzuki, K., Kawamura, T., Oyama, H., Nagao, J., Ebinuma, T., Narita, H., Suzuki, H., Sakagami, H., and Takahashi, N. (2009)b, Characteristics of natural gas hydrates occurring in pore-spaces of marine sediments collected from the eastern Nankai trough, off Japan, *Energy & Fuels*, 23, 5580-5586.

Kihara, T. (1953), Virial coefficient and models of molecules in gases, *Reviews of modern physics* , 25(4), 831-843.

Kim, D.-Y., Uhm, T.-W., Lee, H., Lee, Y.-J., Ryu, B.-J., and Kim, J.-H. (2005), Compositional and structural identification of natural gas hydrates collected at site 1249 on Ocean Drilling Program Leg 204, *Korean Journal of Chemical Engineering*, 22(4), 569-572.

Kim, H. and Burgess, D. (2001), Prediction of interfacial tension between oil mixtures and water, *Journal of colloid and interface science,* 241, 509-513.

Kleinberg, R.L., Flaum, C., Griffin, D.D., Brewer, P.G., Malby, G.E., Peltzer, E.T., and Yesinowski, J.P. (2003), Deep sea NMR: Methane hydrate growth habit in porous media and its relationship to hydraulic permeability, deposit accumulation, and submarine slope stability, *Journal of geophysical research*, 108(10), 2508, doi:10.1029/2003JB002389.

Knight, C.A. (1971), Experiments on the contact angle of water on ice, *Philosophical magazine,* 23, 153-165.

Koh, C.A., Sum, A.K., and Sloan, E.D. (2009), Gas hydrates: Unlocking the energy from icy cages, *Journal of applied physics*, 106, 0611011-1~14.

Konno, Y., Masuda, Y., Hariguchi, Y., Kurihara, M., and Ouchi, H. (2010), Key factors for depressurization-induced gas production from oceanic methane hydrates, *Energy & Fuels*, 24, 1736-1744.

Kono, H.O., Narasimhan, S., Song, F., and Smith, D.H. (2002), Synthesis of methane gas hydrate in porous sediments and its dissociation by depressurizing, *Power technology*, 122, 239-246.

Kruyer, S. (1958), The penetration of mercury and capillary condensation in packed spheres, *Transactions of the Faraday society*, 54(11), 1758-1767.

Kurihara, M., Sato, A., Ouchi, H., Narita, H., Masuda, Y., Saeki, T., and Fujii, T. (2009), Prediction of gas productivity from eastern Nankai Trough methane hydrate reservoirs, *SPE Journal of reservoir evaluation & engineering*, 12, 477-499.

Kurihara, M., Sato, A., Funatsu, K., Ouchi, H., Masuda, Y., Narita, H., and Collett, T.S. (2010), Analysis of formation pressure test results in the Mount Elbert methane hydrate reservoir through numerical simulation, *Marine and petroleum geology*, in print, doi:10.1016/j.marpetgeo.2010.01.007.

Kuznetsova, T. and Kvamme, B. (2002), Thermodynamic properties and interfacial tension of a model water-carbon dioxide system, *Physical chemistry chemical physics*, 4, 937-941.

Kvamme, B., Kuznetsova, T., Hebach, A., Oberhof, A., and Lunde, E. (2007), Measurements and modelling of interfacial tension for water+carbon dioxide systems at elevated pressure, *Computational material science*, 38, 506-513.

Kwon, T.-H., Cho, G.-C., and Santamarina, J.C. (2008), Gas hydrate dissociation in sediments: Pressure-temperature evolution, *Geochemistry Geophysics Geosystems*, 9, Q03019, doi:10.1029/2007GC001920.

Lacasse, S., and Nadim, F. (1996), Uncertainties in characterizing soil properties, *Proceedings of uncertainty '96*, Geotechnical special publication No. 58, Madison, Wisconsin, 49-75.

Landau, L. D., and Lifshitz, E. M. (1960), *Electrodynamics of continuous media*, Pergamon Press, Oxford, New York.

Laudone, G.M., Matthews, G.P., and Gane, P.A.C. (2008), Modelling diffusion from simulated porous structures, *Chemical engineering science*, 63, 1987-1996.

Leaist, D.G., Murray, J.J., Post, M.L., and Davidson, D.W. (1982), Enthalpies of decomposition and heat capacities of ethylene oxide and tetrahydrofuran hydrates, *Journal of physical chemistry*, 86, 4175-4178.

Lenormand, R, Touboul, E., and Zarcone, C. (1988), Numerical models and experiments on immiscible displacements in porous media, *Journal of fluid mechanics*, 189, 165-187.

Lenormand, R. and Zarcone, C. (1985), Invasion percolation in an etched network: measurement of a fractal dimension, *Physical review letters*, 54, 2226-2229.

Leong, E.C. and Rahardjo, H. (1997), Review of soil-water characteristic curve equations, *Journal of geotechnical and geoenvironmental engineering*, 123(12), 1106-1107.

Libardi, P.L., Reichardt, K., Nielsen, D.R., and Biggar, J.W. (1980), Simple field methods for estimating soil hydraulic conductivity, *Soil science society of America journal*, 44(1), 3-7.

Lievois, J.S., Perkins, R., Martin, R.J., and Kobayashi, R. (1990), Development of an automated, high pressure heat flux calorimeter and its application to measure the heat of dissociation and hydrate numbers of methane hydrate, *Fluid phase equilibria*, 59, 73-97.

Lindquist, W.B., Venkatarangan, A., Dunsmuir, J., Wong, T. (2000), Pore and throat size distributions measured from synchrotron X-ray tomographic images of Fontainebleau sandstones, *Journal of geophysical research*, 105, B9, 21509-21527.

Linga, P., Haligva, C., Nam, S.C., Ripmeester, J.A., and Englezos, P. (2009), Gas hydrate formation in a variable volume bed of silica sand particles, *Energy & Fuels*, 23, 5496-5507.

Linga, P., Haligva, C., Nam, S.C., Ripmeester, J.A., and Englezon, P. (2009), Recovery of methane from hydrate formed in a variable volume bed of silica sand particles, *Energy & Fuels*, 23, 5508-5516.

Lu, H., Moudrakovski, I., Riedel, M., Spence, G., Dutrisac, R., Ripmeester, J., Wright, F., and Dallimore, S. (2005), Occurrence and structural characterization of gas hydrates associated with a cold vent field, offshore Vancouver Island, *Journal of geophysical research*, 110, B10204, doi:10.1029/2005JB003900.

MacDonald, G.J. (1990), The future of methane as an energy resource, *Annual review of energy*, 15, 53-83.

Matheron, G. (1967), *Eléments Pour une Théorie des Milieux Poreux*, Masson, Paris.

Minagawa, H., Hirakawa, Y., Sato, M., Ohmura, R., Kamata, Y., Takeya, S., Nagao, J., Ebinuma, T., Narita, H., and Masuda, Y. (2004), Measurement of water permeability under the presence of methane hydrate, *AAPG Hedberg research conference*, Vancouver, BC, Canada, Sep. 12~16.

Minagawa, H., Nishikawa, Y., Ikeda, I., Sakamoto, Y., Komai, T., and Narita, H. (2007), Measurement of methane hydrate sediment permeability using several chemical solutions as inhibitors, *The seventh ISOPE ocean mining symposium*, Lisbon, Portugal, July 1-6.

Moridis, G.J., Kowalsky, M.B., and Pruess, K. (2007), Depressurization-induced gas production from class 1 hydrate deposits, *SPE Journal of reservoir evaluation & engineering*, 10, 458-481.

Moridis, G.J., Silpngarmlert, S., Reagan, M.T., Collett, T., and Zhang, K. (2011), Gas production from a cold, stratigraphically-bounded gas hydrate deposit at the Mount Elbert gas hydrate stratigraphic test well, Alaska North slope: Implications of uncertainties, *Marine and petroleum geology*, 28, 517-534

Moridis, G.J. and Sloan, E.D. (2007), Gas production potential of disperse low-saturation hydrate accumulations in oceanic sediments, *Energy conversion and management*, 48(6), 1834-1849.

Morrow, N.R. (1990), Wettability and its effect on oil recovery, *Journal of petroleum technology*, 42, 1476-1484.

Mu, D., Liu, Z-S., Huang, C., and Djilali, N. (2008), Determination of the effective diffusion coefficient in porous media including Knudsen effects, *Microfluid Nanofluid*, 4(3), 257-260.

Mullin, J.W. (2001), Crystallization, Butterworth-Heinemann. *London*.

Myerson, A.S. (2002), *Handbook of industrial crystallization*, Butterworth-Heinemann.

Nagayev, V.B., Gritsenko, A.I., and Murin, V.I. (1979), All-union conference on calorimetry and chemical thermodynamics, Ivonovo, Proc. 1-NOR, 58.

Narsilio, G.A., Buzzi, O., Fityus, S., Yun, T.S., and Smith, D.W. (2009), Upscaling of Navier-Stokes equations in porous media: theoretical, numerical and experimental approach, *Computers and Geotechnics*, 36(7), 1200-1206.

National Energy Technology Laboratory, US Department of Energy (2011), Energy resource potential of methane hydrate An introduction to the science and energy potential of a unique resource (http://www.netl.doe.gov/technologies/oil-gas/publications/Hydrates/2011Reports/MH_Primer2011.pdf).

National Physical Laboratory (2011), Tables of physical and chemical constants, http://www.kayelaby.npl.co.uk.

Naylor, P., Fishlock, T., Mogford, D., and Smith, R. (2000), Relative permeability measurements for post-waterflood depressurization of the Miller field, North Sea, *SPE annual technical conference and exhibition*, Dallas, Texas, October 1~4, SPE 63148, 491-497.

Nazridoust, K. and Ahmadi, G. (2007), Computational modeling of methane hydrate dissociation in a sandstone core, *Chemical engineering science*, 62, 6155-6177.

Nyre, A.N., McDougall, S.R., and Skauge, A. (2008), Effect of depressurization on trapped saturations and fluid flow functions, *SPE 16th symposium on improved oil recovery*, Tulsa, Oklahoma, U.S.A., April 19~23, SPE 113394, 697-690.

Øren, P.-E. and Bakke, S. (2003), Reconstruction of Berea sandstone and pore-scale modelling of wettability effets, *Journal of petroleum science and engineering*, 39, 177-199.

Osegovic, J.P., tatro, S.R., and Holman, S.A. (2006), Physical chemical characteristics of natural gas hydrate, in *Economic geology of natural gas hydrate*, Ed. Max, M.D., Hohnson, A.H., and Dillon, W.P.. 45~104.

Oyama, H., Konno, Y., Masuda, Y., and Narita, H. (2009), Dependence of depressurization-induced dissociation of methane hydrate bearing laboratory cores on heat transfer, *Energy & Fuels*, 23, 4995-5002.

Papamichos, E., Vardoulakis, I., Tronvoll, J., and Skjærstein, A. (2001), Volumetric sand production model and experiment, *International journal for numerical and analytical methods in geomechanics*, 25, 789-808.

Pauer, F., Kipfstuhl, s., Kuhs, W.F., and Shoji, H. (1999), Air clathrate crystals from the GRIP deep ice core, Greenland: a number-. Size- and shape-distribution study, *Journal of glaciology*, 45(149), 22-30.

Pennell, K.D., Pope, G.A., and Abriola, L.M. (1996), Influence of viscous and buoyancy forces on the mobilization of residual tetrachloroethylene during surfactant flushing, *Environmental science technology*, 30, 1328-1335.

Phadnis, H.S. and Santamarina, J.C. (2011), Pore size limited life in sediments, *Géotechnique letters*, under review.

Phelps, T.J., Peters, D.J., Marshall, S.L., West, O.R., Liang, L., Blencoe, J.G., Alexiades, V., Jacobs, G.K., Naney, M.T., and Heck Jr., J.L. (2001), A new experimental facility for investigating the formation and properties of gas hydrates under simulated seafloor conditions, *Review of scientific instruments*, 72(2), 1514-1521.

Poulsen, S., McDougall, S.R., Sorbie, K., and Skauge, A. (2001), Network modeling of internal and external gas drive, *International symposium of the society of core analysts*, Edinburgh, Sep., SCA 2001-17.

Prat, M. (2002), Recent advances in pore-scale models for drying of porous media, *Chemical engineering journal*, 86, 153-164.

Qi, R., LaForce, T.C. and Blunt M.J. (2009), A three-phase four-component streamline-based simulator to study carbon dioxide storage, *Computational Geosciences*, *13*(4), 493-509.

Reagan, M.T. and Moridis, G.J. (2007), Oceanic gas hydrate instability and dissociation under climate change scenarios, *Geophysical research letters*, 34, L22709, doi:10.1029/2007GL031671.

Reagan, M.T. and Moridis, G.J. (2008), Dynamic response of ocean hydrate deposits to ocean temperature change, *Journal of geophysical research*, 113, C12023, doi:10.1029/2008JC004938.

Reeves, P.C. and Celia, M.A. (1996), A functional relationship between capillary pressure, saturation, and interfacial area as revealed by a pore-scale network model, *Water resources research*, 32(8), 2345-2358.

Ren, Q.-Y., Chen, G.-J., Yan, W., and Guo, T.-M. (2000), Interfacial tension of (CO_2 + CH_4) + water from 298K to 373K and pressures up to 30MPa, *Journal of Chemical and Engineering Data*, 45, 610-612.

Ripmeester, J.A., Lu, H., Moudrakovski, I.L., Dutrisac, R., Wilson, L.D., Wright, F., and Dallimore, S.R. (2005), Structure and composition of gas hydrate in sediment recovered from the JAPEX/JNOC/GSC et al. Mallik 5L-38 gas hydrate production research well, determined by X-ray diffraction and Raman and solid-state nuclear magnetic resonance spectroscopy, in Scientific results from the Mallik 2002 Gas hydrate production research well program, Mackenzie Delta, Northwest territories, *Canada, Geological Survey of Canada*, Bulletin 585, 6p.

Ripmeester, J.A. and Ratcliffe, C.I. (1988), Low-temperature cross-polarization/magic angle spinning ^{13}C NMR of solid methane hydrates: Structure, cage occupancy, and hydration number, *Journal of physical chemistry*, 92(2), 337-339.

Rueff, R.M., Sloan, E.D., and Yesavage, V.F. (1988), Heat capacity and heat of dissociation of methane hydrates, AIChE Journal, 34(9), 1468-1476.

Rutqvist, J., Moridis, G.J., Grover, T., and Collett, T. (2009), Geomechanical response of permafrost-associated hydrate deposits to depressurization-induced gas production, *Journal of petroleum science and engineering*, doi:10.1016/j.petro.2009.02.013.

Sachs, W. and Meyn, V. (1995), Pressure and temperature dependence of the surface tension in the system natural gas/water Principles of Investigation and the first precise experimental data for pure methane/water at 25°C up to 46.8MPa, *Colloids and Surfaces A: Physicochemical and Engineering Aspects*, 94, 291-301.

Sahimi, M. (1994), *Applications of percolation theory*, Taylor&Francis, London, 258 pp.

Salamatin, A.N., Lipenkov, V.Y., and Hondoh, T. (2003), Air-hydrate crystal growth in polar ice, *Journal of crystal growth*, 257, 412-426.

Santamarina, J.C. and Jang, J. (2009), Gas production from hydrate bearing sediments: Geomechanical implication, NETL methane hydrate newsletter: *Fire in the ice*, 9, 18-22.

Santamarina, J.C. and Jang, J. (2010), Energy geotechnology: Implications of mixed fluid conditions, *International conference on unsaturated soils*, Sep. 6~8, Barcelona, Spain.

Santamarina, J.C. and Ruppel, C. (2008), The impact of hydrate saturation on the mechanical, electrical, and thermal properties of hydrate-bearing sand, silts, and clay, *Proceedings of 6th international conference on gas hydrates*, Vancouver, Canada, 6-10 July.

Santamarina, J.C., Klein, K.A., and Fam, M.A. (2001), *Soils and Waves*, J. Wiley & Sons, New York, 488pp.

Servio P. and Englezos, P. (2001), Effect of temperature and pressure on the solubility of carbon dioxide in water in the presence of gas hydrate, *Fluid phase equilibria*, 190, 127-134.

Servio, P. and Englezos, P. (2002), Measurement of dissolved methane in water in equilibrium with its hydrate, *Journal of chemical engineering data*, 47, 87-90.

Seo, Y., Lee, H., and Ryu, B.-J. (2002), Hydrate number and two-phase equilibria of CH_4 hydrate in the deep ocean sediments, *Geophysical research letters*, 29(8), 1244, 10.1029/2001GL014226.

Shaw, D.J. (1992), *Introduction to colloid & surface chemistry* 4th Ed., London: Butterworth-Heinemann.

Shin. H. and Santamarina, J.C. (2010), Fluid-driven fractures in uncemented sediments: Underlying particle-level process, *Earth and planetary science letters*, 299,180-189.

Sloan, E.D. and Koh, C.A. (2008), *Clathrate hydrates of natural gases* 3rd ed., CRC Press, Taylor&Francis Group, Boca Raton, Fl.

Sloan, E.D., Koh, C.A., Sum, A.K., Ballard, A.L., Shoup, G.J., McMullen, N., Creek, J.L., and Palermo, T. (2009), Hydrates: state of the art inside and outside flowlines, *Journal of petroleum technology*, December, 89-94.

Soga, K., Lee, S.L., Ng, M.Y.A., and Klar, A. (2007), Characterisation and engineering properties of methane hydrate soils, *in Characterisation and engineering properties of natural soils, Taylor&Francis Group, London*, 2591-2642.

Sok, R.M., Knackstedt, M.A., Sheppard, A.P., Pinczewski, W.V., Lindquist, W.B., Venkatarangan, A., and Paterson, L. (2002), Direct and stochastic generation of network models from tomographic images; Effect of topology on residual saturations, *Transport in Porous Media*, 46, 345-372.

Song, K.Y. and Kobayashi, R. (1987), Water content of CO2 in equilibrium with liquid water and/or hydrate, *SPE Formation evaluation*, 2, 500-508.

Span, R. and Wagner, W. (1996), A new equation of state for carbon dioxide covering the fluid region from the triple-point temperature to 1100K at pressures up to 800MPa, *Journal of physical and chemical reference data*, 25(6), 1509-1596.

Stauffer, D. and Aharony, A. (1992), *Introduction to percolation theory*, 2nd edition, Taylor&Francis, London, 181 pages.

Stewart, C.R, Hunt, E.B., Schneider, P.N., Geffen, T.M., and Berry, V.J. (1954), The role of bubble formation in oil recovery by solution gas drives in limestones, *Journal of petroleum technology*, 6(12), 21-28.

Stone, H.L. (1970), Probability model for estimating three-phase relative permeability, *Journal of petroleum technology*, 214-218.

Stryjek, R. and Vera, J.H. (1986), PRSV: An improved Peng-Robinson equation of state for pure compounds and mixture, *The Canadian journal of chemical engineering*, 64, 323-333.

Subramanian, S. and Sloan, E.D. (2002), Solubility effects on growth and dissolution of methane hydrate needles, Proceedings of 4th international conference on gas hydrates, Jpn. Natl. Oil Corp., Yokohama, Japan, 19-23 May.

Suicmez, V.S., Piri, M., and Blunt, M.J. (2008), Effects of wettability and pore-level displacement on hydrocarbon trapping, *Advances in water resources*, 31, 503-512.

Sum, A.K., Burruss, R.C., and Sloan, E.D. (1997), Measurement of clathrate hydrates via Raman spectroscopy, *Journal of physical chemistry B*, 101(38), 7371-7377.

Sun, R. and Duan, Z. (2007), An accurate model to predict the thermodynamic stability of methane hydrate and methane solubility in marine environments, *Chemical geology*, 244, 248-262.

Surasani, V.K., Metzger, T., and Tsotas, E. (2008), Consideration of heat transfer in pore network modelling of convective drying, *International journal of heat and mass transfer*, 51, 2506-2518.

Sychev, V.V., Vasserman, A.A., Zagoruchenko, V.A., Spiridonov, G.A., and Tsymarny, V.A. (1987), *Thermodynamic properties of methane*, 341 pp., Hemisphere, Washington, D.C.

Tang, L.G., Xiao, R., Huang, C., Feng, Z.P., Fan, S.S. (2005), Experimental investigation of production behavior of gas hydrate under thermal stimulation in unconsolidated sediment, *Energy & Fuels*, 19, 2402-2407.

Taskinen, A., Sirvio, H, and Bruen, M. (2008), Generation of two-dimensionally variable saturated hydraulic conductivity fields: Model theory, verification and computer program, *Computer & Geosciences*, 34, 876-890.

Tishchenko, P., Hensen, C., Wallmann, K., and Won, C.S. (2005), Calculation of the stability and solubility of methane hydrate in seawater, *Chemical geology*, 219, 37-52.

Tohidi, B., Anderson, R., Clennell, M.B., Burgass, R.W., and Biderkab, A.B. (2001), Visual observation of gas-hydrate formation and dissociation in synthetic porous media by means of glass micromodels, *Geology*, 29, 867-870.

Tohidi, B., Yang, J., Salehabadi, M., Anderson, R., and Chapoy, A. (2010), CO_2 hydrate could provide secondary safety factor in subsurface sequestration of CO_2, *Environmental science technology*, 44, 1509-1514.

Tréhu, A.M., Long, P.E., Torres, M.E., Bohrmann, G., Rack, F.R., Collett, T.S., Goldberg, D.S., Milkov, A.V., Riedel, M., Schultheiss, P., Bangs, N.L., Barr, S.R., Borowski, W.S., Claypool, G.E., Delwiche, M.E., Dickens, G.R., Gracia, E., Guerin, G., Holland, M., Johnson, J.E., Lee, Y.-J., Liu, C.-S., Su, X., Teichert, B., Tomaru, H., Vanneste, M., Watanabe, M., and Weinberger, J.L. (2004), Three-dimensional distribution of gas hydrate beneath southern Hydrate Ridge: constrains from ODP Leg 204, *Earth and planetary science letters*, 222, 845-862.

Treiber, L.E., Archer, D.L., and Owens, W.W. (1972), A laboratory evaluation of the wettability of fifty oil-producing reservoirs, *Society of petroleum engineers journal,* 12, 531-540.

Tsimpanogiannis, I.N. and Lichtner, P.C. (2003), Pore network study of methane clathrate hydrate dissociation. EOS, *Trans, Am. Geophys. Union*, 84(46) (Abstract OS51B-0848).

Tsimpanogiannis, I.N. and Lichtner, P.C. (2006), Pore-network study of methane hydrate dissociation, *Physical review E*, 74, 056303:1-13.

Uchida, T., Ebinuma, T., and Ishizaki, T. (1999), Dissociation condition measurements of methane hydrate in confined small pores of porous glass, *Journal of physical chemistry* B, 103, 3659-3662.

Uchida, T., Ebinuma, T., Takeya, s., Nagao, J., and Narita, H. (2002), Effects of pore sizes on dissociation temperatures and pressures of methane, carbon dioxide, and propane hydrates in porous media, *The journal of physical chemistry B*, 106, 820-826.

Uchida, T., Hirano, T., Ebinuma, T., Narita, H., Gohara, K., Mae, S., and Matsumoto, R. (1999), Raman spectroscopic determination of hydration number of methane hydrates, *American institute of chemical engineers journal*, 45(12), 2641-2645.

Uchida, T., Hondoh, T., Mae, S., Lipenkov. V.Y, and Duval, P. (1994), Air-hydrate crystals in deep ice-core samples from Vostok Station, Antarctica, *Journal of glaciology*, 40(134), 79-86.

Uchida, T., Lu, H., Tomaru, H., and the MITI Nankai Trough shipboard scientist (2004), Subsurface occurrence of natural gas hydrate in the Nankai Trough area: Implication for gas hydrate concentration, *Resource geology*, 54(1), 35-44.

Uchida, T. Mae, S., Hondoh, T., Duval, P., and Lipenkov. V.Ya. (1993), Measurements of surface energy of air-hydrate crystals in Vostok ice core, Antactica, *Proceedings of the National Institute of Polar Research NIPR symposium on polar meteorology and glaciology*, 7, 1-6.

Uddin, M., Coombe, D., Law, D., and Gunter, B. (2008), Numerical studies of gas hydrate formation and decomposition in a geological reservoir, *Journal of energy resources technology*, 130, 032501.

Valdes, J.R. and Santamarina, J.C. (2008), Clogging: bridge formation and vibration-based destabilization, *Canadian Geotechnical Journal*, 45, 177-184.

Valvatne, P.H. (2004), Predictive pore-scale modeling of multiphase flow, *PhD thesis*, Department of earth science and engineering, Imperial College, London.

van der Waals, J.H. and Platteeuw, J.C. (1959), Clathrate solutions, Advances in chemical physics, 2, 1-57.

van Genuchten, M.Th. (1980), A closed-form equation for predicting the hydraulic conductivity of unsaturated soils, *Soil Science Society of America Journal*, 44, 892-898.

Waite, W.F., Santamarina, J.C., Cortes, D.D., Dugan, B., Espinoza, D.N., Germain, J., Jang, J., Jung, J.W., Kneafsey, T.J., Shin, H., Soga, K., Winters, W., and Yun, T.-S. (2009), Physical properties of hydrate-bearing sediments, *Reviews of Geophysics*, 47, RG4003, doi:10.1029/2008RG00279.

Waite, W.F., Stern, L.A., Kirby, S.H., Winters, W.J., and Mason, D.H. (2007), Simultaneous determination of thermal conductivity, thermal diffusivity and specific heat in sI methane hydrate, *Geophysical journal international*, 169, 767-774.

Warren, J.E. and Price, H.S. (1961), Flow in heterogeneous porous media, *Society of petroleum engineers*, 1, 153-169.

Weast, R.C. (1987), *CRC Handbook of chemistry and physics 68^{ed}.*, CRC Press, Boca Raton, Fla.

West, O., Tsouris, C., Liang, L., Lee, S., and McCallum, S. (2003), Negatively buoyant CO_2–hydrate composite for ocean carbon sequestration, *AIChE Journal*, 49, 283-285.

Wilder, J.W., Moridis, G.J., Wilson, S.J., Kurihara, M., White, M.D., Masuda, Y., Anderson, B.J., Collett, T.S., Hunter, R.B., Narita, H., Pooladi-Darvish, M., Rose, K., and Boswell, R. (2008), An international effort to compare gas hydrate reservoir simulators, *Proceedings of the 6th International conference on gas hydrate*, July 6-10, Vancouver, Canada.

Wilhelm, E., Battino, R., and Wilcock, R.J. (1977), Low-pressure solubility of gases in liquid water, *Chemical reviews*, 77, 219-262.

Wilkinson, D. and Willemsen, J.F. (1983), Invasion percolation: a new form of percolation theory, *Journal of physics A: Mathematical and general*, 16, 3365-3376.

Wösten, J.H.M., Lilly, A., Nemes, A., and Bas, C.L. (1999), Development and use of a database of hydraulic properties of European soils, *Geoderma*, 90, 169-185.

Yortsos, Y.C. and Parlar, M. (1989). Phase change in binary systems in porous media: Application to solution-gas drive, *SPE annual technical conference and exhibition*, SPE 19697, 693-708.

Yun, T.S., Fratta, D., and Santamarina, J.C. (2010), Hydrate-bearing sediments from the Krishna-Godavari basin: Physical characterization, pressure core testing and scaled production monitoring, *Energy&Fuels*, 24, 5972-5983, doi:10.1021/ef100821t.

Zatsepina, O.Y. and Buffett, B.A. (1998), Thermodynamic conditions for the stability of gas hydrate in the seafloor, *Journal of geophysical research*, 103, 24127-24139.

References for Figure 5.1.

Blake Ridge

Collett, T.S. and Ladd, J. (2000), Detection of gas hydrate with downhole logs and assessment of gas hydrate concentrations (saturations) and gas volumes on the Blake Ridge with electrical resistivity log data. *In* Paull, C.K., Matsumoto, R., Wallace, P.J., and Dillon, W.P. (Eds.), *Proc. ODP, Sci. Results,* 164: College Station, TX (Ocean Drilling Program), 179–191. doi:10.2973/odp.proc.sr.164.219.2000

Shipboard Scientific Party, 1996. Site 994. *In* Paull, C.K., Matsumoto, R., Wallace, P.J., et al., *Proc. ODP, Init. Repts.,* 164: College Station, TX (Ocean Drilling Program), 99–174. doi:10.2973/odp.proc.ir.164.107.1996

Shipboard Scientific Party, 1996. Site 995. *In* Paull, C.K., Matsumoto, R., Wallace, P.J., et al., *Proc. ODP, Init. Repts.,* 164: College Station, TX (Ocean Drilling Program), 175–240. doi:10.2973/odp.proc.ir.164.108.1996

Shipboard Scientific Party, 1996. Site 997. *In* Paull, C.K., Matsumoto, R., Wallace, P.J., et al., *Proc. ODP, Init. Repts.,* 164: College Station, TX (Ocean Drilling Program), 277–334. doi:10.2973/odp.proc.ir.164.110.1996

Shipboard Scientific Party, 1998. Deep Blake-Bahama Outer Ridge, Sites 1060, 1061, and 1062. *In* Keigwin, L.D., Rio, D., Acton, G.D., et al., *Proc. ODP, Init. Repts.,* 172: College Station, TX (Ocean Drilling Program), 157–250. doi:10.2973/odp.proc.ir.172.105.1998

Cascadia Margin

Expedition 311 Scientists, 2006. Expedition 311 summary. *In* Riedel, M., Collett, T.S., Malone, M.J., and the Expedition 311 Scientists, *Proc. IODP,* 311: Washington, DC (Integrated Ocean Drilling Program Management International, Inc.). doi:10.2204/iodp.proc.311.101.2006

Shipboard Scientific Party, 1994. Sites 889 and 890. *In* Westbrook, G.K., Carson, B., Musgrave, R.J., et al., *Proc. ODP, Init. Repts.,* 146 (Pt. 1): College Station, TX (Ocean Drilling Program), 127–239. doi:10.2973/odp.proc.ir.146-1.008.1994

East Sea

Lee, C., Yun, T-S, Lee, J-S., Bahk, J., and Santamarina, J.C. (2010) Geotechnical characterization of marine sediments in the Ulleung basin, East sea, *Marine Geology*, Under review.

Moridis, G.J., Reagan, M.T., Kim, S.-J., Seol, Y., Zhang, K. (2009), Evaluation of the gas production potential of marine hydrate deposits in the Ulleung basin of the Korean East Sea, SPE Journal, 14(4), 759-781

Eel River Basion (California margin)

Shipboard Scientific Party, 1997. Site 1019. *In* Lyle, M., Koizumi, I., Richter, C., et al., *Proc. ODP, Init. Repts.,* 167: College Station, TX (Ocean Drilling Program), 353–387. doi:10.2973/odp.proc.ir.167.113.1997

Gulf of Mexico

McConnell, D., Boswell, R., Collett, T., Frye, M., Shedd, W., Guerin, G., Cook, A., Mrozewski, S., Dufrene, R., and Godfriaux, P. (2010), Gulf of Mexico gas hydrate joint industry project Leg II: Green canyon 955 site summary, http://www.netl.doe.gov/technologies/oil-gas/publications/Hydrates/2009Reports/WR313SiteSum.pdf.

McConnell, D., Boswell, R., Collett, T., Frye, M., Shedd, W., Guerin, G., Cook, A., Mrozewski, S., Dufrene, R., and Godfriaux, P. (2010), Gulf of Mexico gas hydrate joint industry project Leg II: Walker Ridge 313 Site summary, http://www.netl.doe.gov/technologies/oil-gas/publications/Hydrates/2009Reports/WR313SiteSum.pdf.

Hydrate Ridge

Shipboard Scientific Party, 1994. Site 892. *In* Westbrook, G.K., Carson, B., Musgrave, R.J., et al., *Proc. ODP, Init. Repts.,* 146 (Pt. 1): College Station, TX (Ocean Drilling Program), 301–378. doi:10.2973/odp.proc.ir.146-1.010.1994

Shipboard Scientific Party, 2003. Site 1244. *In* Tréhu, A.M, Bohrmann, G., Rack, F.R., Torres, M.E., et al., *Proc. ODP, Init. Repts.,* 204: College Station, TX (Ocean Drilling Program), 1–132. doi:10.2973/odp.proc.ir.204.103.2003

Shipboard Scientific Party, 2003. Site 1251. *In* Tréhu, A.M, Bohrmann, G., Rack, F.R., Torres, M.E., et al., *Proc. ODP, Init. Repts.,* 204: College Station, TX (Ocean Drilling Program), 1–119. doi:10.2973/odp.proc.ir.204.110.2003

Japan Sea

Shipboard Scientific Party, 1990. Site 796. *In* Tamaki, K., Pisciotto, K., Allan, J., et al., *Proc. ODP, Init. Repts.,* 127: College Station, TX (Ocean Drilling Program), 247–322. doi:10.2973/odp.proc.ir.127.106.1990

Shipboard Scientific Party, 1990. Background, objectives, and principal results, ODP Leg 127, Japan Sea. *In* Tamaki, K., Pisciotto, K., Allan, J., et al., *Proc. ODP, Init. Repts.,* 127: College Station, TX (Ocean Drilling Program), 5–33. doi:10.2973/odp.proc.ir.127.101.1990

Krishna-Godavari (India)

Collett, T., Riedel, M., Cochran, J., Boswell, R., Presley, J., Kumar, P., Sathe, A., Sethi, A., Lall, M., Sibal, V., and the NGHP Expedition 01 scientists (2007), National gas hydrate program expedition 01 Initial report.

Mallik

Wright, J.F., Dallimore, S.R., and Nixon, F.M. (1999), Influences of grain size and salinity on pressure-temperature thresholds for methane hydrate stability in JAPEX/JNOC/GSC Mallik 2L-38 gas hydrate research-well sediments, in Scientific results from JAPEX/JNOC/GSC Mallik 2L-38 gas hydrate research well, Mackenzie Delta, Northwest territories, Canada, *Geological survey of Canada*, 544, 229-240

Mt. Elbert

Dai, S., Lee, C., and Santamarina, J.C. (2010), Characteristics, mechanical properties and geophysical parameters of sediments from the Mount Elbert gas hydrate stratigraphic test well, Alaska North slope, *Marine and petroleum geology*, in print.

Nankai Trough

Expedition 314 Scientists, 2009. Expedition 314 Site C0002. *In* Kinoshita, M., Tobin, H., Ashi, J., Kimura, G., Lallemant, S., Screaton, E.J., Curewitz, D., Masago, H., Moe, K.T., and the Expedition 314/315/316 Scientists, *Proc. IODP,* 314/315/316: Washington, DC (Integrated Ocean Drilling Program Management International, Inc.). doi:10.2204/iodp.proc.314315316.114.2009

Expedition 316 Scientists, 2009. Expedition 316 Site C0006. *In* Kinoshita, M., Tobin, H., Ashi, J., Kimura, G., Lallemant, S., Screaton, E.J., Curewitz, D., Masago, H., Moe, K.T., and the Expedition 314/315/316 Scientists, *Proc. IODP,* 314/315/316: Washington, DC (Integrated Ocean Drilling Program Management International, Inc.). doi:10.2204/iodp.proc.314315316.134.2009

Shipboard Scientific Party, 1991. Site 808. *In* Taira, A., Hill, I., Firth, J.V., et al., *Proc. ODP, Init. Repts.,* 131: College Station, TX (Ocean Drilling Program), 71–269. doi:10.2973/odp.proc.ir.131.106.1991

Tobin, H., Kinoshita, M., Ashi, J., Lallemant, S., Kimura, G., Screaton, E.J., Moe, K.T., Masago, H., Curewitz, D., and the Expedition 314/315/316 Scientists 2009. NanTroSEIZE Stage 1 expeditions: introduction and synthesis of key results. *In* Kinoshita, M., Tobin, H., Ashi, J., Kimura, G., Lallemant, S., Screaton, E.J.,

Curewitz, D., Masago, H., Moe, K.T., and the Expedition 314/315/316 Scientists, *Proc. IODP,* 314/315/316: Washington, DC (Integrated Ocean Drilling Program Management International, Inc.). doi:10.2204/iodp.proc.314315316.101.2009

Tobin, H., Kinoshita, M., Moe, K.T., and the Expedition 314 Scientists, 2009. Expedition 314 summary. *In* Kinoshita, M., Tobin, H., Ashi, J., Kimura, G., Lallemant, S., Screaton, E.J., Curewitz, D., Masago, H., Moe, K.T., and the Expedition 314/315/316 Scientists, *Proc. IODP,* 314/315/316: Washington, DC (Integrated Ocean Drilling Program Management International, Inc.). doi:10.2204/iodp.proc.314315316.111.2009